UNIVERSITY OF CALIFORNIA,
IRVINE

Functionalizing C-MEMS: From Surface Modification to Structural Modification

DISSERTATION

submitted in partial satisfaction of the requirements for the degree of

DOCTOR OF PHILOSOPHY

in Engineering

by

Sunshine Holmberg

Dissertation Committee:
Professor Marc J. Madou, Chair
Professor Jack Brouwer
Associate Professor Yun Wang

2018

DEDICATION

To my parents and friends, for without whom this would not be possible

"You always try to think so far outside the box, that you never thought to put together the necessary tools into the box"

-From a Wise Man

"… Because you don't have a box"

-From a Wise Guy

TABLE OF CONTENTS

LIST OF FIGURES

LIST OF TABLES

ACKNOWLEDGMENTS

I would like to acknowledge the UCI's BioMEMS lab and thank Dr. Marc Madou for his guidance and wisdom over these many years. I would, also, like to acknowledge all the wonderful friends and researcher I have met and had the pleasure to work with during my tenure in this lab. In particular, I would like to thank Alexandra Perebikovsky, Lauren (EunByul) Cho, Brandon Pollack, Derosh George and Dr. Maziar Ghazinejad, who would there for me when things got tough. I would also like to thank all the visiting scholars and other scholars that I've had the pleasure to work and learn from including but not limited to Oscar Pilloni, Dr. Arnoldo Salazar, Deeno Carpendras, Mario Ramos, Rahul Kamath, Ross Milton, Maria Bauer, Ehsan Shamloo, Hamsa Gowda, Paola Ginestra, Melissa Rodriguez, Monze Cobak, Ka Lle, Mehdi, Giulia Canton and many others. Many parts of work were also made possible through collaboration with many of the aforementioned current, and past members of the BioMEMS family.

Support for many of the experiments came from various sources including National Science Foundation (NSF) grant #1449397. Specialized instruments necessary for a large degree of this work was generously provided access to by UCIs Chemistry Department Laser Spectroscopy, UCI integrated Nanosystems Research Facility (iNRF), UC Irvine Materials Research Institute (IMRI) and UCI National Fuel Cell Research Center (NFCRC).

For use of copyrighted images special thanks go to John Wiley and Sons, Nature Publishing Group, American Chemical Society, IOP Publishing, IEEE, Royal Society of Chemistry and Elsevier for permissions. Few of the figures are used under CC BY 3.0 and 4.0.

CURRICULUM VITAE

SUNSHINE HOLMBERG

EDUCATION

University of California, Irvine (UCI)
March 2018
Ph.D. in Engineering

University of California, Irvine (UCI) - 3.882 GPA
September 2012
M.S, Electrical Engineering and Computer Science

University of California, Los Angeles (UCLA)
June 2010
B.S., Electrical Engineering and Computer Science

RESEARCH EXPERIENCE

PhD Research - UCI BioMEMS Lab 9/12 - 4/18

Research and development of fabrication processes for carbon electrodes for energy harvesting and storing technologies:

- Carbon Material Synthesis
  - Developed a non-catalyst based route for graphitizing a "non-graphitizable" polymer
    - Resulting carbon exhibited a unique microstructure, which saw a profound enhancement in its electrochemical performance, including increased ability for:
      - Oxygen reduction
      - Hydrogen peroxide reduction
      - Selective simultaneous detection of dopamine, glucose, ascorbic acid, and uric acid
  - Developed method to synthesize carbon nanofibers infused with gold nanoparticles
    - Gold nanoparticles can act as catalysts for sensing or used as active sites to attach function groups
- Enzymatic Biofuel Cell
  - Adapted functionalization technique for carbon nanofibers made through electrospinning of polyacrylonitrile
    - Demonstrated superior performance due to larger surface area
  - Developing method
  - Developing an enzymatic fuel cell for wastewater remediation and energy regeneration
  - Developing C-MEMS process for creating porous flow-through fuel cell system
- Practical and Theoretical experience with multiple spectroscopy technique including
    - High Resolution Transmission Electron Microscopy (HRTEM)

        - Scanning Electron Microscopy (SEM)
        - Electron diffraction spectroscopy (EDS)
        - Raman Spectrpscopy
        - X-ray Photoelectron Spectroscopy (XPS)
        - Fourier Transform Infrared Spectroscopy (FTIR)
            - Attenuated Total Reflection spectroscopy (ATR)
        - IR absorption spectroscopy
        - X-ray Diffraction Spectroscopy (XRD)
- Electrospinning
    - Developed various electrospinning methods and setups
        - Rotating drum setup
            - Capable of aligning the deposited fibers along one orientation
            - Allow for uniform film deposition
        - Electric field guided setup
            - Capable of unique carbon film architectures with ranging degree of porosity
            - Controlled by shape of electric field
        - Developed method for electrospinning block co-polymers
            - Allows for fabrication of carbon fibers with gold nanoparticles
    - Developing process for controlling porosity of electrospun polymer mats
    - Developing process to automate and better control Electromechanical spinning process for nanowriting polymer patterns
        - Developed a controllable automated electrostatic initiation method
        - Supervised the development of near-field drum electrospinning capable of produce high precision nanopatterns with features size of ~3 µm and 1 µm spacing
- Dye-sensitized solar battery
    - developing a means of capturing and storing solar energy chemically
- Clean room training
    - spin coating, mask aligner, wet bench (i.e. etching)

Masters Research - UCI BioMEMS Lab
9/10 - 9/12

Research into implantable biofuel cell devices:

- Glucose Oxidase Biofuel Cell
    - Developed a novel immobilization technique for carbon electrodes for an enzymatic biofuel cell with a glucose oxidase anode and laccase cathode for implantable devices.

NATCAR Research member - UCLA, Los Angeles, CA 9/08 - 6/10

UCLA NATcar team member

- Researched, developed and simulated a non-linear control system for controlling the NATcar (an autonomous miniature vehicle that follows an electric wire, which radiates a signal at a certain frequency)

EMPLOYMENT

Broadcom intern - Irvine, CA 6/10 – 6/12

Test engineer for Broadcom Bluetooth devices:

- Developed software to test the robustness of bluetooth devices
- Developed software for reading bluetooth device information and diagnosing bluetooth device errors

Physical Optics Corporation (POC) intern - Torrance, CA 6/10 - 6/11

Prototype development for SBIR projects:

- Developed LabVIEW software to control galvanometer mirrors for multiple LIDAR systems
- Developed software with LabVIEW to control and characterize miniature piezo-electric motors
- Conducted, modified, and improved a process for making photovoltaic cells for electrolysis of water for hydrogen fuel generation.

PUBLICATIONS

- Bisht, Gobind S., et al. "Diffusion-free mediator based miniature biofuel cell anode fabricated on a carbon-MEMS electrode." *Langmuir* 28.39 (2012): 14055-14064.
- Holmberg, Sunshine, Alexandra Perebikovsky, Lawrence Kulinsky, and Marc Madou. "3-D micro and nano technologies for improvements in electrochemical power devices." *Micromachines* 5, no. 2 (2014): 171-203.
- Holmberg, Sunshine, Melissa Rodriguez-Delgado, Ross D. Milton, Nancy Ornelas-Soto, Shelley D. Minteer, Roberto Parra, and Marc J. Madou. "Bioelectrochemical study of thermostable Pycnoporus sanguineus CS43 laccase bioelectrodes based on pyrolytic carbon nanofibers for bioelectrocatalytic O2 reduction." *ACS Catalysis* 5, no. 12 (2015): 7507-7518.
- Pollack, Brandon, Sunshine Holmberg, Derosh George, Ich Tran, Marc Madou, and Maziar Ghazinejad. "Nitrogen-Rich Polyacrylonitrile-Based Graphitic Carbons for Hydrogen Peroxide Sensing." *Sensors* 17, no. 10 (2017): 2407.
- Ghazinejad, Maziar, Sunshine Holmberg, and Marc Madou. "Manufacturing carbon nanofiber electrodes with embedded metallic nanoparticles using block copolymers templates." In *Carbon Nanotubes, Graphene, and Emerging 2D Materials for Electronic and Photonic Devices IX*, vol. 9932, p. 99320G. International Society for Optics and Photonics, 2016.
- Salazar, Arnoldo, Maria Bauer, Sunshine Holmberg, and Marc J. Madou. "Study of Pulling Effect on the Electrical Conductivity of Suspended Carbon Microfibers Due to Electromechanical Spinning (EMS)." In *Meeting Abstracts*, no. 14, pp. 919-919. The Electrochemical Society, 2016.
- Holmberg, Sunshine. *Highly Electroactive Biofuel Cell developed using amine electro-oxidation technique for novel strategy of immobilization of Enzyme on fabricated Carbon MEMS Electrodes*. University of California, Irvine, 2012.
- Ghazinejad, Maziar, Sunshine Holmberg, Oscar Pilloni, Laura Oropeza-Ramos and Marc Madou. “Graphitizing non-graphitizable carbons by stress-induced routes.” *Sci. Rep.* Accepted.
- Holmberg, Sunshine, Maziar Ghazinejad, EunByul Cho, Derosh George, Alexandra Perebikovsky, Brandon Pollack, and Marc Madou,. “Electrocatalysis of Stress-Activated Pyrolytic Carbons” In preparation.

- Cho, EunByul, Sunshine Holmberg, Marc Madou, and Maziar Ghazinejad. “Enhanced Laccase Bioelectrocatalysis of Oxygen Reduction on Stress-Activated Pyrolytic Carbon Nanofibers” In preparation.

CONFERENCES

- ICOMM 2016 conference proceedings – submitted manuscript – publication pending
- SPIE 2016 Optics, Photonics and Nanoscience Engineering - Submitted 2 manuscripts
- ECS 2016 229th Meeting - attended

COMPUTER/TECHNICAL SKILLS

Software: COMSOL, SolidWorks, LabVIEW, MATLAB, PSPICE, Taurus Supreme, Orcad, Microsoft Word, Excel, PowerPoint, C++, Perl, Gamry Framework Scripts, Python, Raspberry Pi

ABSTRACT OF THE DISSERTATION

Functionalizing C-MEMS: From Surface Modification to Structural Modification

By

Sunshine Holmberg

Doctor of Philosophy in Engineering

University of California, Irvine, 2018

Professor Marc J. Madou, Chair

Carbon-MicroElectroMechanical systems (C-MEMS) use patterning and nanofabrication techniques developed for integrated circuits (ICs) in combination with traditional carbon pyrolysis to create intricate 3-D carbon materials and electrodes from organic precursors. The fabrication of specialized, pyrolytic carbon microfeatures and geometries, such as carbon micro-post arrays or interdigitated electrode arrays (IDEAs), significantly enhances carbon's electrical, chemical and mechanical properties to create high performance sensors and energy storage devices.

However, C-MEMS is generally limited to using amorphous or glassy carbons since most inexpensive carbon microfabrication processes require cross-linking a non-graphitizing polymer precursor. The inability to change the microstructure of a polymer precursor to a configuration that yields graphitic carbon inhibits the performance of the resulting material. Furthermore, traditional processes for functionalizing carbon using surface modifications are typically too harsh for its small microfeatures. The ideal solution is to develop a fabrication process that allows for the structural and surface modification of pyrolytic carbons without sacrificing cost or scalability. The results of this work present a novel method for electromechanically modifying the microstructure and surface properties

of carbon to significantly enhance its electrochemical activity. Specifically, the results of a comprehensive materials and electrochemical characterization of the structurally modified carbon reveals a new class of stress-activated pyrolytic carbon (SAPC). The SAPC showed a remarkable improvement in graphitization and demonstrated an inherently high and enduring electrocatalysis that has yet to be seen with any other pyrolytic carbon to date. Furthermore, the SAPCs simple and scalable synthesis process is compatible with common C-MEMS fabrication processes, creating a new tool for C-MEMS operators to tune the properties of their carbon electrodes.

1 – INTRODUCTION

1.1 Motivation and Overview of this Work

Within the last few decades, a rise in interest in carbon research grew from the development of nanocarbon synthesis processes. At the forefront of these research is the field of Carbon-Microelectromechanical systems (C-MEMS), which evolved from micro- and nanofabrication techniques developed for Integrated Circuits (IC) devices[1]. Integration of IC microfabrication with carbon pyrolysis allows for the synthesis of intricate 3-dimensional carbon microfeatures, which are capable of amplifying carbon's electrical and mechanical properties. For instance, the development of carbon micropost arrays and interdigitated electrode arrays (IDEAs) greatly enhanced the performance of electrode beyond the capability of the carbon alone[2]–[4]. These carbon microstructures amplified the current signals to achieve lower limits of detection for sensors and greater power density for energy storage devices. Similarly, Bauer demonstrated how carbon microlattices can greatly enhance the strength of carbon microstructures[5]. Despite tremendous progress being made by the field, C-MEMS still face huge hurdles stemming from the challenge in developing synthesis processes that can maximize the electrocatalytic capabilities of carbon.

A primary issue comes from an inadequate understanding of carbon synthesis processes such as pyrolysis[6]. This lack of understanding greatly limits researcher's ability to tune the structural properties of carbons. Particularly for C-MEMS, researchers are limited to non-graphitizing carbons as many of the microfabrication processes requires cross-linked

or rigid polymer precursors that can endure the temperatures of pyrolysis to maintain the morphology of the precursor[7], [8]. To further exacerbate this limitation, traditional processes for activating pyrolytic carbons are typically too harsh for the small microfeatures of C-MEMS devices[8], [9]. The main goal of this thesis is to develop strategies for enhancing the electrocatalysis of C-MEMS electrodes for electrochemical application. The results of this work demonstrated several surface modification techniques, which culminated in the development of a novel method stress-induced structural modification for enhancing C-MEMS electrochemical activity[10]. Specifically, the results of a comprehensive materials and electrochemical characterization of the structurally modified carbons reveals new class of stress-activated pyrolytic carbons (SAPC), with measured electrocatalytic activity comparable to graphene and carbon nanotube-based electrodes. These results indicate that this newly developed methodology could create a new pathway for enhancing future C-MEMS electrochemical device performance.

2 - BACKGROUND

2.1 Carbon

Carbon is a remarkably simple element with an incredibly rich chemistry. Its capacity for forming different chemical bonds, both with itself and other elements, has a profound impact on almost all fields of research. For example, the fundamental basis of organic chemistry is founded on the principle of understanding the nature of carbon and its innumerable different forms. Despite the vast amount of research devoted to the understanding of carbon, the extent of our knowledge on the nature of carbon is still largely inadequate. The discovery of bucky balls by Richard Smalley, Harry Kroto and Robert Curl in 1986[11], carbon nanotubes by Sumio Iijima in 1991[12], and graphene by Andre Geim and Konstantin Novoselov in 2004[13], served to not only corroborate the existence of some long-theorized carbon allotropes but challenged the conventional knowledge of the structure, properties, and applications of carbon. The unique properties exhibited by these new forms of carbon spurred the development of an entirely new field of research focused on the study, synthesis, and application of these materials.

Perhaps the most intriguing allotrope among the three discovered is graphene, which was synthesized in 2004 using mechanical exfoliation[13]. A poster child of the rather unique properties and structure of carbon, graphene's 2-D structure makes up all graphitic allotropes of carbon, including carbon nanotubes and bucky balls. Graphene is a 2-D, atomically thin layer of graphite, consisting of carbon atoms arranged in a hexagonal ring

and held together with strong sp^2-hybridziated bonds. Until its synthesis, it was believed that a single sheet of graphene was thermodynamically unstable and would quickly curl up or deform immediately upon isolation from bulk graphite. Its surprisingly stable nature is fortuitous for carbon researchers, allowing for a host of new empirical studies and practical applications that have greatly heightened our understanding of the fundamental properties of graphitic carbons.

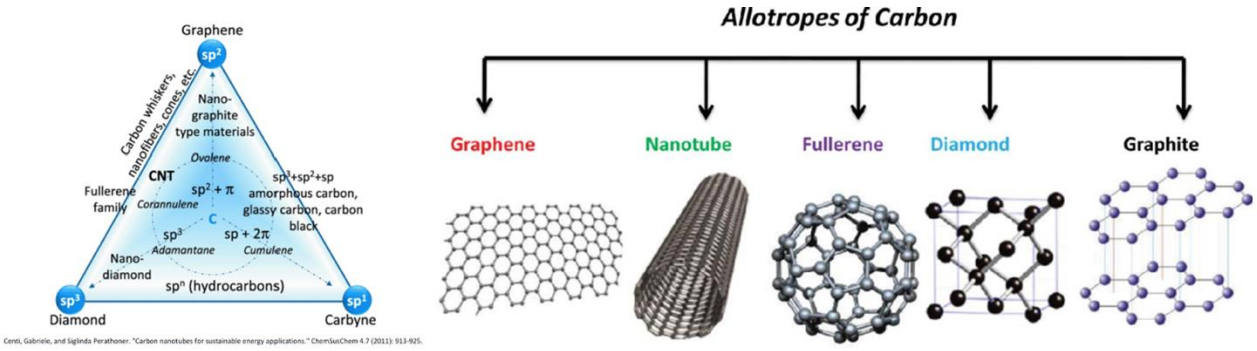

Figure 2.1. Various Carbon Allotropes. a) Triangle of various carbon allotropes with the vertices showing the pure crystalline carbon form of carbon's hybridization. b) Diagram of the various carbon crystalline allotropes. Adapted with permission from [14], [15].

The mechanical, thermal, and electrical properties of graphene, akin to its 2-D structure, is heterogenous in nature with respect to its crystal plane, which is particularly unique among nearly every other natural element. It is mechanically robust uniaxially and is also extremely pliable, as demonstrated by graphene-based electronics[16]–[18]. The Van der Waal forces holding together individual graphene sheets within graphite, however, are incredibly weak and can be easily broken, a principle seen every day by the amount of graphite pencils schoolchildren go through. This is also the governing principle of graphene synthesis via mechanical and chemical exfoliation[19]–[21]. When rolled into its carbon

nanotube tubular allotrope, it demonstrates a tremendously high young's modulus, making it ideal as a reinforcing material[22], [23].

Similarly, graphene's electrical properties are also defined by a large degree of heterogeneity. Conductivity measurements made perpendicular towards graphite basal planes can be 10^4 poor than that measured parallel along the graphite basal plane[24], [25]. Figure 2.2 shows graphene's electronic density energy band structure, further illuminating its unique electrical properties[26]. Here in Figure 2.2, it can be seen that its electron state density thins near its Fermi level, creating a conical electronic band structure. This unique energy band structure has been exploited through careful synthesis processes to produce semiconducting graphitic structures like semiconducting single-walled carbon nanotubes and graphene nanoribbons[27]–[30].

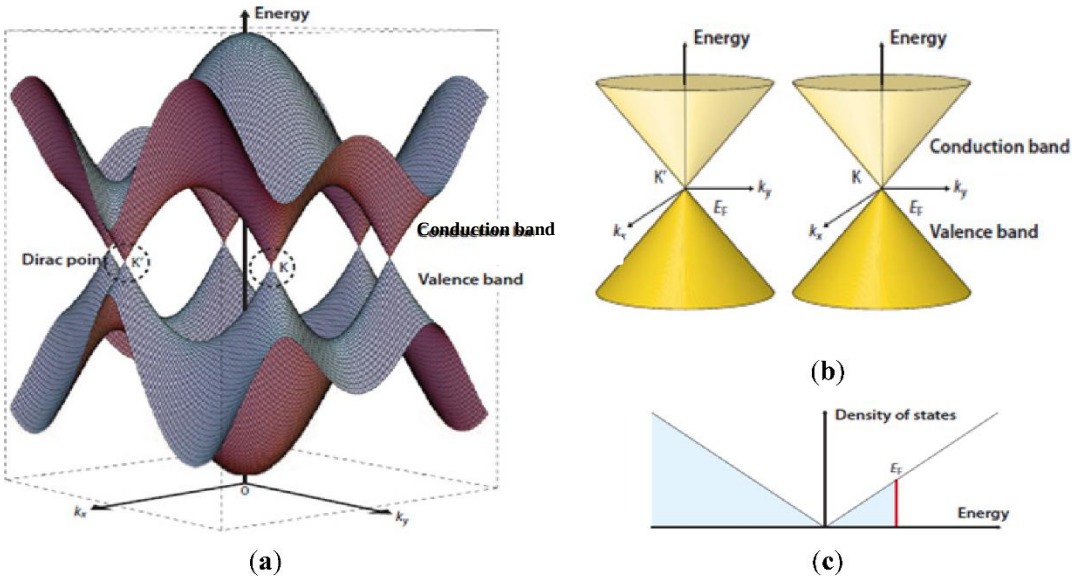

Figure 2.2. Carbon Electronic Energy Band Structure. a) Energy band structure near the Fermi Level, here the K and K' are Dirac points, where graphene conduction and valence bands intersect. b) Close-up of the Dirac points. c) Density of State near the Fermi energy level, E_F. Adapted with permission from [26].

Another fascinating implication of graphene's unique electron band structure is how it affects its chemical properties. Just like its electrical and mechanical properties, graphene chemistry also varies at different aspects of its crystal lattice. Graphene's basal planes are almost completely inert, while its edges are highly reactive and capable of forming different function groups[31], [32]. These edges are the primary sites responsible for electron transfer between graphitic materials and exogenous elements. A simplified understanding of this nature is that the sp^2-hybridized bonds, the backbone of the graphitic structure, largely satisfies carbon's 4 valence orbitals, leaving no empty electron states for the electron transfer process to be conducted. At graphitic edge planes, dangling bonds are present since there are no more adjacent carbon atoms to satisfy all 4 of carbon's valence orbitals. These dangling carbons are highly reactive, forming covalent bonds with various elements. The presence of heteroatoms at these edges provides graphitic carbons with other useful properties including absorptivity and hydrophilicity. The rich and heterogeneous chemistry of graphitic carbons holds great significance in the field of electrochemistry, where carbon is used as a premiere electrode material.

2.2 Carbon Electrochemistry

Carbon's large thermal, electrical, chemical, and electrochemical stability windows and good conductivity makes it particularly suitable as an electrode material for the highly corrosive environment in many electrochemical systems. As a result, carbon has found widespread use in many different electrochemical applications, ranging from energy storage applications, like proton-exchange membrane (PEM) fuel cells[33], [34], to biosensor applications, such as glucose and pH sensors[2], [35]–[37]. Despite experiencing

commercial success in electrochemical applications, carbon has been largely overshadowed by its metallic counterparts, gold and platinum, in terms of electrocatalytic performance. Furthermore, despite its rich chemistry, carbon often requires complex activation processes to gain the full value of its electrochemical performance[9], [38]. Even with recent advances in the development of carbon nanoallotropes like graphene, expensive multi-step processes are usually necessary to obtain a carbon electrode with sufficient electrocatalysis.

As previously discussed, the difficulty in synthesizing an "ideal" carbon electrode for electrochemical applications stems largely from its unique electronic energy band structure. Unlike the uniform density of states (DOS) of gold and platinum, carbon's energy band structure varies drastically based on its microstructure. For graphitic carbons like graphene and Highly Ordered Pyrolytic Graphite (HOPG), its valence and conduction bands only have small overlaps near the Fermi level, forming a rather unique energy band structure where the DOS near it's Fermi level is very low, as seen in Figure 2.2. For electrochemistry, the heterogenous electron transfer process is dependent on the availability of electronic states and therefore the greater the DOS, the faster the electron transfer process can proceed[9], [21]. As a result, the electron transfer rate of highly graphitic carbons is particularly sluggish. Interestingly, introducing "defects" into the graphene planes will increase the electron DOS and in turn greatly enhance the electron transfer rate. Indeed, studies from Compton *et al* have shown that the measured electrochemical kinetics of graphitic carbons is nearly completely dependent on the quantity of graphitic edges and "defects", concluding that the graphitic basal plane is almost entirely electrochemically inert[21], [39]. In this regard, one may hypothesize that highly

disordered carbon such as glassy carbon and amorphous carbon will exhibit much greater electrocatalysis. While this is largely true in comparison with basal plane graphite, these forms of carbon are largely inferior to the performance seen on graphitic edge planes. Furthermore, increased disorder generally reduces the electrical conductivity of carbon, which also has a significant effect on carbon's electrochemical performance. Thus, the answer to optimizing carbon electrochemical performance is not a trivial one and is one that many researchers have sought through the development of new post-carbon-synthesis activation processes.

The most widely used activation processes are based on carbon surface modification through covalent attachment of function groups or through adsorption or entrapment in a permeable matrix of various catalytic materials[9]. These methods often use carbon as purely a current collector and structural base for more electrocatalytically active elements such as metal nanoparticles, enzymes, and reactive functional groups and have been applied commercially in, for example, fuel cell systems. For hydrogen fuel cells, highly graphitic pyrolytic carbon nanofibers act as a conductive base to collect electrons from the more active catalyst layer[40]. In this case, the catalyst layer is usually a slurry consisting of a mixture of more active carbon particles such as activated carbon and platinum nanocatalysts. The main drawback of surface modification is that it doesn't directly address the sluggish electrochemical kinetics of most carbon electrodes, ultimately resulting in kinetic losses in the electron transfer process between the carbon and the catalyst layer. These losses can range from electrical contact resistance between the materials to sluggish electrochemical transfer rates with organic catalysts, which is why surface modifications are often done in conjunction with carbon structural modifications.

In contrast to surface modifications, carbon structural modification techniques are aimed at “activating” carbon electrodes to promote features that have greater electrocatalysis such as graphitic edges and defects. The simplest of these methods involves physically damaging the surface of highly graphitic materials through harsh treatment techniques such as mechanically breaking or fracturing the electrode, polishing the surface with an alumina slurry either by hand or via sonication, laser etching, or plasma bombardment[9]. Though commonly used in laboratory settings with bulky pyrolytic carbons, this process creates features that are transient in nature. The graphitic edges and defects created in these physical activation processes tend to lose electrocatalytic activity over time due to passivation of edges through spontaneous processes like chemisorption of oxygen. To address these stability issues, researchers have developed methods to simultaneously activate these features and functionalize them with various heteroatoms that enhance their electrochemical stability. These methods include acid treatments, electrochemical activation, reactive plasma treatments and various thermal treatments[9], [41]–[44].

Specifically, doping graphitic carbon structures using heteroatoms has gained growing recent interest due to the remarkable enhancement in electrocatalytic activity exhibited by these doped carbons[43], [45], [46]. The most common heteroatoms that have been used as dopants are nitrogen and phosphorus, which inject extra electron carriers into the graphene matrix, effectively making an “n-type” carbon that exhibits quasi-metallic behavior[47], [48]. Alternatively, boron has also been inserted into graphene lattices, adding hole carriers and making a “p-type” carbon material with a positively charged lattice[49], [50]. Currently, doping methods have been demonstrated mostly with graphitic nanoallotropes like graphene and carbon nanotubes and often requires expensive post-

carbon-synthesis processes. Alternative methods for synthesizing heteroatom rich carbons have also been demonstrated through use of traditional carbon thermal decomposition processes[51]–[53]. By choosing appropriate carbon precursors that are rich in the desired heteroatoms, such as melamine and polyacrylonitrile (PAN), these precursors can be carbonized at relatively low temperatures to preserve these heteroatoms within the final carbon structure. However, until very recently this method has been limited to carbons with non-graphitic structures, which exhibits less than stellar electrocatalysis, or graphitic nanoparticles. In fact, many of the outlined carbon modification strategies are not compatible with contemporary carbon micro- and nano-machining processes. Specifically, Carbon Micro-electromechanical systems (C-MEMS) technology, which aims to produce intricate 3-dimensional nanostructures, have difficulty applying many of the conventional carbon activation and modification process into its nanofabrication methodologies[3].

2.3 C-MEMS

Carbon Microelectromechanical systems (C-MEMS) were first developed at the end of the last century, when a series of papers by various groups of researchers demonstrated how traditional photolithography processes developed for integrated circuits (ICs) could be used to pattern carbon microfeatures[54]–[56]. This development was particularly significant as it helped address the long-standing challenge of carbon micromachining, which was previously unfeasible due to the brittle nature of pyrolytic carbon materials. Even with more modern synthesis process developed for carbon nanotubes and graphene, it is still challenging to fabricate the 3-dimensional nano- and micro-structure made possible by C-MEMS technology. Research conducted by Madou *et al* demonstrated the

remarkable potential this new technique had for various electrochemical applications[3], [4], [55], [56].

In 1998, Kim *et al* demonstrated that simple carbon electrodes made through pyrolyzing positive and negative photoresist microstructures exhibited adequate quasi-reversible electrochemical kinetics that are comparable to glassy carbons pyrolyzed at much greater temperatures, without the need for subsequent activation steps[56]. C-MEMS proved to be a powerful tool to overcome the carbon's relatively lackluster electrochemical kinetics, as was demonstrated by the development of high surface area carbon micropost arrays and interdigitated electrode arrays (IDEAs) [3], [3], [4], [57]. Wang *et al* utilized a two-step fabrication process to produce high-aspect ratio carbon micropost arrays[3]. Playing with UV exposure rates, they discovered clever ways to utilize the unwanted diffraction effect of the UV light to create suspended bridge structures between the carbon posts, as seen in Figure 2.3. Electrochemical characterization of these structures demonstrated a particularly high lithium ion charge/discharge capacity due to the high surface area produced by their unique geometry [57].

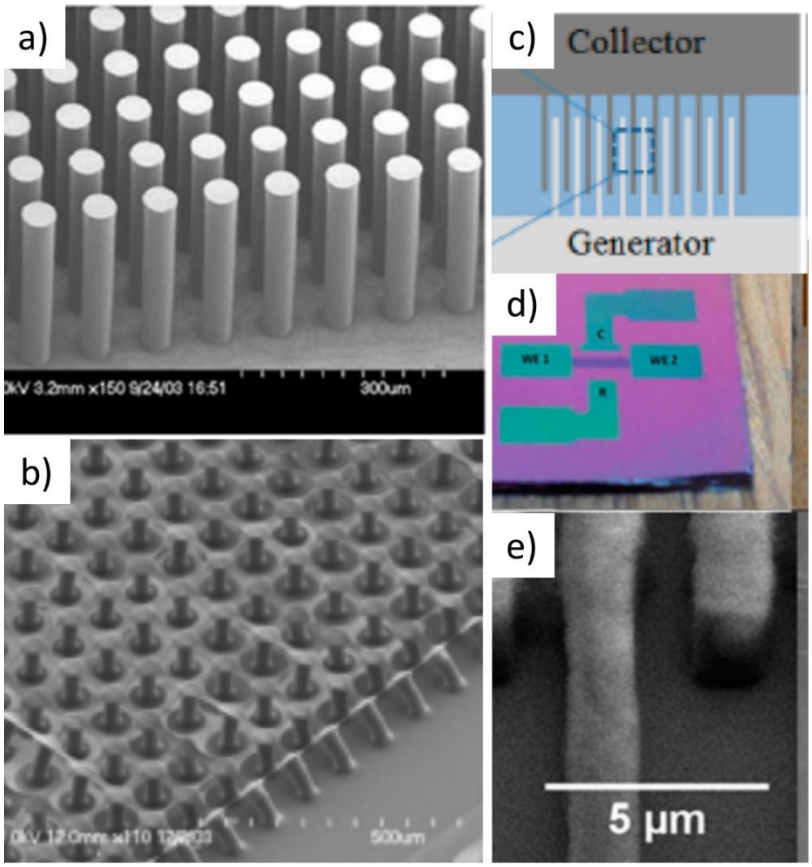

Figure 2.3. Photolithography-based C-MEMS Structures. SEM and optical images of a) carbon micropost array electrodes and b) carbon micropost with interconnected bridges made through photolithography-based C-MEMS techniques. c) Conceptual schematic of Interdigitated Electrode arrays (IDEAs). d) Optical image and e) SEM images of fabricated C-MEMS IDEAs interdigitated electrode arrays Adapted with permission from [3], [4].

More recently, Kamath *et al* optimized the photolithography process for fabrication of IDEAs with micron-size features, approaching feature sizes for gold and platinum IDEAs that utilize substantially more expensive and cumbersome processes[4]. The unique architecture of the carbon IDEAs can amplify the current response to an electroactive species by more than 40 times, greatly reducing the lower limit of detection for electrochemical sensors. This is accomplished by holding two closely spaced interdigitated

working electrode fingers at opposing potentials to promote the oxidation or reduction of a redox active species (Figure 2.4). Due to the close spacing of the fingers (~1 um) and the 3D nature of the electrodes, each redox species experience multiple redox reactions before it diffuses into the bulk and leaves the system. Each redox cycle increases the current, enhancing its overall electrochemical response. To accomplish such a feat requires the two working electrodes' fingers to be placed within a few microns of each other without physical contact to avoid shorting the two working electrodes together. In this way, this work showed the remarkable potential of C-MEMS technology.

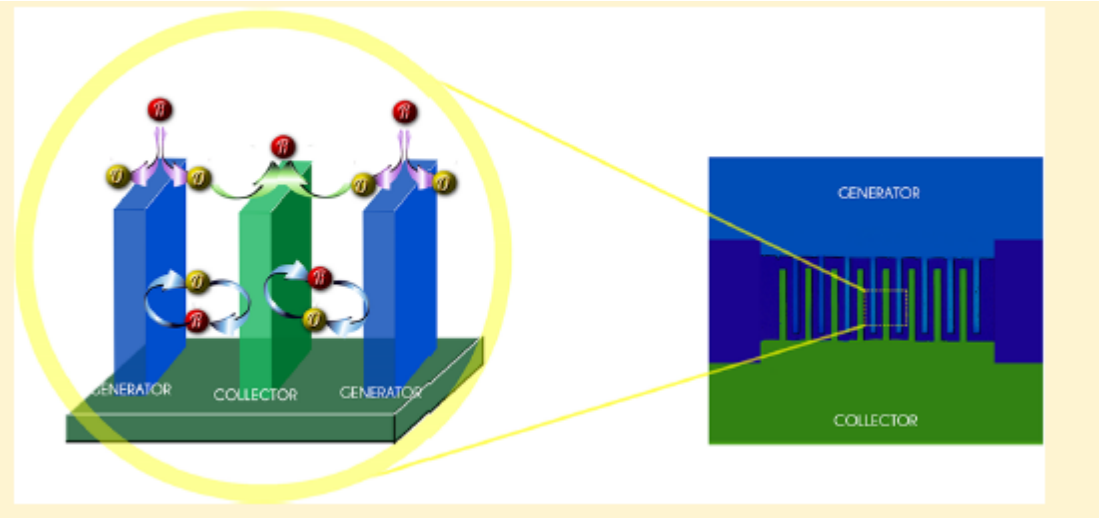

Figure 2.4. IDEA's Electrochemical Response Amplification Process. Each redox analyte cycles between the generator, where its oxidized, and collector electrodes, where its reduced, thus amplifying the electrochemical response of the redox analyte. Reproduced with permission from [4].

2.4 Photolithography Techniques

The most prolific C-MEMS fabrication technique is based on the UV photolithography developed by the IC industry. As illustrated in Figure 2.5, the process can be broken down

into 4 major steps: 1) application of photoresist onto the desired substrate, 2) patterning of the photoresist, 3) development of the photoresists and 4) pyrolysis[3], [56], [58]. In the first step, convention method of application of photoresists involves the spin coating of the photoactive resin on to a substrate, typically silicon wafer. The substrate is then spun at high RPMs, utilizing centrifugal forces to stretch the resin evenly across the substrate. Here, it has long been experimentally determined that the thickness of the resin can be directly tuned by adjusting the RPM. Alternative ways to apply photoresist electrospinning nanofibers polymers unto a substrate and heat-pressing dry-photoresist, which are thin films of photoactive polymers. After the photoresist is applied, a mask of the desired pattern is placed over the film and the polymer is exposed to the appropriate wavelength of light, most commonly in the UV spectrum. Depending on the type of the polymer, the UV will either crosslink the polymer, in the case of negative photoresists, or cause scissions within the polymer, as in the case of positive photoresist, thus creating difference in resistance of the exposed and unexposed polymer to its developer. The polymer structure is then created by developing away less developer resistant areas of the polymer and finally carbonized through thermal decomposition in an inert environment, a process called pyrolysis.

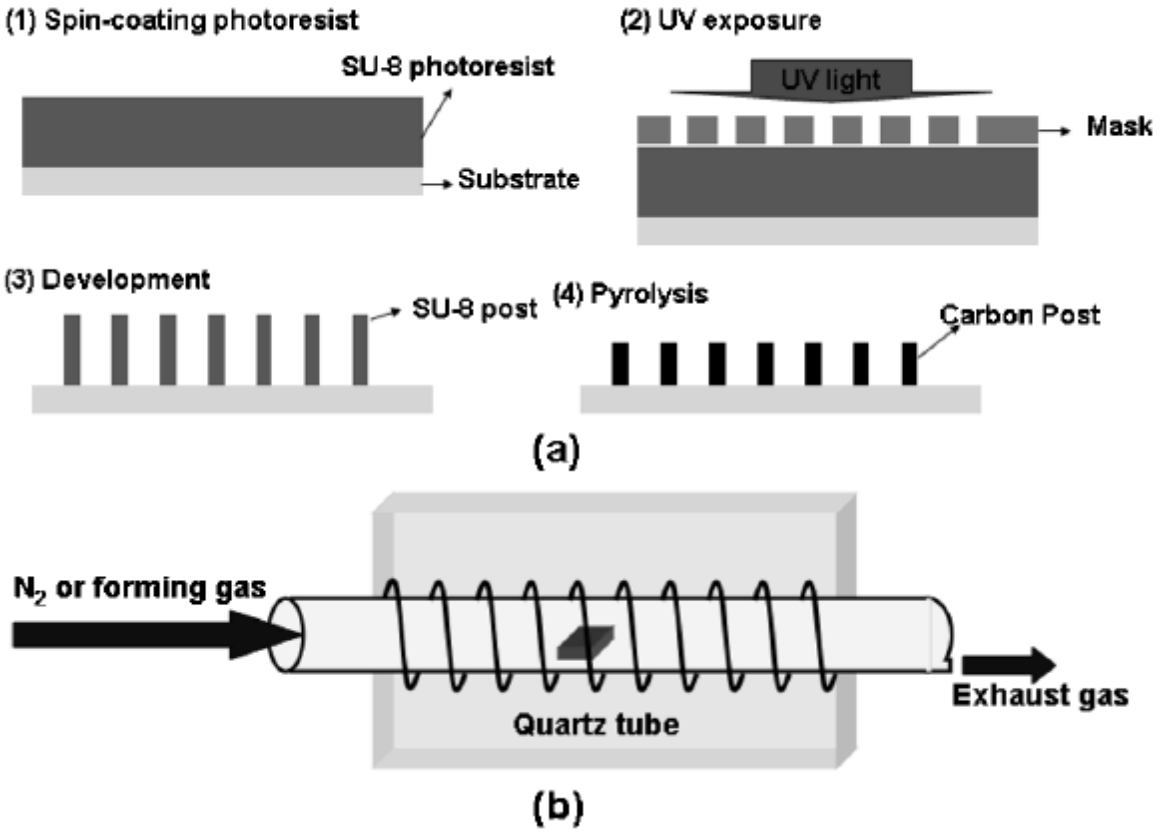

Figure 2.5. C-MEMS Photolithography Process. a) Diagram of standard SU-8Photolithography process and b) Pyrolysis process. Reproduced with permission from [3].

For C-MEMS, there are subtle differences between the photolithography processes optimized for ICs and that for making carbon microfeatures. First, not all photoresist is "pyrolyzable", which means they do not retain their polymer microstructure after pyrolysis. Second, extra care and step are necessary in the photolithography process for C-MEM to promote the adhesion of the photoresist layer to the substrate[58]. This is particularly important since photoresist were designed for ICs system where they are almost entirely designed to be impermanent, sacrificial layers. While there are some other general considerations of what constitute good C-MEMS fabrication protocols, the field and

techniques developed are largely base based on experimental results and not particularly well-defined. Similarly, what polymers are considered “pyrolyzable” is largely based on experimental results, with only loose rules like avoiding polymers with oxygen groups that can cause the polymer to burn during pyrolysis.

2.5 Advanced Lithography Techniques

As technology advanced within the last two decades, more advanced lithography processes were applied to C-MEMS technology. LIGA and Electron-beam and X-ray lithography were the logical extension to traditional photolithography process, allowing for researchers to push the feature size of carbon electrodes into the nano-domain and further increasing aspect ratios of their microstructures[58], [58]–[61]. However, these technologies had major drawbacks and challenges when applied towards mass-manufacturing due to their extreme cost and lack of scalability. As a response to these challenges, other polymer fabrication processes were developed. One of such technology is nanoimprinting lithography, which based on soft lithography techniques[58], [62], [63]. Unlike traditional photolithography, nanoimprint lithography is entirely a mechanical fabrication process. As shown in Figure 2.6, the process utilizes a stamp consisting of the inverted nanofeatures, which is mechanically pressed into the polymer film to transfer the pattern into the polymer. The polymer is then cured via heat or UV treatment to solidify its structure. Sometimes subsequent ion bombardment or further development and etching process are applied to further remove unwanted features or polymer residues.

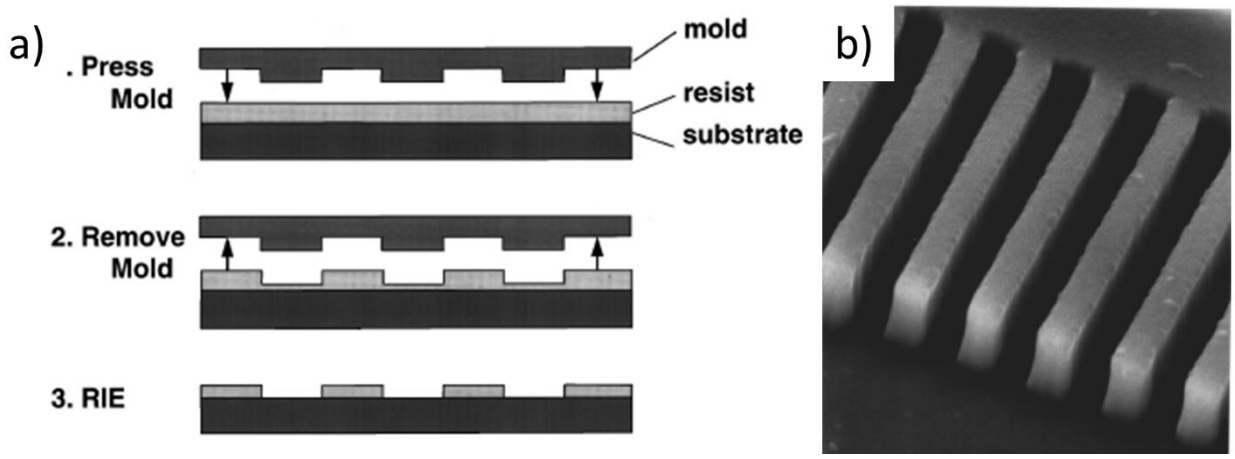

Figure 2.6. Nanoimprint Lithography. a) Schematic of nanoimprinting process. b) SEM image of C-MEMS electrodes fabricated using nanoimprinting lithography. Adapted with permission from [62].

Perhaps the most flexible techniques developed to date is two-photon lithography[64]. The basic concept of this technique, as outlined in Figure 2.7, involved the focusing the beam a laser to "nanowrite" a 3D dimensional structure. At the focal point of the interference of different photons generates enough intensity to crosslink a polymer. This allows for serially crosslink precise areas within a bath of the photoresist to construct intricate 3-D polymer structures. The promise of this technique was demonstrated by Kraft *et al*, who utilized the technology develop an intricate carbon nanolattice which displayed incredible mechanical strength due to its unique architecture (Figure 2.7)[5]. The main drawback for this technology is that it's a serial writing technology and, like the other serial writing technology described earlier, is not particularly easy to scale into mass-manufacturing processes. However, 3-D printing and nanowriting technologies have been growing rapidly in popularity and sophistication within the past few years, foreshadowing the necessity for scalability may no longer be a limiting factor.

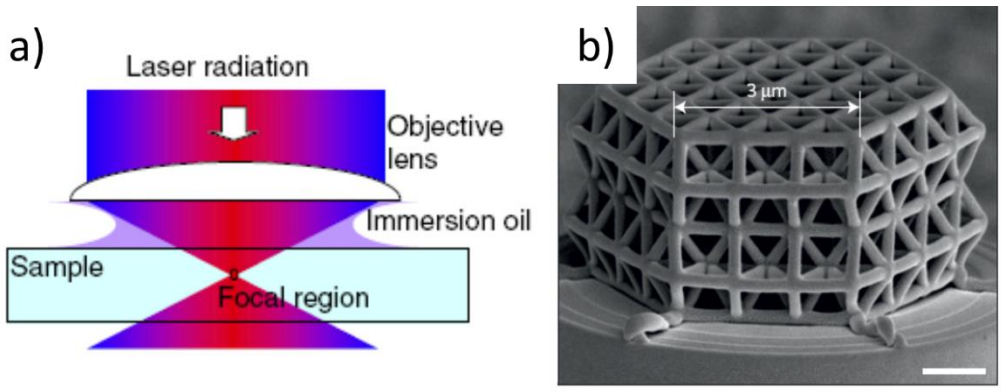

Figure 2.7. Two-photon Lithography. A) Schematic of the Two-photolithography process and B) SEM image of carbon microlattice fabricated with two-photon lithography. Adapted with permission from [5], [64].

2.6 Electrospinning

Possibly the most unique C-MEMS fabrication developed to date is electrospinning. Electrospinning is nanofabrication technique for synthesizing nanofibrous patterns and textiles[65]. The process utilizes a large electrical field to stretch a polymer solution into nanofibers and is widely used for its ability to readily synthesis sub-micron polymeric fibers in a scalable fabrication process. This phenomenon was first demonstrated nearly a century ago and has been studied extensively by numerous researchers. Among these was the seminal work from Geoffrey Taylor, who developed the mathematical model to describe electrospinning's initiation process, which would become to be known as the Taylor cone[66]. The phenomenon would continue to be explored with Darell Reneker and Alexander Yarin, who would model other aspects of the process as it would pertain to polymeric solutions such as the bending instability[65], [67], [68].

Fundamentally, electrospinning is the interplay between external electrostatic forces and internal viscous forces of the polymer solution. Starting at it initiation process, the applied

external electric field will distort the polymer droplet, seen in Figure 8, into a conical shape until it reaches a critical limit where the electrostatic force overcomes the surface tension of the polymer droplet. As described by Taylor, this limit is characterized by angle of the cone, which becomes instable after reaching <49.3^{o} called the Taylor cone[66]. Another aspect of the interplay of forces plays out in the electrospinning jet just after the Taylor, Figure 2.8. Here if the viscous forces are too weak in comparison to the electrostatic forces, the polymer jet is ripped apart into droplets, becoming a process called electrospraying. As the electrostatic forces decreases, the polymer jet transitions from droplets to beady fibers and finally to fibers of various diameters.

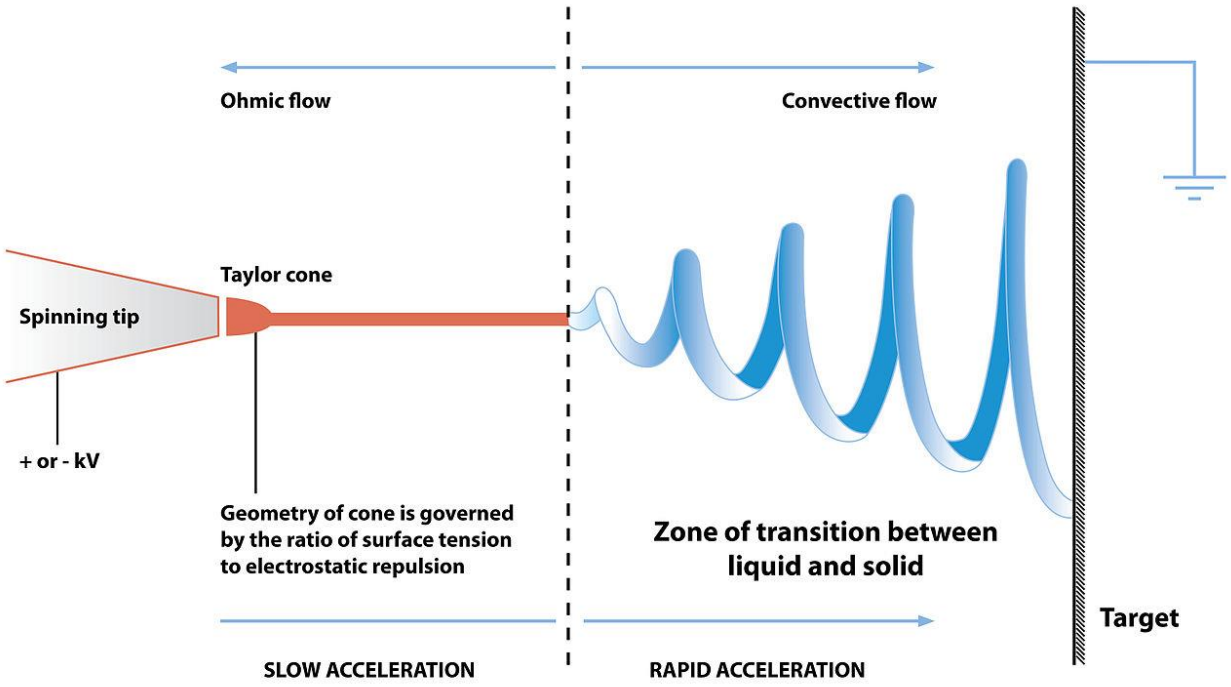

Figure 2.8. Electrospinning Process. Permission obtained from Wikipedia under CC BY 3.0.

Finally, as the fibers travel, rapid evaporation of the fibers occurs, rapidly shrinking and freezing the polymer structure and trapping the charges built up by the electric field into a

nanofibrous form. The entrapped charges cause repulsion between the fibrous jet and creates a whipping effect as the fibrous jet extends beyond the Taylor cone[65], [68]. This whipping effect is known as the bending instability and is responsible for the randomly oriented nanofibrous matrix making up many of the electrospun textiles. Understanding of the interplay between these forces allows researchers to tune the synthesized fibers morphology and fully exploit the various forces at play. For example, it will be demonstrated later in this thesis how these forces are an integral part of the synthesis of Stress-Activated Pyrolytic Carbons (SAPC)[10].

2.6.1 Far-Field Electrospinning

The traditional electrospinning process as described in the previous section has become rebranded to Far-Field Electrospinning due to the development of a new nanowriting process derived from the same concept, which will be described later[69]. Though Far Field Electrospinning has been extensively studied, there are still a slew of nuanced facets of the process that is not fully understood. A popular field of current research, is the development of patterning techniques to control patterns and microfeatures of the electrospun fibers. One aspect of this research involves the electrospinning of photoresists, which can then be patterned using photolithography techniques, allowing for the ability to create carbon microelectrodes with large surface area[70]. Similarly, electrospinning has also been combined with nanoimprinting technology and 3-D printing technology to create 3-dimensional micro and macro features to supplement the nanofeatures for various applications ranging from biosensors to stem cells growth platforms[71]–[75]. Another alternative method to forming 3-dimensional structures can be achieved by using a

patterned collecting substrate, as the electron spun fibers will conform to the surface of the collecting substrate and retain the structure after it is removed from the collector[76].

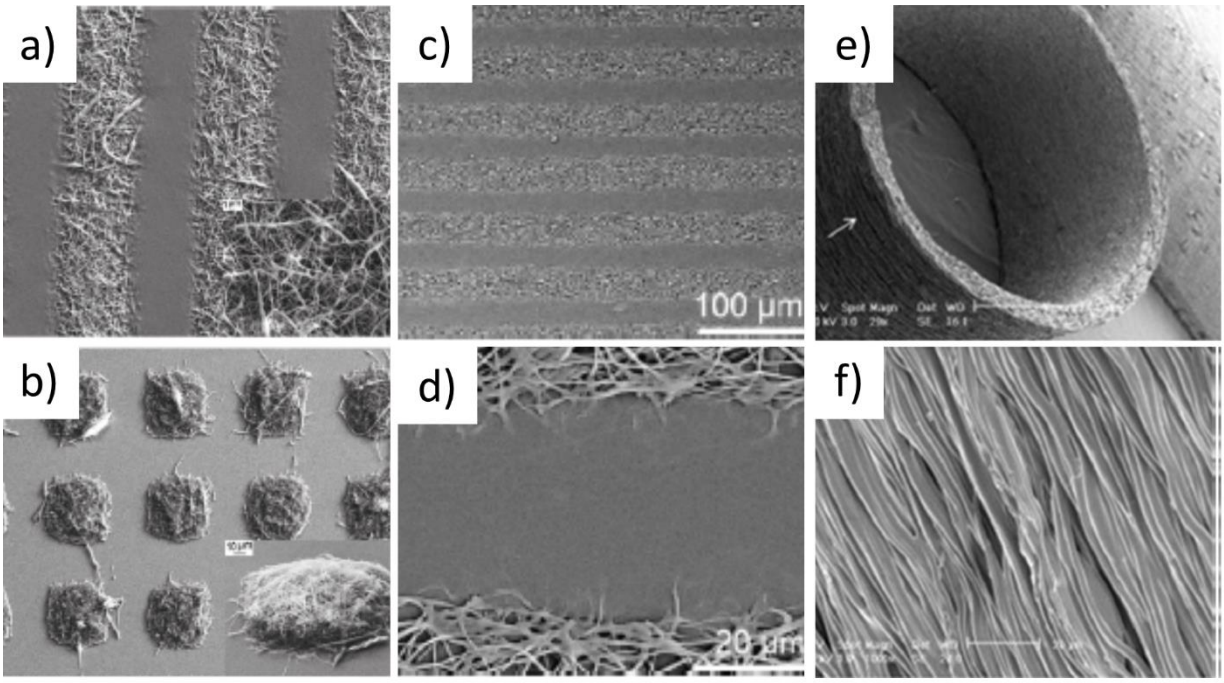

Figure 2.9. Patterned Electrospinning Structures. SEM images of electrospun nanofibers patterned with a-b) photolithography[70], (c-d) nanoimprinting lithography [71] and (e-f) conformation to collector shape. [76]. Adapted with permission from [70], [71], [76].

Beyond patterning, studies have been conducted to control the orientation, alignment and the density of the deposited fibers through clever manipulation of the collecting stage. These techniques can be categorized into either mechanical manipulation or electrical manipulation. Mechanical manipulation is typified by a rotating drum setup, which is usually operated at greater than 1000 RPM. At these high RPM's, the rate of rotation of the stage begins to match with the rate at which the fibers are being drawn from the Taylor cone, causing the fibers to become oriented along the tangential direction of rotation[77]–[79]. Variations of this technique have been developed, which includes additional x-y axis

motion to allow for more intricate patterns to be produced (Figure 2.10). An example of this process can be used to create crisscross patterns by alternating the direction of the linear actuation[80], [81]. By tuning the linear actuators speed and the rotational speed, both the spacing and the angle between the intersection of the fibers could be controlled. The spacing between the fibers was shown to enhance the supercapacitance of the fabricated carbon electrodes, by enhancing the transport of the ions to the surface of the electrodes.

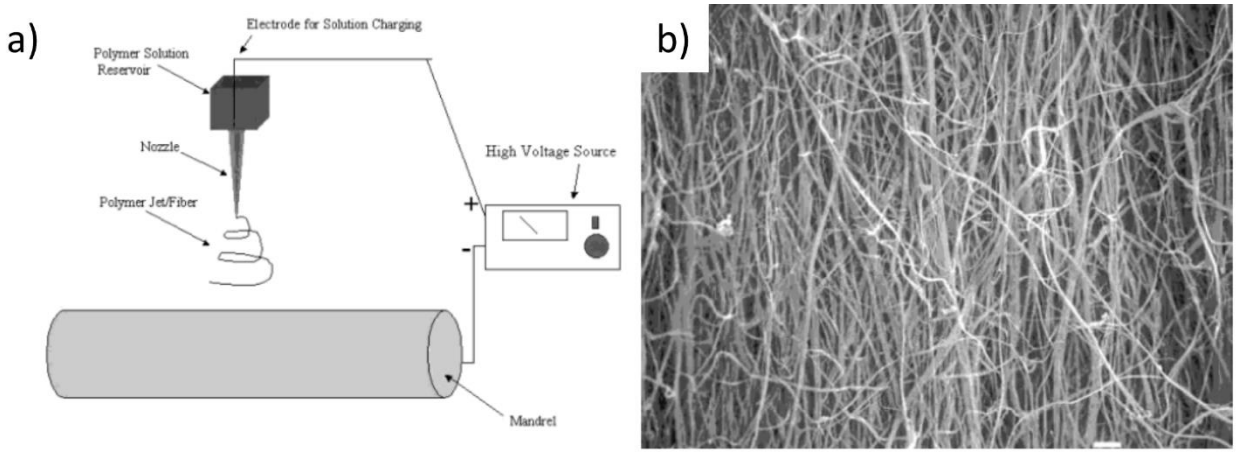

Figure 2.10. Electrospinning with rotating drum. A) Diagram of electrospinning with rotating drum setup and b) SEM image of the Aligned electrospun fibers synthesized with this method. Adapted with permission from [77].

An alternative strategy to mechanical alignment can be achieved by manipulating the electrospinning's electric field. The most common of these methods alter the shape of the collecting substrate as shown in Figure 2.11. Studies from numerous research have shown that the nanofiber are attracted towards conducting substrates. By having two parallel conducting pieces, the depositing fibers would deposit on both plates and cause the fibers between the metallic pieces to be aligned between the parallel plates. This phenomenon

was later explained by Zhao *et al* to be a result of distorting of the electric field and the bend instability of electrospinning[82]. The electric field converges only at conductive collectors, therefore pulling the polymer jet towards them. The bending instability, caused by charge repulsion within the polymer jet, causes the jet to whip violently between the collecting substrate. The combination of these two phenomenon causes the alignment of the polymer fibers across non-conducting areas of the collector. Zhao *et al* demonstrated this phenomenon occurs for even more intricately-designed collector such as tightly spaced checkered patterns in Figure 2.11[82]. In addition, the lower electric field strength in the insulated areas also creates a lower density of deposited fibers, thus creating varying thickness and pore density throughout the electrospun fabric. These unique 3-dimensional structures could have potential application I future of membrane technologies.

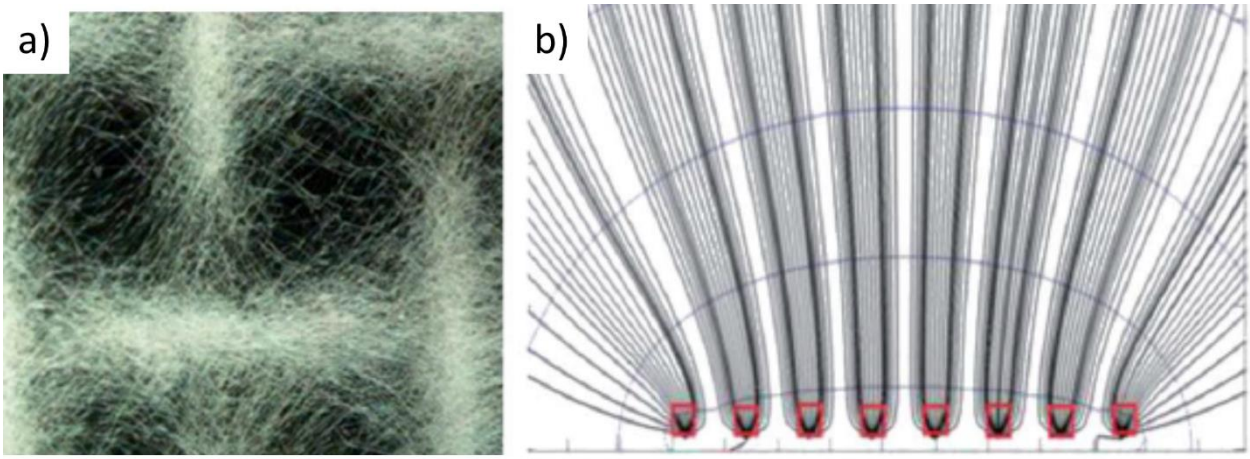

Figure 2.11. Electrostatic templating of electrospinning process. a) SEM image of the aligned fiber made with a metallic wire mesh template and b) The electric field of created by the metallic wire mesh. Adapted with permission from [82].

Alternatively, the electric field can be manipulated by altering the electrospinning setup rather than the collector. A common method is to install concentric metallic rings between

the dispensing needle and the collector[83]. By applying voltages to these rings, the electric field can be altered to expand or contract the area of deposition. The rings can be replaced with split ring to allow for further control of the direction of the polymer jet. This technique was further adapted by fixing the electrospinning setup to a x-y linear stage platform, allowing for the system to "write" the nanofiber matrix[84].

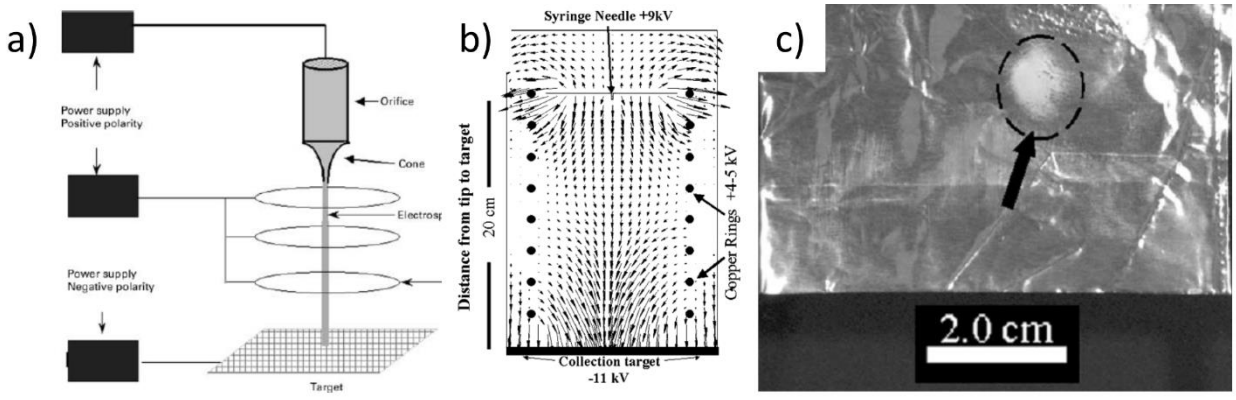

Figure 2.12. Electric field manipulation in electrospinning. a) conceptual diagram of concentric ring electrospinning setup, b) diagram of the altered electric field by the rings and c) optical image of the smaller deposition area caused by the rings. Adapted with permission from [83].

2.6.2 Near-Field Electrospinning

Unlike the Far-Field Electrospinning (FFES), Near-Field electrospinning (NFES) is novel technology developed within the last 2 decades. It was first demonstrated in 2006 by research group in Berkeley that adapted to the principles of traditional electrospinning to create a nanowriting system[69]. To accomplish this, the team scaled the electrospinning process to its "near-field" by reducing the applied voltage from 10-30 kV to >1kV and the working distance from 10-30 cm to >1 mm as seen in Figure 2.13. The group found that operating within this range prevents the polymer jet from entering the bending instability

regime, allowing he operator to control the position of the deposited fiber with the help of an x-y stage. Despite being a nascent technology, NFES has shown tremendous potential as one of the fastest nanowriting process for producing sub-micron nanofibers of polymers, carbon, and ceramic[85]–[88].

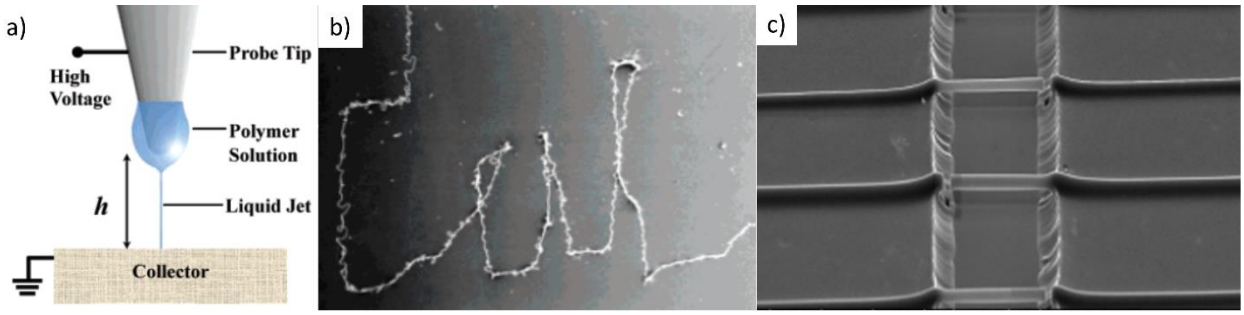

Figure 2.13. Near Field Electrospinning. a) Conceptual diagram of near-field electrospinning setup. b) Optical image of a pattern written using Near-field electrospinning and c) SEM image of suspended carbon nanofibers fabricated using near-field electrospinning. Adapted with permission from [69], [86]

However, being relatively new technology, NFES still faces many hurdles towards its automation and commercial viability, a large portion of which stems from a lack of understanding of the process. For example, Ehmann *et al* demonstrated that the trapped charges within the fibers can cause the fibers to repel each by greater than 100 microns and therefore difficult to reduce the spacing between the deposited fibers[89]. In addition, the smaller electric field used in NFES cannot provide adequate force to cause the Taylor Cone instability seen in FFES and requires an alternative method to initiate the process the process. These, along with other challenges, are all unique problems not seen in other 3-D printing and nanowriting process, which are mostly limited to optical limitations or mechanical limitation of stage and thus require their own clever and specialized solutions. For example, in my work in the BioMEMS Lab, we managed to address the former challenge

with using a conducting substrate to discharge the fibers and a latter with an electrostatic initiation process using a dielectric tip. However, these will not be addressed here as they are not the focus of this thesis.

2.7 Challenges for C-MEMS electrochemistry

Despite the significant strides made within the last few decades in the field of C-MEMS technology, it still faces numerous challenges. In this section, we will focus on the challenges for, specifically, C-MEMS electrochemistry and present the challenges facing their activation and functionalization and give an overview of the primary motivation for this work.

2.7.1 Limitation of C-MEMS pyrolysis

Fundamentally, C-MEMS is an extension of traditional carbon synthesis methodology based on the thermal decomposition of organic materials in an inert environment; A process known as pyrolysis. Despite widespread use for centuries, the pyrolysis process has only been scientifically studied within the last century. The first of these in-depth studies was conducted by Rosalind Franklin in early 1950's, when she tried to gain insight into the difference between Graphitizing and non-graphitizing carbons, carbons that do not convert into graphite even at extremely high temperatures (>3000 ^{o}C)[90]. Using X-ray Diffraction methodologies to gain insight into various pyrolytic carbon microstructure, Franklin described non-graphitizing carbons as highly porous structures, consisting of small graphene planes held apart by sp^3 hybridized covalent bonds. This concept would be revisiting much later by Peter Harris, who conductive extensive studies on carbon

microstructures using High Resolution Electron Microscopy[6], [91], [92]. Harris expanded upon Franklin's initial work and explained that the nanoporosity of non-graphitizing carbons is a result of cage-like microstructures, which resemble fullerenes. In addition, Harris contested that sp^3 hybridized covalent bonds are not thermodynamically stable enough to withstand the high temperatures of pyrolysis. This is evident from studies that have shown diamonds decompose into graphite at temperatures above 1700 ^oC. Instead, Harris attributes the non-graphitizability of the carbons to the propensity to form fullerenic structures, which are thermodynamically more stable than graphite. The concept of graphitizing vs. non-graphitizing would be further expanded upon by Kipling *et al*, who correlate the capacity to undergo a liquid-crystal fusion phase during pyrolysis with graphitizing carbons[93]. This phase is believed to be crucial to carbon's graphitizability as it allows for the carbon crystallites to rearrange themselves to form the graphene planes. Non-graphitizing carbons, on the other hand, do not undergo this fusion phase. Instead they, typically, undergo a cross-linking phase, which causes the carbon's structure to be become rigid and incapable of realigning to form the graphene planes. Despite the major contribution made by these researcher, our understanding of carbon pyrolysis is largely inadequate and limited to an inconclusive list of known graphitizing and non-graphitizing precursors.

In this context, C-MEMS technology have traditionally been limited to non-graphitizing carbons due, in large part, to the necessity for patternability. Most precursors that are suitable for MEMS fabrication technologies like photolithography and nanoimprint lithography utilizes UV or thermal crosslinking processes to define the polymer microstructures. However, this limitation remains true in precursors that do not require

crosslinking such as in the case of electrospun polystyrene fibers, which require UV crosslinking prior to pyrolysis to retain its morphology[94]. Another interesting example of this is the commercial fabrication process for carbon fibers made from pitch, a graphitizing carbon precursor[95]. To retain its graphitizing nature, pitch is melted at 300 ^{o}C to allow the carbon crystalline planes to align and then mechanically extruded out into fibrous form. The melt is then immediately cool-down to freeze its microstructure and subsequently crosslinked to retain its fibrous morphology during the pyrolysis process before it is finally carbonized via pyrolysis. Thusly, these studies suggest that the rigid non-graphitizing nature of C-MEMS polymers is a necessary property, whether its achieved through cross-linking or is inherent to the polymer. As previously discussed, this limitation in C-MEMS' atomic microstructure greatly inhibits the electrochemical performance of the CMEMS electrodes. Although fabrication processes like the one described for pitch have been developed for synthesis of graphitic, pyrolytic carbons, these strategies have yet been incorporated into C-MEMS technology or are largely incompatible with C-MEMS technology. Thus, this limitation leaves C-MEMS researchers to develop alternative pathways to enhance the electrocatalysis of C-MEMS electrodes indirectly through Functionalization methods.

2.7.2 Challenges in C-MEMS Functionalization

C-MEMS's inherently low electrocatalysis due to the limitation to tune its atomic microstructure is further exacerbated by the difficulties in functionalizing C-MEMS electrodes. As previously discussed, researchers have developed multiple methods to activate and functionalize pyrolytic carbons. Even non-graphitizing carbons'

electrochemical performance can be enhanced with these methods. For example, commercial glassy carbon with various activation processes have demonstrated electron transfer rates as high as activated, pyrolytic graphite[9]. However, many of the techniques developed for macro carbon electrodes are two harsh for the microfeatures of C-MEMS electrodes. Mechanical activation process like polishing, laser-activation and fracturing are entirely infeasible for C-MEMS electrodes as they will damage the microfeatures and morphology of the electrodes, completely negating the purpose of C-MEMS synthesis process. Similarly, chemical activation like nitric acid oxidation, plasma treatment and electrochemical activation will often severely damage the structure, creating pores within the structure or outright fracturing certain microfeatures. Therefore, functionalizing C-MEMS is typically limited to surface modification such a covalent attachment of function groups, linkers and catalysts or through painting more catalytic layers on top of the carbon structure. In the next chapter, I will describe several methods with which I've used to develop C-MEMS sensors and energy storage.

3 – SURFACE MODIFICATION

3.1 Enzymatic Catalyst Layer

3.1.1 Introduction

Among the various surface modification, the two simplest and most commonly used is perhaps the covalent attachment of function groups and adsorption of a catalysts. Both methods were explored in my prior work with Dr. Gobind Bisht, where it was demonstrated how glucose biofuel cell anodes can be functionalized by both covalent bonding and adsorption of glucose oxidase[8]. Though successful, the current density output was not particularly high compared to that reported by other studies. The low electrochemical response is common problem with these forms of modification of C-MEMS electrodes, which can largely be attributed to the poor electrocatalysis of C-MEMS electrodes as previously discussed. For bulk pyrolytic carbon electrodes, these functionalizing methods are often coupled with mechanical activation process like polishing, plasma treatment or electrochemical activation. These activation processes help open the graphitic edge planes to allow for more active sites for functionalization. In addition, this manner of functionalization has also been demonstrated to prevent these edges from passivation effects[41]. However, due to the difficulty in activating C-MEMS

electrodes without severely damaging their microfeatures this pathway is usually not available to C-MEMS researchers. To address this, C-MEMS researcher have instead functionalized more active substrates like carbon nanotubes, which are then subsequently "painted" on to C-MEMS electrodes as a paste. This technique is commonly implemented in fuel cell applications. Thus, in the next generation of C-MEMS biofuel cell electrodes, the enzymes were attached to carbon nanotubes and painted onto carbon nanofiber electrodes. In this configuration, the C-MEMS electrodes functions purely as a current collector with the carbon nanotubes acting as the conduit for electron exchange process with the enzyme. In this regard, Laccase was chosen as the catalysts of choice to produce biofuel cell cathodes for oxygen reduction.

Laccases (polyphenoloxidase; EC 1.10.3.2) are a group of multi-copper oxidases (MCOs) that couple the oxidation of a broad range of (poly)phenols and aromatic substrates to the reduction of molecular oxygen to water.[96]–[98] Many different isoforms of laccases have been discovered in a variety of organisms including lacquer trees, planktonic microorganisms, and insects, although they are most commonly found in fungi.[97]–[99] These different isoforms of laccase typically share similarities in their catalytic sites, which consist of two copper-based redox active centers. The copper atoms constituting the redox centers are classified into three categories depending on their characteristics obtained from UV/visible and electron paramagnetic resonance (EPR) spectroscopy: a type 1 (T1), a type 2 (T2) and a type 3 (T3).[96]–[99] The redox center responsible for the oxidation of phenolic substrates consists of a single T1 copper atom while the second redox center contains both T2 and T3 copper atoms that form a trinuclear cluster, where the reduction of molecular oxygen takes place.[96]–[99] Compared to other widely used oxidases such as

tyrosinase and peroxidases, laccases are more stable, versatile and only require protons for reducing oxygen to water.[98], [99] Although the different isoforms of laccase share similarities in their catalytic sites, their overall structure can often vary drastically and have significant impact on their behavior.[98], [99] For example, the commercially available laccase from *Trametes versicolor* has a redox potential of +800 mV *vs.* standard hydrogen electrodes (SHE) and exhibits its highest activity between pH 4 and 5, while laccase from *Rhus vernicifera* has a redox potential of +410 mV *vs.* SHE and maintains its highest activity in the pH range from 5.5 to 8.5.[100], [101]

Recent studies in laccase bioelectrocatalysis have led to the development of highly reproducible oxygen reducing cathodes for biofuel cell applications.[102]–[104] One of the main inspirations for these developments was a study by Blanford *et al.*[105] in 2007, in which laccase was immobilized onto a carbon electrode by orientating the T1 Cu site towards anthracene molecules that had been covalently attached to the surface of a carbon electrode. This anthracene immobilization method reliably oriented the T1 redox center close enough to the electrode to allow for direct electron transfer (DET) to occur between the T1 redox center and the electrode. The electron transfer is coupled intramolecularly from the T1 site to the T2/T3 oxygen reduction redox center, creating an efficient pathway to transfer electrons from the electrode to the reduction site for the oxygen reduction reaction.[10] Since this initial discovery many other research groups have adapted this immobilization method to various types of electrode materials and morphologies.[11–16] One example is the anthracene-modified multi-walled carbon nanotubes (AC-MWCNT) electrode designed by Meredith *et al.*[109] who immobilized laccases onto AC-MWCNT by mixing laccase and AC-MWCNT into a buffer solution to create a slurry that was applied to

a Toray carbon paper electrode.[13–16] The AC-MWCNT immobilization method was demonstrated to be very reproducible and versatile, capable of being applied to any number of different electrode support systems.

Despite the tremendous progress made in the field of enzymatic fuel cells (EFCs), the stability of enzymes is still a major issue that must be addressed if long-term EFCs are to be created.[7,22] For laccase, in particular, inhibitors such as hydrogen peroxide, chlorides and fluorides are also a major concern as they are present in many natural mediums and their presence will limit the applicability of laccase bioelectrodes to these environments.[15,23,24] While incorporating supporting enzyme such as catalase into the electrode system have proven effective for improving laccase stability and efficiency issues, many of these supporting biomolecules also have limited lifetimes.[25] Thus researchers have begun searching for new isoforms of laccases with higher lifetimes and increased resistance to inhibitors to help alleviate stability and efficiency issues associated with laccase bioelectrodes.[26–28]

In this context, Ramirez *et al*.[29,30], reported the production and characterization of two laccase isoforms from a native strain of the white-rot fungus known as *Pycnoporus sanguineus CS43.* Both isoforms displayed very high thermostability, in particular LAC1 exhibited a specific activity of 277 U/mg at 60 °C with a half-life of 18 hours.[30] Furthermore, these isoforms showed improved resistance to common laccase inhibitors such as chloride, methanol, and acetonitrile. These characteristics make these two isoforms of laccase particularly attractive for biofuel cell applications, especially for membrane-less

EFCs operating on methanol (as the fuel) or operating within a physiological setting (human serum containing 150 mM Cl^-).[31–36]

In this study, the first demonstration of bioelectrocatalytic oxygen reduction by two laccase isoforms isolated from the fungus *Pycnoporus sanguineus CS43* is reported. Their electrochemical performances were evaluated and compared to that of commercially available laccase from *Trametes versicolor* (TvL). LACI, LAC2 and TvL were immobilized onto multi-walled carbon nanotubes modified with anthracene moieties (AC-MWCNT) in the process developed by Meredith *et al.*[14] The laccase-anthracene-modified MWCNT (LAC-AC-MWCNT) mixture is then applied to a carbon nanofiber electrode (CNF) made from carbonizing electrospun polyacrylonitrile (PAN) mats using a C-MEMS fabrication process. Electrochemical characterization of the bioelectrodes was performed to determine their performances at different pH, temperature and with different inhibitors under hydrodynamic and hydrostatic conditions.

3.1.2 Materials and Methods

3.1.2.1 Chemicals

Polyacrylonitrile (PAN), 2,2'-azino-bis(3-ethylbenzothiazoline-6-sulphonic acid) (ABTS), laccase from (benzenediol:oxygen oxidoreductases; EC 1.10.3.2) *Trametes versicolor (TvL)*, and catalase (H_2O_2:H_2O_2 oxidoreductase; EC 1.11.1.6) from bovine liver were purchased from *Sigma Aldrich Co. LLC*. Ultra-Pure Argon and Ultra-Pure Oxygen were purchased from *Air Gas, Inc*. Dimethylformamide (DMF), citric acid monohydrate, sodium phosphate dibasic heptahydrate, sodium chloride, sodium fluoride and hydrogen peroxide were purchased

from *Thermo-Fisher-Scientific, Inc.* Loctite Hysol 9462 epoxy was purchased from *Ellsworth Adhesives.* Conductive carbon paint was purchased from *Structure Probe, Inc.* Citrate-phosphate buffers were prepared by mixing 0.1 M of citric acid and 0.2 M Na_2HPO_4 solutions until the desired pH is reached. Phosphate buffered saline (PBS) of pH 7.4 was made using by mixing 8 g of NaCl, 0.2 g of KCl, 1.44 g of Na_2HPO_4, and 0.24 g of KH_2PO_4 into 1 L of deionized water.

3.1.2.2 Enzyme Source and culture conditions

The white-rot fungus *P. sanguineus* CS43 was obtained from the culture collection of the Universidad Autónoma de Nuevo León, Mexico, kindly provided by Prof. Carlos Hernández. The enzyme production and purification of laccase isoforms were obtained using published procedures.[29,30] Laccase activity was determined using ABTS as substrate. The reaction mixture contained 0.5 mM ABTS in 0.1 M citrate/0.2 M phosphate buffer (pH 4) at 25°C with 20 µL aliquots of appropriately diluted culture purified enzyme. Spectrophotometric measurements of ABTS oxidation were monitored by following the increase in absorbance at 420 nm ($\varepsilon = 3.6 \times 10^4\ M^{-1}\ cm^{-1}$)[37], using a micro-plate reader (Omega FLUOstar, BMG LABTECH's, Germany). Enzyme activity was expressed as international units (U), where one unit corresponds to 1 µmol of product formed per minute. The laccase isoforms activities were 822 ± 6.32 KU L^{-1} and 2,890 ± 4.73 KU L^{-1}, for LAC1 and LAC 2, respectively.

3.1.2.3 Laccase inhibition – Spectroscopic assays

The purified isoforms were tested in the presence of common inhibitors at 25°C: H_2O_2, NaF and KCl. Inhibitions assays were carried out in a mixture of citrate/phosphate buffer (pH 4,

0.1 M) adding 20 µL of a laccase solution (30 and 60 U L^{-1} for LAC1 and LAC2, respectively) and the corresponding aliquot of ABTS (5mM, prepared in water), to obtain final ABTS concentrations of 0.03, 0.13, 0.33, 0.67, 0.83, 1.0 and 1.33 mM. Each inhibitor was tested at different concentrations depending on its effects on the enzyme. Stock solutions of inhibitors were prepared in citrate/phosphate buffer and substituted within the citrate/phosphate buffer aliquot, giving final concentrations in the range of 1 to 20 mM for H_2O_2; 0.01 to 1.5 mM for NaF and 3 to 600 mM for KCl . The mixture of laccase and inhibitor was incubated for 5 min at room temperature, before the activity was measured. Michaelis-Menten non-linear regression and Lineweaver-Burk double-reciprocal linearization analyses were performed with GraphPad Prism.

3.1.2.4 Carbon Nanofiber Electrode Fabrication

The carbon nanofiber electrodes were prepared by first spin-coating an 18% PAN in DMF solution at 300 rpm upon an aluminum foil substrate to form a thin PAN layer. The PAN nanofibers were electrospun at 1 kV/cm onto the thin PAN layer with an 8% PAN in DMF solution. The PAN nanofibers mats were then peeled of the aluminum foil and thermally annealed at 300 ^oC for 3 hours in air and then placed in a tubular high-temperature furnace for pyrolysis. The furnace was ramped to 900 ^oC at 5 ^oC/min in an inert (N_2) environment to carbonize the PAN nanofibers mats into carbon nanofibers mats. A copper wire was attached to the thin carbon layer using conductive carbon paint to allow for an electrical contact between the CNF electrodes and potentiostat. The thin carbon layer not only acts as a support for carbon nanofibers, but also provides a non-porous conductive membrane that prevents the buffer solution from interacting with the attached copper wire, which is

sandwiched between carbon layer and the Loctite 9462 epoxy (Figure 3.1a). The PAN nanofibers mats were cut to 1 cm^2 before pyrolysis, but the average geometric area of the CNF electrodes ranged from 0.2 cm^2 to 0.25 cm^2 due to shrinkage as a result of the pyrolysis.

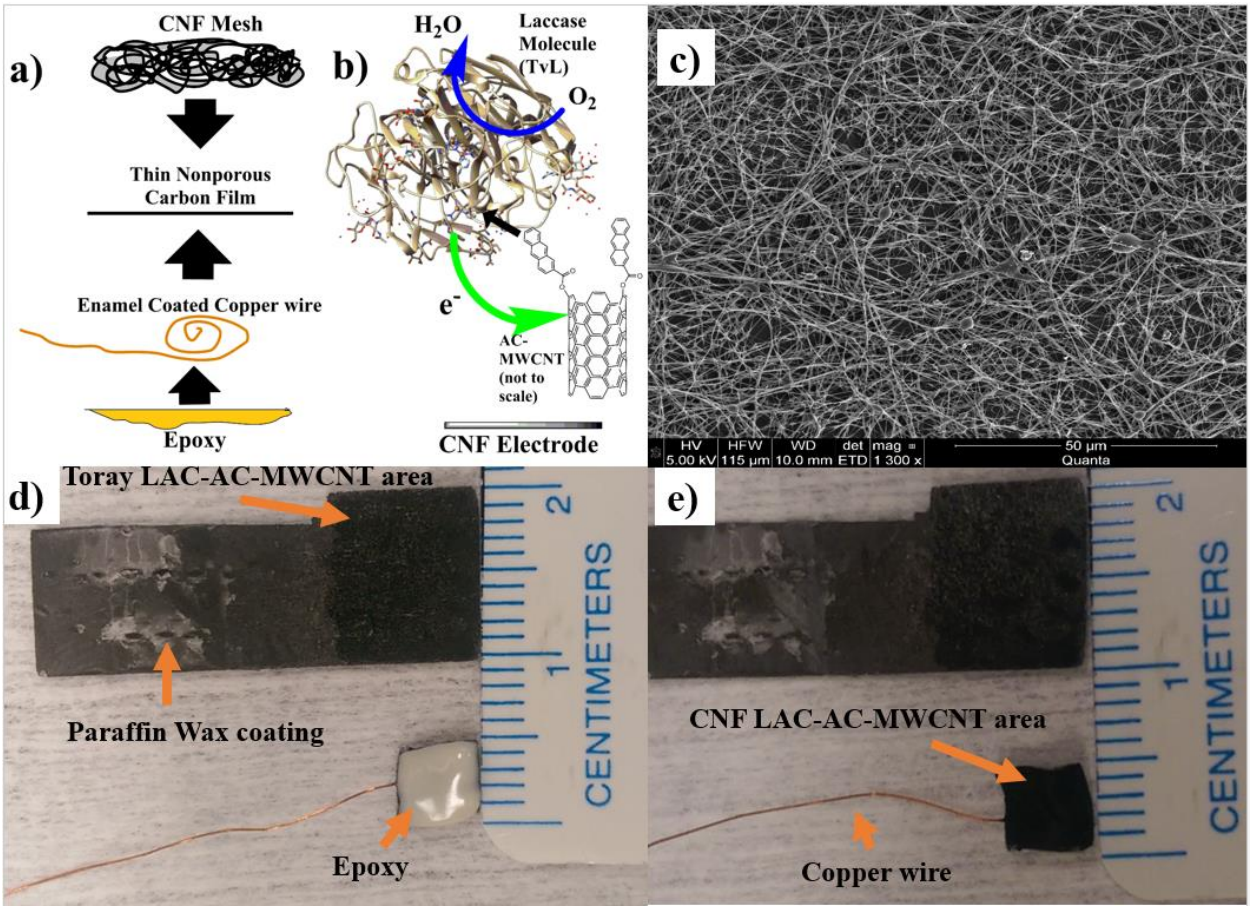

Figure 3.1. Laccase-CNT immobilization process a) Schematic view of the multiple layers of the CNF electrodes. b) Schematic of Laccase immobilization process. c) SEM image of the CNF electrodes. Images of the Toray and CNF electrodes (d) Paraffin wax was used to coat the strips of Toray to isolate the 1 cm^2 area for LAC-AC-MWCNT application and testing. Back side of the CNF electrode was covered with epoxy, which sandwiched the copper wire with the thin carbon layer. (e) Front side of CNF electrodes where the LAC-AC-MWCNT is applied. Reproduced with permission from *[128]*.

3.1.2.5 Laccase immobilization

AC-MWCNTs were prepared as previously reported.[14] For LAC1 and LAC2, the purified laccase solution was mixed 1:1 with citrate/phosphate buffer pH 5.0 then 25 µL of the diluted LAC1/LAC2 solution was mixed with 1.25 mg of the AC-MWCNT. The LAC-AC-MWCNT solution was vortexed at 2250 rpm for one minute then sonicated for 15 sec. This mixing process was repeated 3 more times before 6.25 µL of the LAC-AC-MWCNT mixture was applied to the CNF electrodes. A second coating (6.25 µL of the same solution) is applied after 15 minutes of the first coat in order to maximize enzyme loading. Then the LAC-AC-MWCNT electrode was left to dry for 30 minutes before testing. For the TvL laccase (1 mg) was mixed with 50 µL of the citrate/phosphate buffer pH 5.0 and 25 µL of the TvL solution was mixed with 1.25 mg of AC-MWCNT. The LAC-AC-MWCNT solution was then vortexed and applied to the CNF electrodes in the same double application process described for the preparation of the LAC1 and LAC2 electrodes. The CNF electrodes were soaked in citrate/phosphate buffer pH 4.0 for an hour before testing to increase the wettability of the CNF surface in order to improve contact between the AC-MWCNT and the CNF. All laccase solutions were normalized to 2.5 mg/mL after mixing with citrate/phosphate buffer.

Direct electron transfer (DET) between laccase T1 redox center and a conductive support by anthracene molecules occurs whereby anthracene mimics the hydrophobic properties of the natural substrates of laccase (*i.e.* phenols and polycyclic aromatic hydrocarbons). The presence of anthracene moieties on MWCNTs results in the favorable orientation of the T1 Cu site of laccase towards the electrode architecture, resulting in the ability of laccase to

undergo DET with the electrode. The LAC-AC-MWCNT immobilization process outlined above was first developed by Meredith *et al* [109]. and binds laccase to anthracene modified MWCNT by combining AC-MWCNT and a laccase solution to create a slurry (Figure 3.1b), which is then painted onto the CNF or Toray electrodes. The LAC-AC-MWCNT slurry is then left to dry and adsorb onto the CNF or Toray electrodes.

3.1.2.6 Electrochemical measurements

All electrochemical measurements were performed using a Princeton Applied Research Versastat 4 potentiostat, and conducted using a 3-electrode setup with a Ag/AgCl reference electrode (3M KCl) and a platinum wire as a counter electrode. The experiments were conducted in a small Pyrex beaker containing 10 mL of citrate/phosphate buffer, exposed to air. All electrochemical tests were run in triplicate.

3.1.2.7 LAC-AC-MWCNT Leaching study

The amount of enzyme leaching from LAC-AC-MWCNT electrodes was estimated using UV/Visible spectrophotometric absorbance measurements at 280 nm. Quantification of the amount of protein in a solution is possible by the absorption of aromatic amino acids at 280 nm with respect to a known standard solution. Typical UV-Visible spectra of laccase show two maxima around 280 and 600 nm. [96] Absorbance measurements were recorded using a Cary 50 spectrophotometer.

To simulate the hydrodynamic conditions, the LAC1 and LAC2 electrodes were prepared as previously described and immersed into a quartz cuvette containing 4 mL of deionized water. The UV-Vis absorbance spectrum (350 nm to 200 nm) of the leachate was measured

every 5 min at room temperature. The solution was mixed after each scan *via* pipette siphoning. To simulate the effect of temperature on the leaching of laccase into the solution, LAC1 and LAC2 electrodes were immersed into 10 mL DI raised to 45^{o}C. Aliquots of 1 mL of the solution were taken at 5 min, 10 min, 15 min, 30 min, 1 hr, 2 hr, and 4 hr and replaced with fresh DI to maintain the 10 mL volume. A volume of 1 mL of deionized water was also added every 1 hr to compensate for evaporation and maintain a consistent volume. The aliquots were then diluted to a 4 mL solution before UV absorbance measurement. A control solution was made by diluting 25 µL of the LAC1 or LAC2 solution in 4 mL deionized water. The leaching effect was estimated with relation to the maximum absorption peak obtained from the control solution (which is the maximum concentration of laccase that could be immobilized on each electrode) and the aliquot taken during the stability test.

3.1.3 Results and Discussion

3.1.3.1 Cyclic Voltammetry of the bioelectrodes

Cyclic voltammetry was used to evaluate the performances of the 3 different bioelectrodes under hydrostatic and hydrodynamic conditions. Citrate/phosphate buffer (pH 4.0) was chosen as the medium for comparison between the TvL and LAC1/LAC2 because of overlap in their optimal pH ranges (*i.e*. the optimal pH range of TvL is between 4 and 5 and optimal pH range of LAC1 and LAC2 is between 2 and 4).[30,38,39] The citrate/phosphate buffer was purged with oxygen or argon for 10 minutes before the O_2 and Ar saturation tests, respectively. The performance of the 3 laccases was evaluated on both Toray electrodes (Figure 2) and CNF electrodes (Figure 3.3).

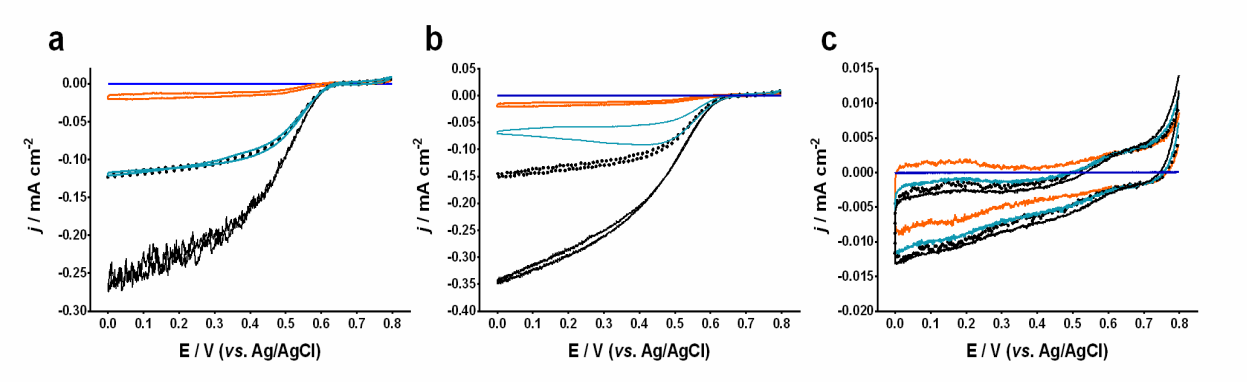

Figure 3.2. Representative cyclic voltammograms of (a) LAC1, (b) LAC2, and (c) TvL on Toray bioelectrodes at 1 mV/s in citrate/phosphate buffer pH 4.0 under (orange) continuous argon bubbling, (sky blue) under hydrostatic conditions exposed to air, (dotted black) under hydrodynamic conditions exposed to air, (solid black) under continuous oxygen bubbling and (blue) an unmodified Toray electrode under hydrostatic conditions exposed to air. Reproduced with permission from *[128]*.

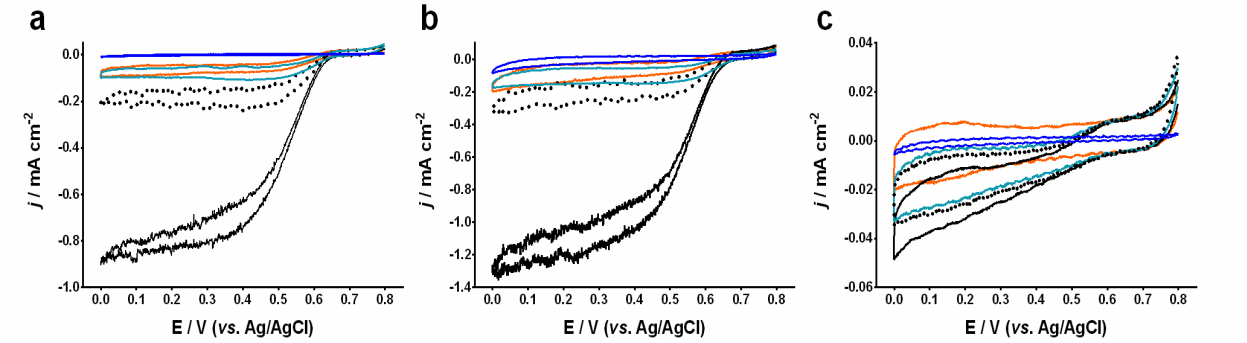

Figure 3.3. Representative cyclic voltammograms of (a) LAC1, (b) LAC2, and (c) TvL on CNF bioelectrodes at 1 mV/s in citrate-phosphate buffer pH 4.0 under (orange) continuous argon bubbling, (sky blue) under hydrostatic conditions exposed to air, (dotted black) under hydrodynamic conditions exposed to air, (solid black) under continuous oxygen bubbling and (blue) an unmodified CNF electrode under hydrostatic conditions exposed to air . Reproduced with permission from *[128]*.

The results of the cyclic voltammetry show that CNF electrodes consistently produced 4 to 5 times more current density than the Toray bioelectrodes for each isoform of laccase. A large part of this discrepancy in current density can be attributed to the electrochemical active surface area of the CNF electrode, which were estimated using the method described by Krejci *et al.*[40] for planar carbon electrodes to be nearly 8 times the active surface area of the Toray. Another contributing factor to the difference in performance could be a result of the disparity in electron transport efficiency between the Toray and CNF electrodes, which can be seen in the behavior of the cyclic voltammograms. In Figure 3.3, both LAC1 and LAC2 CNF biocathodic current densities plateau at 0.5 V *vs*. Ag/AgCl under hydrodynamic conditions, which can be interpreted as the reaction rate of the electrodes matching the mass transport rate of molecular oxygen to the surface of the electrodes. These plateaus are not present in the cyclic voltammograms of the Toray bioelectrodes under the same conditions in Figure 3.2. Instead, the current density continues to linearly rise after 0.5 V *vs.* Ag/AgCl, indicating that the reaction rate is slower than the mass transport rate. Since both Toray and CNF electrodes were tested under the same hydrodynamic conditions and the laccases were immobilized in the same manner, these results are very likely a symptom of better electron transport kinetics of the CNF bioelectrodes than that of the Toray bioelectrodes. Since the CNF electrodes consistently outperformed the Toray electrodes, the remaining characterization steps (*i.e.* pH, and temperature dependency and stability at elevated temperature and in presence of inhibitors) were performed on the CNF electrodes only.

LAC1 and LAC2 bioelectrodes exhibited an onset potential of +655 ± 4.29 mV and +675 ± 22.4 mV *vs.* Ag/AgCl, respectively, which are among the highest onset potential reported for

any laccase bioelectrode to date [132]–[135]. The TvL bioelectrodes, by comparison, had an onset potential at +588 ± 8.47 mV *vs*. Ag/AgCl, which is very close to the known redox potential of TvL (600 mV *vs.* Ag/AgCl) and therefore these results also indicate very efficient direct electron transfer processes between the TvL and electrodes. [101] Both LAC1 and LAC2 electrodes outperformed TvL electrodes in current density as well, which is expected as the calculated activity of the TvL solution (16.1 ± 8.62 KU L^{-1}) was much lower than activities of the LAC1 and LAC2 solutions.

Unexpectedly, LAC2 bioelectrodes only produced 58.8 ± 10.6% more current density than the LAC1 bioelectrodes, despite having over 3.5 times the specific activity (LAC2, after dilution by citrate/phosphate buffer, has an activity 1,450 ± 2.37 KU L^{-1} as opposed to 411 ± 3.16 KU L^{-1} of the LAC1). This result was consistent for both the Toray and CNF electrodes, which may indicate improved DET between the LAC1 and the MWCNT than between LAC2 and MWCNT. Further comparison between LAC1 and LAC2 can be made when examining their behaviors after reaching their maximum turnover rates, the mass transported regime of the cyclic voltammetry, which appears to occur when E > 0.4V *vs*. Ag/AgCl. A slight drop in current density could be seen in the LAC1 CNF electrodes under all conditions besides continuous oxygen bubbling whereas a slight increase in current density is observed in LAC2 CNF electrodes under all conditions. Due to similar architecture of the electrodes, these results seem to indicate a better electron transfer efficiency between LAC1 and the CNF electrodes than LAC2 and the CNF electrodes. The exact nature as to why LAC1 have observably better electron transfer efficiency with CNF electrodes thanLAC2 has with CNF electrodes is uncertain and may be due to differences in the molecular structure of the isoforms that affects their interaction with the AC-MWCNT.

Future studies on the molecular structures of the two enzymes may bring further insight to this disparity.

It is also interesting to note that even under continuous argon bubbling, the current density does not substantially drop below the current density under hydrostatic conditions whereas under the same conditions the TvL electrodes showed no signs of oxygen reduction current. It is unlikely that the current density is a result of anything but oxygen reduction because the citrate/phosphate buffer does not contain any known reduction substrate of laccase besides dissolved oxygen. While convection generated by continuous argon bubbling could contribute partly to the elevated current, these results seem to indicate that these new isoforms of laccase are particularly sensitive towards oxygen reduction.

3.1.3.2 Optimization of CNF bioelectrode performance

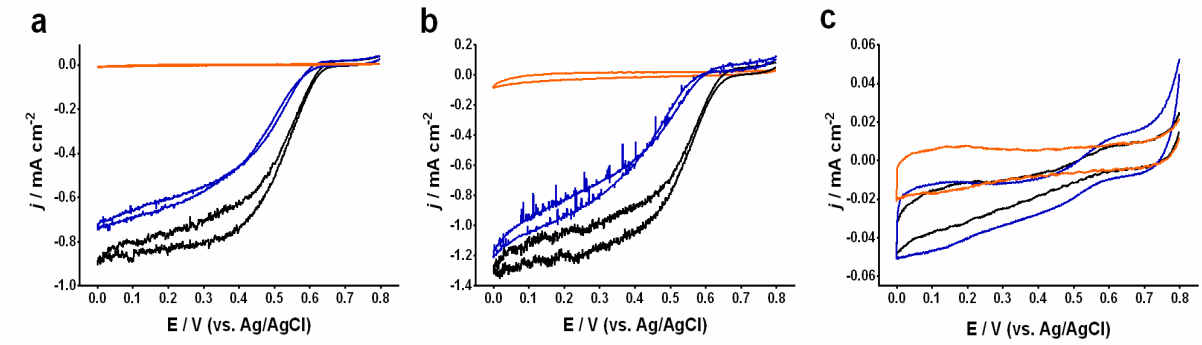

Figure 3.4. Representative cyclic voltammograms of (a) LAC1, (b) LAC2, and (c) TvL on (black) CNF bioelectrodes that were wetted prior to laccase immobilization in citrate/phosphate buffer pH 4.0 at 1 mV/s under continuous oxygen bubbling, (blue) on CNF bioelectrodes without wetting and under hydrostatic conditions, (orange) CNF bioelectrodes without enzyme under hydrostatic conditions. Reproduced with permission from *[128]*.

Initial cyclic voltammograms of the CNF electrodes showed a lower onset potential than that of the Toray electrodes (47.4 ± 8.60 mV lower) (Figure 3.4). However, the immobilization on both Toray and CNF electrodes are identical, therefore it is believed the drop in onset potential is mostly like a result of the difference between absorption process of the LAC-AC-MWCNT on to Toray electrodes to that of LAC-AC-MWCNT to CNF electrodes. One way to improve adsorption of the LAC-AC-MWCNT on to the CNF electrodes is to immerse the CNF electrodes in citrate/phosphate buffer pH 4.0 for an hour then left to dry for 10 minutes prior to the first application of LAC-AC-MWCNT solution. Immersion in a buffer solution improves the wettability of the CNF electrodes by removing adsorbed gas molecules from the surface of the carbon nanofibers and therefore reduce the inter-particle distances between the moieties. The reduced distance can significantly reduce the contact resistance between the AC-MWCNT and CNF electrode and consequently affect the catalytic current observed.[136] The new protocol was successful and not only improved the onset potential but also increased the current density for both LAC1 and LAC2 electrodes by 147 ± 86.1 $\mu A/cm^2$. No noticeable improvements were observed when this protocol was applied to the Toray electrodes.

To maximize enzyme loading of the bioelectrodes, multiple coatings of the LAC-AC-MWCNT (each painted 15 min after the subsequent coat) was evaluated in an attempt to improve the performance of the bioelectrodes. It was observed that a second coat of the LAC-AC-MWCNT solution did increase the current density of both LAC1 and LAC2 CNF electrodes by 186 ± 87.4 $\mu A/cm^2$, however no improvements were observed for both TvL electrodes and Toray electrodes. Additional applications after the second layer yielded negligible increases in current densities and therefore the protocol was adjusted to include two

applications of the LAC-AC-MWCNT. All results shown are measured from bioelectrodes prepared using the optimized procedure outlined here.

3.1.3.3 Effects of pH and temperature on performance of LAC1 and LAC2 bioelectrodes

Cyclic voltammetry was used to measure the performance of the LAC1 and LAC2 bioelectrodes in citrate/phosphate buffer at pH 4.0, 4.5, 5.0, 5.5 and 6.0 (Figure 3.5). The pH dependency of the bioelectrodes mirrors the results of the activities of LAC1 and LAC2 at these pH values, as measured by ABTS in the studies conducted by Ramirez *et al*.[30] Although the non-immobilized LAC1 and LAC2 reported by Ramirez *et al*. remained very stable at neutral pH, the activity losses seen in both LAC1 and LAC2 bioelectrodes after testing at pH 6 and higher were permanent. Signs of performance loss due to higher pH can also be seen in the drop in onset potential. At pH 6, there is no observed net increase in current density between hydrodynamic test and oxygen bubbling test (results not shown).

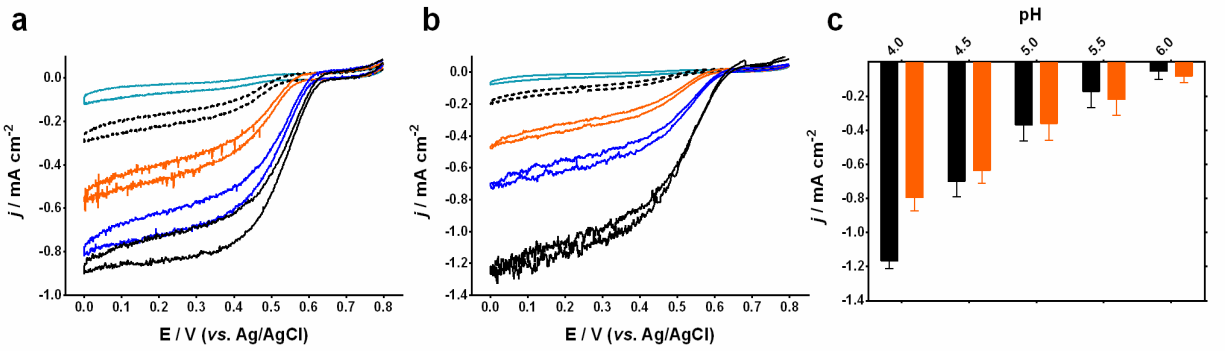

Figure 3.5. Representative cyclic voltammograms of (a) LAC1, and (b) LAC2 on CNF bioelectrodes at 1 mV/s in citrate/phosphate buffer under continuous oxygen bubbling at pH 4.0 (solid black), pH 4.5 (blue), pH 5.0 (orange), pH 5.5 (dashed black), and pH 6.0 (sky blue). (c) Statistical comparison of the current density of all

the cyclic voltammetry tests measured at 0.2 V vs. Ag/AgCl (orange) LAC1, and (black) LAC2. Reproduced with permission from *[128]*.

Similarly, cyclic voltammetry was used to evaluate the temperature effects on the LAC1 and LAC2 bioelectrodes in citrate/phosphate buffer pH 4 at temperatures of 40°C, 50°C and 60°C (Figure 3.6). In this case, the performance of the bioelectrodes did not meet the results reported by Ramirez *et al.,*[30] where optimal range of temperature for both isoforms were from 40°C to 60°C. The performance of the bioelectrodes showed the highest current density at 20°C and lost more than 50% of their current density at 50°C and higher. In particular, LAC2 bioelectrodes lost all activity at 50°C and higher. Several factors could explain this discrepancy in data: (1) the improved activity at elevated temperature of laccases reported by Ramirez *et al.*[30] could be attributed to the hydrostatic conditions were the UV/Vis spectrophotometric measures were performed, (2) electrochemical measurements may include partial denaturation of the laccase due to lower stability at higher temperature and could result in the difference in activity measurement. This becomes more evident at 60 °C (results not shown), where significant losses in LAC2 biocathodic activities were observed between the two scans in one cyclic voltammetry test and (3) the saturation concentration level of dissolved O_2 is much lower at elevated temperatures, which will contribute to drop in current density seen in the results.

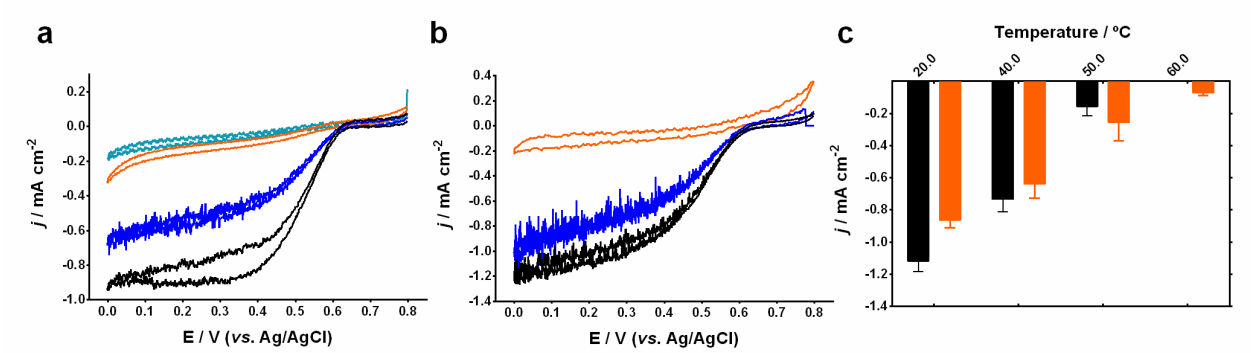

Figure 3.6. Representative cyclic voltammograms of (a) LAC1, and (b) LAC2 on CNF cathode at 1 mV/s in citrate-phosphate buffer at pH 4.0 under continuous oxygen bubbling at 20°C (solid black), 40°C (blue), 50°C (orange), and 60°C (sky blue). (c) Statistical comparison of the current density of all the cyclic voltammetry tests measured at 0.2 V *vs.* Ag/AgCl (orange) LAC1, and (black) LAC2. Reproduced with permission from *[128]*.

3.1.3.4 TvL, LAC1 and LAC2 bioelectrode Stability

The stabilities of the electrodes were examined by potentiostatic evaluation of the current densities measured above what is inferred as the maximum turnover rate of the enzyme at 0.4 V *vs.* Ag/AgCl in citrate/phosphate buffer at pH 4.0. The TvL, LAC1 and LAC2 bioelectrodes were first evaluated at 20°C for 12 hours (Figure 3.7). Potentiostatic evaluation was chosen over galvanostatic evaluation as a means to compare the electrochemical stability to the stability found by Ramirez *et al.*[30]

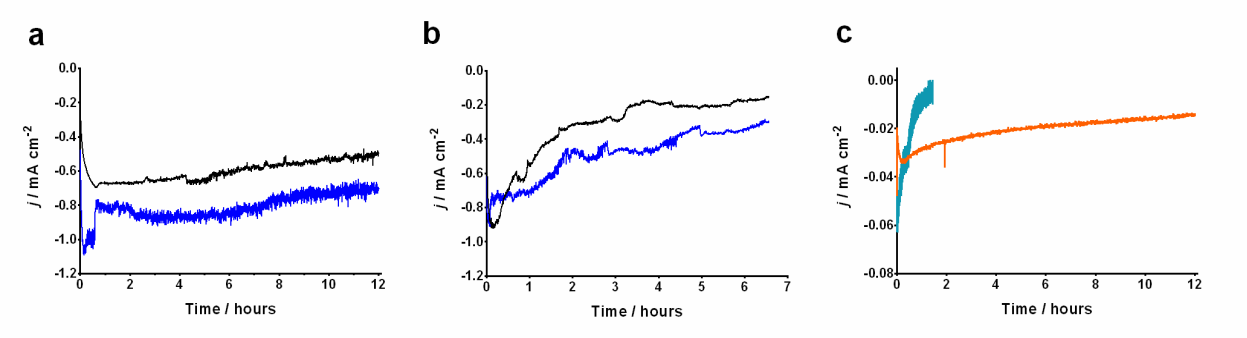

Figure 3.7. Representative potentiostatic chronoamperometry of LAC1 (Black), and LAC2 (Blue) on CNF cathode at 0.4 V vs. Ag/AgCl in citrate/phosphate buffer at pH 4.0 under continuous oxygen bubbling at (a) 20°C, and (b) 45°C. (c) Representative potentiostatic chronoamperometry of TvL on CNF cathode at 0.4 V vs. Ag/AgCl in citrate/phosphate buffer at pH 4.0 under continuous oxygen bubbling at 20°C (orange), and 45°C (sky blue). Reproduced with permission from *[128]*.

Both LAC1 and LAC2 electrodes exhibited higher stability than the TvL electrodes, losing 25.6 ± 10.6% and 21.0 ± 9.9% of their maximum current density, respectively, as opposed to the 43.2 ± 13.6% loss in current density experienced by the TvL electrodes after 12 hours. The LAC1 and LAC2 bioelectrodes also exhibited improved stability compared to the non-immobilized LAC1 and LAC2 reported in Ramirez's study, in which both LAC1 and LAC2 lost nearly 50% of their activity after being stored for 10 hours in pH 4.0 citrate buffer. The decreases in current densities observed at the 30 min mark were consistent with all of the electrodes. It is expected that this drop in current is a combination of enzyme leaching until steady-state combined with electrode equilibration processes (such as hydration).

The stabilities of the LAC1, LAC2 and TvL bioelectrodes were also evaluated at 45°C for 6 hours, in citrate/phosphate buffer at pH 4.0. At elevated temperature, the TvL electrodes

lost 91.6 ± 5.5% of their initial current densities within 1.38 ± 0.31 hours. The LAC1 and LAC2 bioelectrodes were more resilient and lost 92.1 ± 8.7% and 69.0 ± 3.0% (respectively) of their current densities after 6 hours of testing.

3.1.3.5 LAC-AC-MWCNT Leaching study

The effect of the laccases and LAC-AC-MWCNT leaching from the CNF electrodes on the stability of the electrodes was estimated by evaluating the UV absorbance at 280 nm of a 1 mL aliquot taken during stability testing at various intervals. The absorbance is compared to that of a control solution that contains the maximum possible concentration of LAC-AC-MWCNT immobilized onto any electrode.

The results of the study as seen in Figure 3.8 and Table 3.1 shows that there is a lapse of time (at 30 min under temperature of 20°C and at 5 min under 45°C during which the electrode leaching rate is substantially higher than the rest of the study. When juxtaposing this period of high leaching to the result of the stability test, the high leaching period coincides with the period of time at which the current density is still increasing. At 20^{o}C and after 30 min, the current density reaches steady state and similarly enzyme leaching for LAC1, LAC2 and TvL begins to plateau. However, at 45^{o}C, the leaching rate is not only larger, but also does not plateau after the current density begins to drop. These results indicate that the leaching at 20^{o}C does not contribute significantly to loss in current density after the steady state is reached, but do partially contribute to the loss in current density at 45^{o}C. Additionally, the leaching rate after steady state (the slopes of the leach percentage in Figure 3.8) of all 3 isoforms of laccases are similar in magnitude at both 20 ^{o}C and 45 ^{o}C, which indicates the disparity in rate of current density loss between TvL and LAC1 and

LAC2 is a result of the lower thermostability of the TvL. To better visualize the percentage of leaching after the steady state is reached, the initial leaching before steady state was subtracted and the results of steady state leaching are indicated by the dashed line in Figure 3.8.

A working theory as to why a noticeable drop in current occurs right before steady state current is achieved at 20 ^{o}C could be a result of the large initial leaching that occurs prior to steady state. The large leaching rate may cause the current density to overshoot the steady state current, since a large portion of the adsorbed laccase that was initially contributing to the current density is leached away. Leaching becomes more severe at higher temperature, which explains why this drop in current density occurs much sooner at 45^{o}C. This theory also concurs with earlier observations that additional applications of the LAC-AC-MWCNT slurry after the second coating are ineffective in increasing the performance of the respective electrode. These results coupled with the consistency in current density achieved by the bioelectrodes seem to indicate that the maximum enzyme loading is almost self-regulating, as the excess enzymes are quickly leached off.

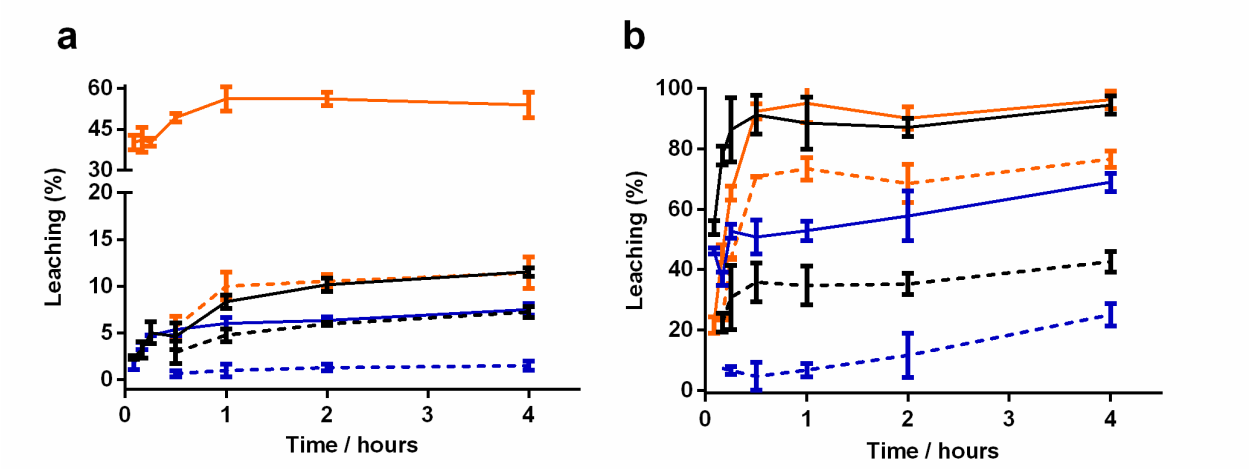

Figure 3.8. Leaching study under continuous oxygen bubbling for LAC1 (Black), LAC2 (Blue) and TvL (orange) electrodes. (solid line) Full leaching percentage. (dashed line) Percentage of leaching during steady state at (a) 20°C and (b) 45°C . Reproduced with permission from *[128]*.

At room temperature, percentage leaching was 7.71 ± 4.5% and 1.21 ± 0.78%, respectively, after 4 hours of continuous testing (measured after steady state). Leaching is substantially higher at 45°C, with LAC1 and LAC2 leaching off of 40.6 ± 2.9 and 27.7 ± 3.2%, respectively, (also measured after steady state). The test also demonstrated that the improved stability of the LAC2 electrodes over the LAC1 electrodes is a result of larger enzyme leaching occurring in the LAC1 electrodes and not because of the stability of the LAC1 itself. This result agrees with the results presented by Ramirez's work[30], where it was shown that LAC1 has higher thermal stability than LAC2. Since both isoforms were immobilized under the same conditions, this result may point to stronger docking mechanism between the LAC2 and the anthracene. It is also important to note that the electrochemical testing of the electrodes may also have an impact on the leaching of the enzyme, which is not factored into this study.

Table 3.1. Leaching rate and final percentage of enzyme loss during stability test at 20°C and 45°C (before and after subtracting initial leaching). Reproduced with permission from *[128]*.

T (°C)	Total leaching			Steady State leaching		
	Leaching Percentage (%)			Leaching Percentage (%)		
	TvL	Lac 1	Lac 2	TvL	Lac 1	Lac 2
25 °C	56.2 ± 2.42	11.3 ± 5.19	7.08 ± 0.742	11.9 ± 1.44	7.71 ± 4.45	1.21 ± 0.780
45 °C	98.3 ± 0.03	94.5 ± 3.04	74.0 ± 8.27	76.6 ± 2.68	40.6 ± 2.93	27.7 ± 3.21

3.1.3.6 Laccase inhibition – Spectroscopic assays

The inhibition of laccase by different agents (*i.e.* H_2O_2, NaF and KCl) was investigated spectrophotometrically, using ABTS as an electron mediator at different concentrations. Figure 3.9 presents apparent Michaelis-Menten kinetics, determined by non-linear regression fits for the oxidation of ABTS under different concentrations of inhibitors.

Figure 3.9 revealed that H_2O_2 increases the apparent K_M while decreasing the apparent V_{max} of laccase, suggesting that H_2O_2 acts *via* noncompetitive inhibition, which is confirmed by the Lineweaver-Burk double-reciprocal plot (Figure 3.10), where the convergence on the abscissa is characteristic of a noncompetitive inhibition model, obtaining a K_i value of 29.5 and 31.4 mM for LAC1 and LAC2, respectively). Milton and Minteer,[46] suggested in a previous study, that the inhibition mechanism of H_2O_2 fitted to a mixed inhibition model (subcategory of noncompetitive inhibition). The reversibility of the inhibition of laccase by

H_2O_2 has previously been demonstrated by recovering the enzymatic activity by the rapid decomposition of H_2O_2 by catalase.[24]

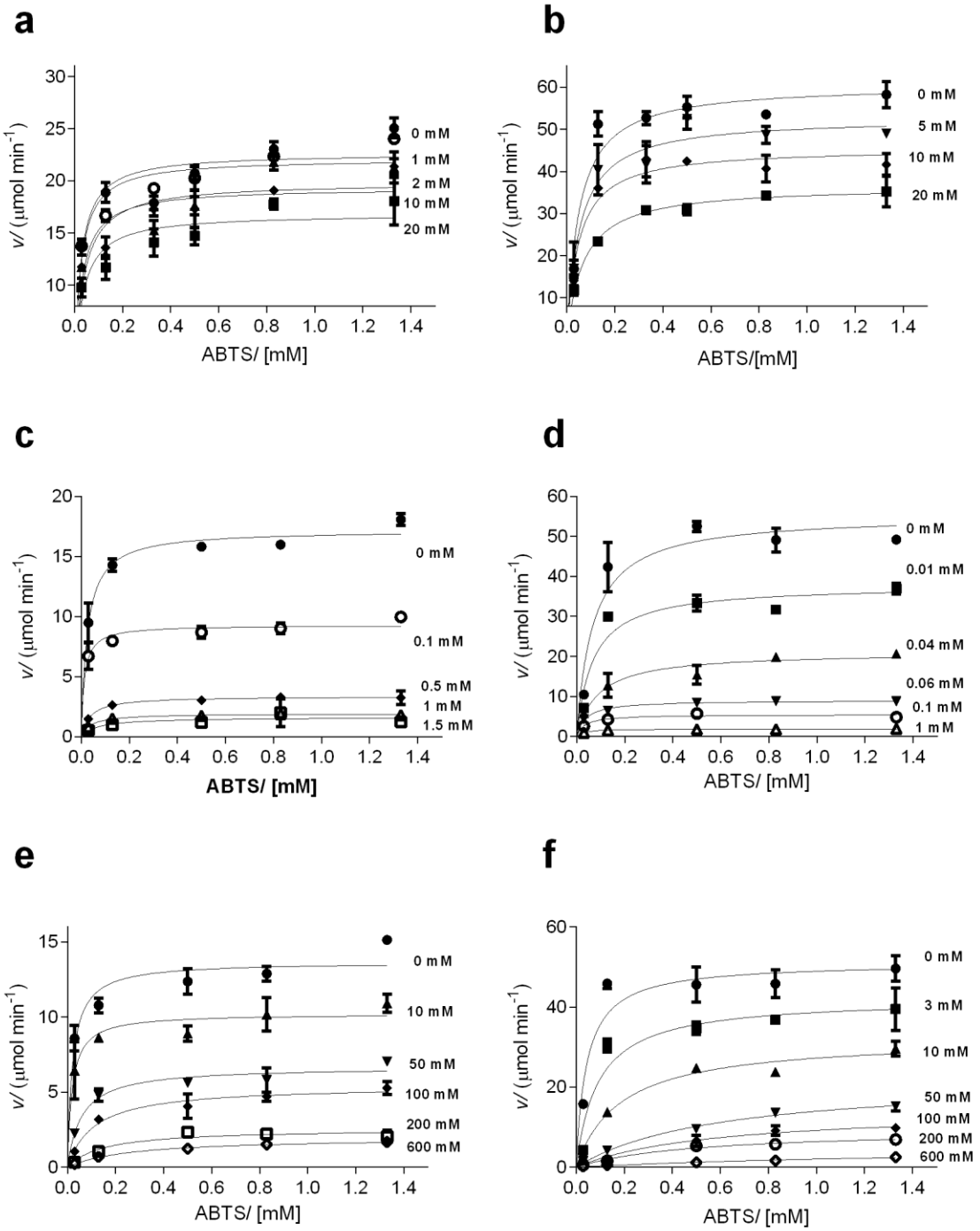

Figure 3.9. Spectroscopic determination of apparent Michaelis-Menten kinetics for the biocatalytic reduction of O_2 by laccase in presence of different inhibitors (a)LAC1 in H_2O_2, (b) LAC2 in H_2O_2, (c) LAC1 in NaF, (d)

LAC2 in NaF , (e) LAC1 in KCl, (f) LAC2 in KCl monitored using ABTS phosphate/citrate buffer (pH 4, 0.1 M). Reproduced with permission from *[128]*.

As expected, an inhibitory effect of fluoride was clearly observed at low concentrations (K_i = 0.0724 and 0.0184 mM for LAC1 and LAC2, respectively). Fluoride acts as a non-competitive inhibitor by binding to the T2/T3 copper cluster, blocking the electron transference pathway from the T1 site to the T2/T3 cluster.[47] According to Lineweaver-Burk double-reciprocal plot, it was found that Cl^- acts as competitive inhibitor, since the convergence of the data points on the ordinate axis is typical of a competitive inhibition model (see Figure 3.10). This result indicates that contrary to the inhibition by F^-, Cl^- ions interact with the T1 Cu site of the enzyme and (in the competitive inhibition mechanism) Cl^- ions compete with electron donors for access to the T1 redox center of the enzyme, reducing the observed activity.[48]

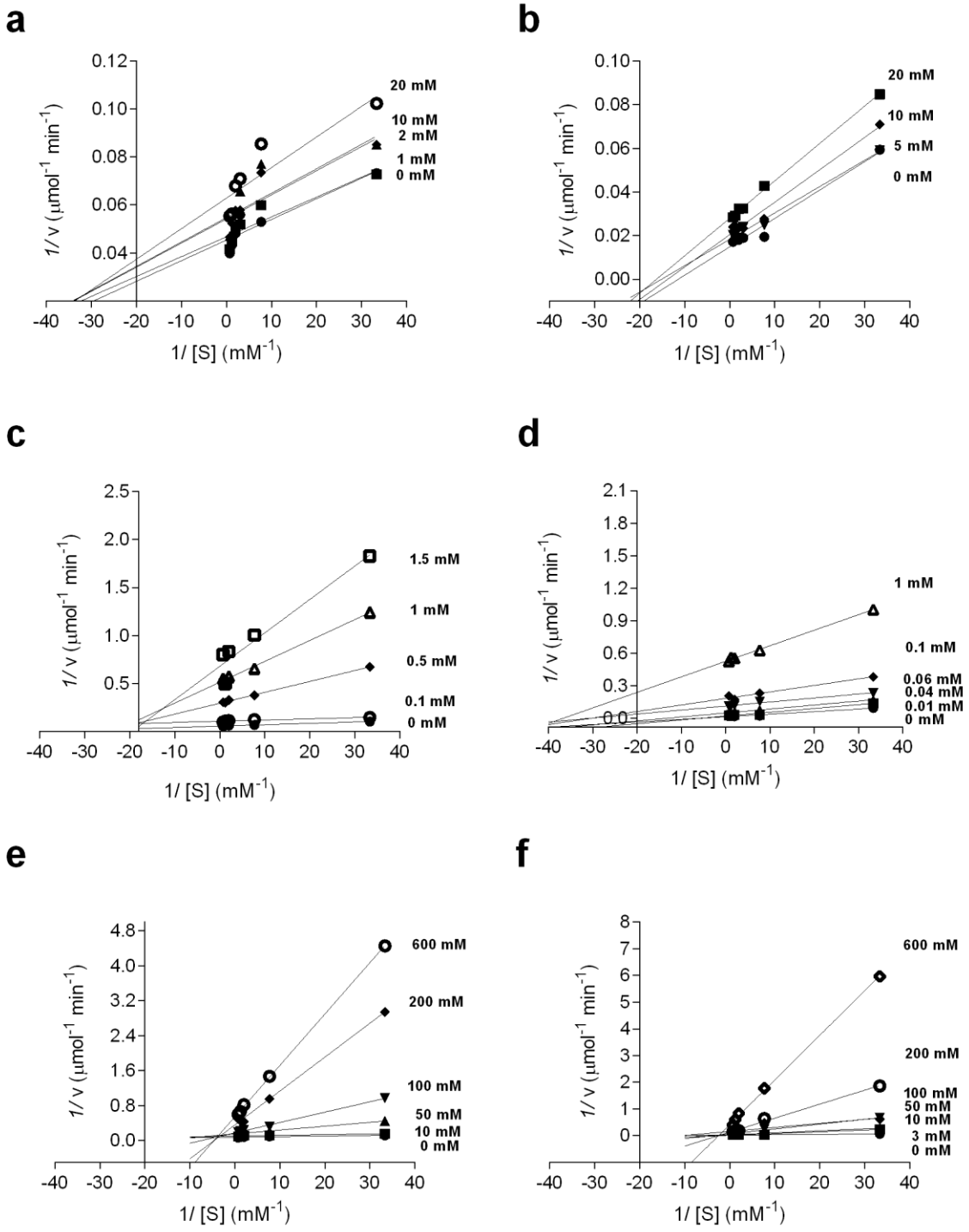

Figure 3.10. Lineweaver-Burk double reciprocal plot for the biocatalytic reduction of O_2 by laccase in presence of different inhibitors (a) LAC1 in H_2O_2, (b) LAC2 in H_2O_2, (c) LAC1 in NaF, (d) LAC2 in NaF , (e)

LAC1 in KCl, (f) LAC2 in KCl monitored using ABTS phosphate/citrate buffer (pH 4, 0.1 M). Reproduced with permission from *[128]*.

3.1.3.7 Electrochemical Inhibition studies

The LAC1, LAC2 and TvL bioelectrode's tolerances to three well-known laccase bioelectrode inhibitors (*i.e.* chloride, fluoride and hydrogen peroxide) were evaluated by potentiostatic analysis of the current densities (Figure 3.11). The citrate/phosphate buffer (pH 4.0) was purged with ultra-pure argon gas for 10 minutes, prior to testing. At 1000 seconds, 0.2 mM ABTS was added to the solution in order to determine the amount of immobilized laccase that was not contributing to DET. ABTS is a commonly used electron mediator for laccase that facilitates mediated electron transfer (MET) between laccase and an electrode. [133], [140] The lack of increase in the current density after the introduction of ABTS indicates a lack of MET occurring between any active laccase present on the electrode surface that does not undergo DET, further suggesting that the majority of active laccase within the electrode architecture undergoes DET.

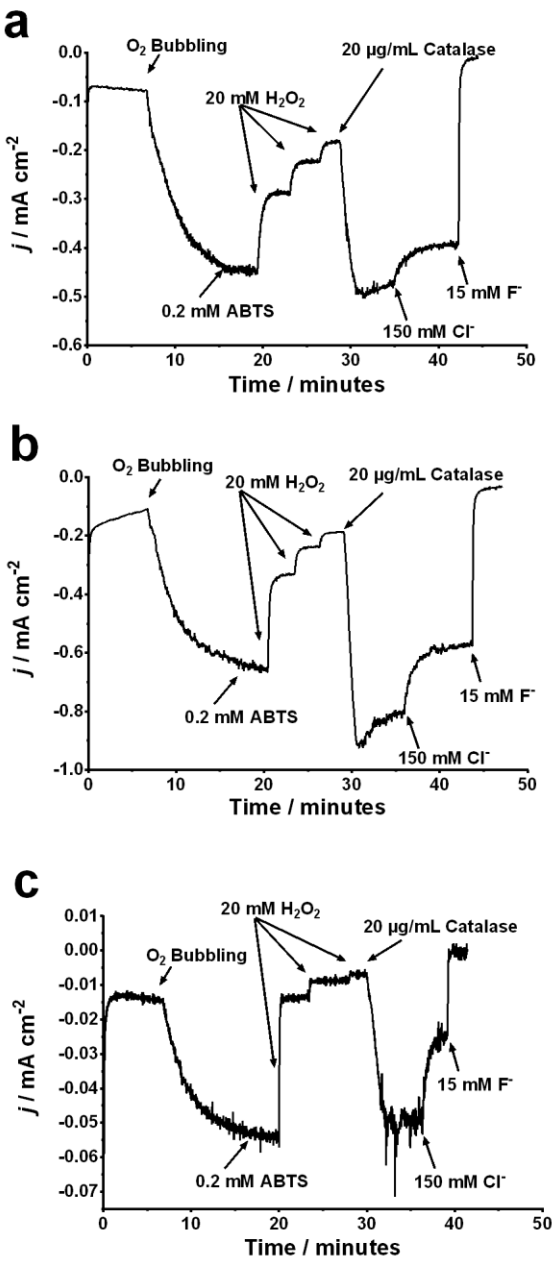

Figure 3.11. Representative potentiostatic chronoamperometry of (a) LAC1, (b) LAC2, and (c) TvL on CNF cathode at 0.4 V *vs.* Ag/AgCl in citrate-phosphate buffer at pH 4.0 at 20°C. Citrate/phosphate buffer was purged of oxygen by bubbling ultra-pure argon into solution for 10 minutes before test began. Oxygen bubbling was initiated at 400 secs into experiment and continuously ran until the end of the experiment.

ABTS, H_2O_2, catalase, KCl and KF were sequentially added at the times labeled in the graph. Reproduced with permission from *[128]*.

Both LAC1 and LAC2 demonstrated more resilience to traditional laccase inhibitors than TvL, such as chloride and hydrogen peroxide. LAC1 and LAC2 lost 26.5 ± 10.6% and 42.7 ± 7.8% (respectively) of their maximum current densities after the introduction of 20 mM of hydrogen peroxide and a 45.1 ± 17.3% and 63.6 ± 14.2% loss in current densities after the addition of 60 mM hydrogen peroxide. In comparison, TvL electrodes exhibited a 62.3 ± 11.2% loss after the first 20 mM of hydrogen peroxide and 87.6 ± 11.3% loss in current densities after 60 mM. The loss in activity was quickly recovered after the removal of hydrogen peroxide from the solution by the introduction of catalase, indicating that the loss in activity was not due to denaturation of the enzymes but rather their inhibition by H_2O_2, which corroborates with the results previously found by Milton *et al.* and Calvo *et al.*[15,23,24] The large growth in current densities following the introduction of catalase could be attributed to the production of oxygen by the catalase, and thus, increased localized dissolved O_2 concentrations. However, these results contradict the results of the spectroscopic assays, which indicated by the K_i that the resistances of the two isoforms to H_2O_2 were similar (*i.e.* K_i of 29.5 ± 1.62 mM and 31.4 ± 1.62 mM for LAC1 and LAC2, respectively). It is unknown why there is such a discrepancy in the data.

Similarly, LAC1 and LAC2 exhibited a 24.6 ± 5.0% and 32.1 ± 5.0% drop in current density after 150 mM of KCl was added to the solution while TvL had a 64.0 ± 16.2% drop in current density. All three laccase bioelectrodes experienced complete losses in current densities following the addition of 15 mM KF, which were also not permanent losses as the current densities were restored after replacing the solutions with fresh citrate/phosphate

buffer. Although the results of the chlorine inhibition also contradicts the results of the spectroscopic assays, this discrepancy is expected as it was reported in Blanford's original anthracene immobilization paper that anthracene immobilization significantly improved the resistance of laccase to inhibition by chlorine ions[105].

3.1.4 Conclusion

The first electrochemical characterization of bioelectrocatalytic oxygen reduction by the recently-isolated isoforms of laccase from *Pycnoporus sanguineus CS43* was reported. Two isoforms (LAC1 and LAC2) of laccase from *P. sanguineus CS43* were immobilized onto carbon nanofiber (CNF) mat electrodes using anthracene-modified multi-walled carbon nanotubes (AC-MWCNT) and their performances were juxtaposed with TvL immobilized on CNF electrodes using the same process. The AC-MWCNT helps facilitate direct electron transfer (DET) between the CNF and laccase allowing the characterization of the electrochemical properties of the immobilized enzymes. The CNF electrodes demonstrated improved apparent reaction kinetics than commercially available Toray carbon paper electrodes, which allowed a better gauge of the performances of the immobilized laccases.

The results showed that LAC1 and LAC2 have remarkable tolerance to a wide range of different operational conditions, e.g. pH, temperature and inhibitors agents. The LAC1 and LAC2 bioelectrodes retained some activity up to pH 6 (LAC1 and LAC2 have optimal pH range from 2.0 to 4.0) and exhibited substantially improved stability as compared to the TvL electrodes in the entire temperature range investigated. Furthermore, LAC1 and LAC2 electrodes exhibited some of the highest onset potentials (+655 ± 4.29 mV and +675 ± 22.4

mV *vs.* Ag/AgCl, respectively) of all laccase bioelectrodes reported to date, maintaining high current densities even in the presence of several common inhibitors.

The high thermostability, onset potential, current density and resilience to inhibitors are all very attractive qualities for biofuel cell cathode applications. Specifically, their tolerances towards hydrogen peroxide would be very beneficial for such applications as bioelectrodes for glucose biofuel cells where glucose oxidase anodes have been shown to produce significant concentrations of hydrogen peroxide.[50] Future studies will be focused on improving the interaction between the LAC-AC-MWCNT with the CNF electrodes through surface and chemical modifications of the CNF electrodes to promote better electron transfer between the laccase and electrode. Alternatively, other immobilization schemes could be explored for improving the performances of the bioelectrodes.

3.2 Embedding Metal Nanocatalysts

3.2.1 Introduction

Though the described Laccase-CNT paste functionalization method was successful, the process is not applicable to all forms of C-MEMS electrodes. For instance, adapting such a technique to enhance the performance of IDEAs would be particularly difficult due to the small microfeatures and necessity to keep the two working electrodes electrically isolated.

Furthermore, this technique lacks stability, due to leaching of the loosely-bound catalysts, and large ohmic losses from poor contact between the CNT and C-MEMS electrodes. Another approach that have been explored by few research groups, is embedding metal nanoparticles directly into the nanofibers. One of the earliest studies on this type of functionalization was done by Reneker et al. who mixed an iron salt into a polyacrylonitrile (PAN), and electrospun the solution in nanofiber mats[141]. The mats were then thermally treated in a reducing environment containing a mixture of hydrogen and nitrogen to reduce the iron salts into nanoparticles. The mats were subsequently pyrolyzed in an inert nitrogen environment at a much higher temperature to convert the polymer fibers into carbon nanofibers. The embedded iron nanoparticles were then used as catalysts for the growth of carbon nanotubes.

Embedding nanoparticles have several advantages such as better surface coverage, improved contact with the catalysts and improved stability of catalysts[142]–[145]. However, the process outlined previously has a few flaws; it offers limited control on the uniformity of the nanoparticle coverage, as well as low flexibility on the size and spacing between individual nanoparticles. Moreover, the process is not compatible with all types of metal nanoparticles. In this work, we aim to enhance this microfabrication technique by implementing block copolymers (BCP) as the carbon precursor instead of PAN. We used Poly(styrene-co-4-pyridine) because its low carbonization temperatures make it more compatible with a larger range of metal nanoparticles. Furthermore, the amphiphilic nature of this block-co-polymer allows for better control over the size and spacing between each nanoparticle, enabling us to optimize these parameters for improved catalysis performances.

3.2.2 Result and Discussion

The capability of Block copolymers to automatically assemble to a myriad of organized nanostructures has established them as a prominent category of self-assembly materials. Implementing block copolymers provides nano-engineers with effective bottom-up processes to fabricate nanometer-scale structures. Moreover, tunabilty of block copolymers in terms of size, shape, and chemical nature of micro-domains allows for their use as templates and incorporation of different functionalities into the resulting microfabricated structures.

In this work, Carbon nanofiber mats embedded with metal nanoparticles were synthesized from of the carbonization of poly (styrene-b-4-pyridine). PS-b-P4VP nanofibers were fabricated via the electrospinning. Metal ions was loaded into the pyridine islands by soaking the mats in a ferric chloride or gold (III) chloride solution followed by UV stabilization of metal salt loaded polymer. In general, the chemical nature of the minor block which achieved through proper selection of constituent polymers, guarantees selective absorption of the catalytic ions to desired microdomains and not to the matrix (major block) in BCP film[146], [147].

The electrospun polymer fibers are then carbonized in a single step via thermal treatment in an inert environment. For this procedure, PS-P4VP block co-polymer was purchased from Polymer Source, Inc. Metal Salts, Ferric Chloride and Gold (III) Chloride, were purchased from Sigma Aldrich.

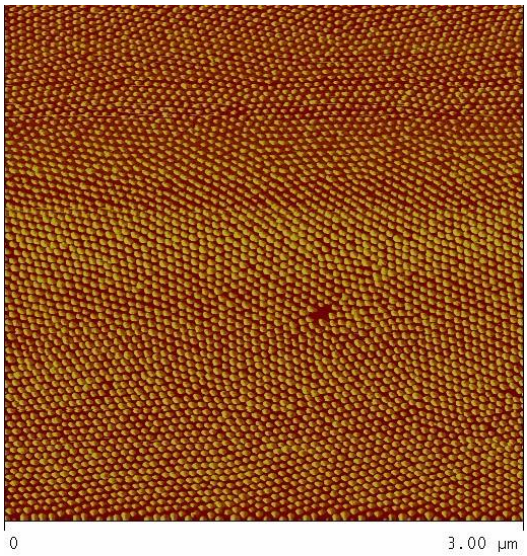

Figure 3.12. AFM image of gold particles arrays achieved by using PS-b-P4VP (69K) cylindrical block copolymers domains as scaffold. Reproduced with permission from [94].

Figure 2.8 shows the schematic of the electrospinning setup used to develop block-co-polymer nanofiber mats. The polymer reservoir is held using a 5 mL syringe, which is mounted on the [syringe pump] that controls the rate at which the polymer is supplied to the tip of the spinneret. The spinneret is a ½ inch, 21 gauge, and stainless steel needle. The voltage is supplied to the spinneret using a high voltage power supply purchased from Information Unlimited. The collector consisted of p-type silicon wafer mounted on a copper plate, which is grounded with respect to the spinneret.

The electrospinning parameter were experimentally determined and optimized for uniformity of fiber thickness and coverage. 15 wt.% PS-b-P4VP is electrospun onto the collecting substrates, a 1 cm^2 p-type silicon pieces affixed to a 100 cm^2 grounded copper plate. The collector is placed at a working distance of 10 cm away from the spinneret, which is held at 15 kV with respect to ground. Figure 3.13a indicates the scalability the electrospinning microfabrication technique. As shown, the size of the fabricated block

copolymer mat is controllable and depends on the electrospinning stage. Figure 3b shows the uniformity of the electrospun fibers across the mat, which is fundamental factor in achieving uniform electrical, thermal and mechanical properties in the resulting mat. Furthermore, figure 3.13c demonstrates the morphology and diameter of individual BCP fibers. The dimeter of fibers may be tuned by adjusting key electrospinning parameters such collector working distance and applied voltage.

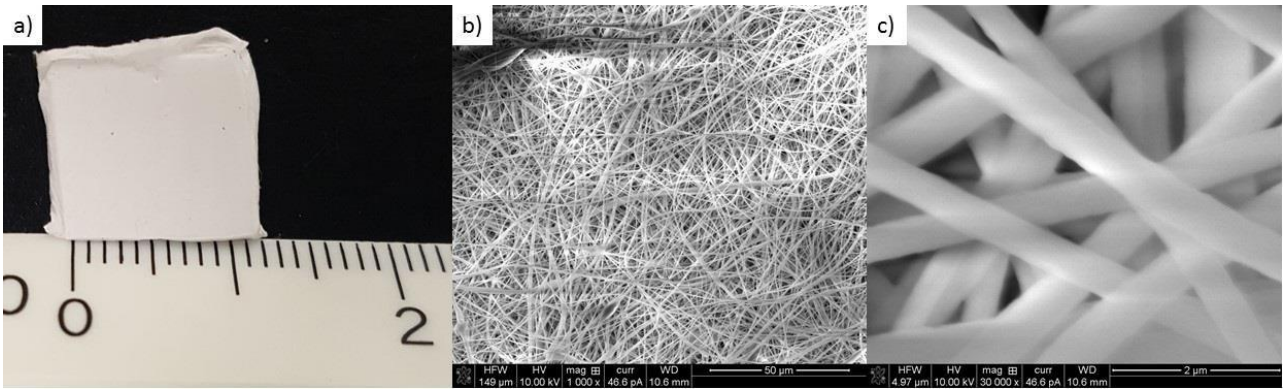

Figure 3.13. a) image of the PS4VP fiber mats on the 1 cm^2 silicon piece. b) and c) SEM images of the PS4VP fibers mat. Reproduced with permission from [94].

Figure 3.14 shows the carbonized PS4VP nanofibers with embedded metallic nanofibers. These results show the promise of the process, however, not all the fibers survived the pyrolysis intact as evident by the loss in morphology in figure 3.14 b. The loss in morphology likely stems from the crude method with which the PS4VP was stabilized and may require much more powerful UV lamp. To further, exacerbate this the metallic salt are also capable of UV absorption and therefore reduce the amount of crosslinking with the PS4VP. Thus, further optimization is still required for this process.

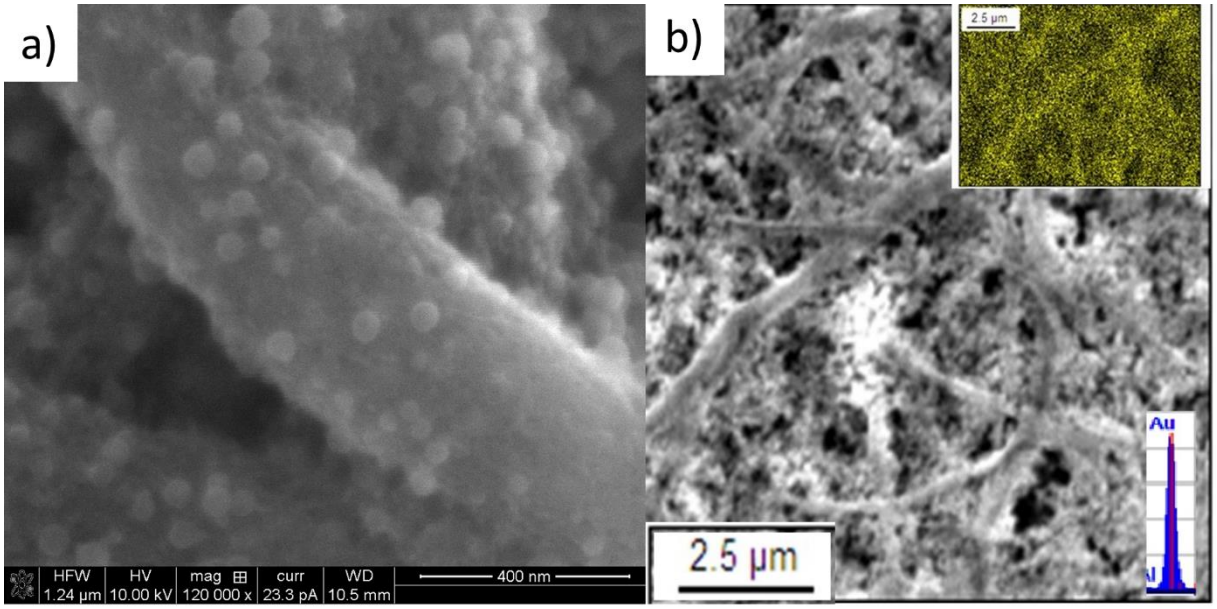

Figure 3.14. SEM image of Carbon Nanofibers Embedded with Nanoparticles. a) Close up SEM image of carbon nanofibers embedded with nanoparticles and b) EDS micrograph of gold nanoparticles within the carbon nanofiber matrix.

3.2.3 Conclusion

These presented results are particularly promising for fuel cell application and electrode fabrication. Embedded nanoparticle not only improves the active surface area and reduces ohmic losses but also provides a simple, scalable fabrication process for creating a highly porous electrode. For biofuel cells and biosensors, gold nanoparticles are particularly attractive for their chemistry with thiol linker molecules and good compatibility with biological catalysts. Furthermore, the reduced pyrolysis temperature makes this process much more compatible with many more fabrication processes. The potential of growing carbon nanotubes from the iron nanoparticles also makes these electrodes very attractive for supercapacitor and battery applications due to their high surface area and fractal-like morphology.

Although preliminary, the results of this study point to a simple, flexible fabrication technique for a functionalized 3-dimension carbon nanostructure, which can potentially open the possibility of novel intricate electrodes designs without compromising fabrication complexity and electrode performance for various electrochemical applications. Though promising, there are still a few challenges with this process. First, the process is not compatible with all metallic nanoparticles as many of them have melting points much lower than the carbonization temperature of pyrolysis. While 680 ^{o}C is low enough to largely prevent gold nanoparticles from melting, the carbon microstructure is largely amorphous as the low temperature pyrolysis is unable to anneal away the disorder. Such forms of carbons would exhibit very low conductivity and electrochemical kinetics and such C-MEMS electrodes would like good electrochemical response.

4 – STUCTURAL MODIFICATION

4.1 Synthesis of Stress-Activated Pyrolytic Carbon

4.1.1 Introduction

The difficulty in functionalizing C-MEMS through surface modification prompted us to begin investigating methods to alter and tailor the carbon's microstructure to enhance its electrochemical performance. As previously discussed, commercial process has been developed for synthesizing highly graphitic carbon fibers from Pitch and Polyacrylonitrile(PAN) through heat treatment techniques to align the molecular structure of the precursor to enhance graphitization during their pyrolysis. However, these processes has largely remained non-compatible with C-MEMS fabrication processes. Alternatively, we demonstrate how the implementation of active effect by application of electrohydrodynamic forces and mechanical compressive treatment on a "non-graphitizing" polymer precursor can greatly enhance the degree of their graphitization during low temperature pyrolysis (1000 ^{0}C). In particular, we present a framework by which a traditionally known "non-graphitizing" polymer, Polyacrylonitrile (PAN), may be graphitized at low pyrolysis temperature, thereby challenging the current notion of graphitizing and non-graphitizing polymers. The choice of electrospinning process allows us to use electrohydrodynamic forces, enhanced by the addition of carbon nanotubes, to

unwind and orient the polymer molecular chains. In addition, electrospinning process is particularly adaptable to multiple C-MEMS processes. Once formed, the polymer nanofiber mat was thermally stabilized under calculated mechanical stress to preserve and enhance the alignment of the precursor's chains. A myriad of characterization methods, including transmission electron microscopy, Raman spectroscopy, ohmic resistance, and electrochemical measurements, were used to measure the degree of graphitization in pyrolyzed PAN specimens. The presented results demonstrate how the physical conditions exerted during the synthesis affect molecular alignment in a polymer precursor to markedly enhance its graphitizability. By revealing unexplored stress-based mechanisms for carbon graphitization, this work suggests that graphitizability is not solely a chemical property of organic precursors.

4.1.2 Material and Methods

4.1.2.1 Carbon Synthesis.

Electrospinning: For electrospinning PAN fibers, polyacrylonitrile (Sigma Aldrich) with molecular weight M_w = 150,000 g/mol was dissolved in DMF, N,N-dimethylformamide (Sigma Aldrich), at 40 ^{0}C for 24 hours to a final concentration of 8 wt.%. The solution for electrospinning CNT-infused PAN (PAN-CNT) nanofibers was prepared by dispersing MWCNT, multi-walled carbon nanotubes (Sigma Aldrich) with a diameter of 110-170 nm and a length of 5-9 μm, in DMF under ultra-sonication for 1 hour then stirred for 24 hours at 40 ^{0}C. Subsequently, PAN was dissolved into the DMF-CNT solution by stirring at 40 ^{0}C for 24 hours, to achieve a final concentration of 8 wt.% PAN and 1 wt.% MWCNT. Electrospinning for PAN and PAN-CNT solution was performed by loading the PAN or PAN-

CNT solutions, respectively, into a 1 mL syringe mounted on a syringe pump, which provided a flow rate of 0.7 mL/hour. An operating voltage of 15 kV was applied between a 21-gauge needle (820 μm outer diameter) and an 8x8 cm^2 aluminum plate, which was held at 15 cm away from the dispensing needle. The electrospinning process was run for 1 hour to form a ~100 μm thick PAN and PAN-CNT nanofiber mats, respectively.

Stabilization: PAN and PAN-CNT mats were peeled off the aluminum plate and then thermally stabilized on top of an alumina plate at 275 ^{0}C in an oven for 5 hours. For mechanically-treated PAN-CNT (M-PAN-CNT) samples, a PAN-CNT mat was subjected to a 200 kPa compressive stress between two alumina plates, while being stabilized in an oven at 275 ^{0}C for 5 hours.

Pyrolysis: All stabilized PAN nanofiber mats were pyrolyzed in a tube furnace with a continuous flow of Nitrogen at a rate of 4,600 sccm. First, the stabilized samples were heated to 300 ^{0}C at a 4.5 ^{0}C/min ramp rate and maintained at that temperature for one hour. Next, the temperature was increased to 1000 ^{0}C at a 2.5 ^{0}C/min ramp rate and held at that temperature for an hour before cooling down to ambient temperature at 10 ^{0}C/min rate.

4.1.2.2 Characterization.

The pyrolyzed polymer samples characterized by Raman spectroscopy, using a Renishaw InVia Raman Microscope equipped with 532-nm excitation laser set, to assess the graphitization of the pyrolyzed PAN samples. Over 100 Raman spectra were acquired and averaged across each type of carbon fibers to evaluate the graphitic quality of the resulting carbons. The Raman spectra were then fitted using Lorentzian curves and analyzed. Optical

confocal microscopy (Keyance, VK-X) and scanning electron microscopy (FEI, Quanta 3D FEG Dual Beam) were employed to observe the morphology of the carbon nanofibers. 4-point probe station (Signatone, S-302-4, with a SP4 probe head) was used to measure the conductivity of the pyrolyzed PAN samples.

High-resolution transmission electron microscopy (HRTEM; FEI, Titan 80-300kV S/TEM) operated at 300 kV was used to visualize and evaluate the microstructure of the pyrolyzed PAN samples. TEM samples were prepared by drop-casting pyrolytic carbon sample, suspended in toluene, onto TEM grids (PELCO CM20 purchased from Ted Pella, Inc.). Fast Fourier Transform (FFT) was applied on the collocated TEM micrographs to further measure the crystallinity and the fringe separation distance of the resulting carbons.

Cyclic voltammetry (CV) was used to characterize the electrochemical behavior of the three distinct types of carbon fiber mats(CFM): pure PAN, PAN-CNT and M-PAN-CNT. CVs of the CFM were first run in a 1 mM potassium ferricyanide (Fischer Scientific) in 2M potassium chloride (Sigma Aldrich) solution using a traditional 3-electrode configuration with a Ag/AgCl (BASi) reference electrode and a 1 cm^2 polished glassy carbon (Structure Probe, Inc) counter electrode. Potassium ferricyanide was chosen as the redox couple to characterize the CFM as it is particularly sensitive to the presence of graphitic edge planes, while remaining relatively insensitive to most other surface modifications[148], [149]. To further distinguish the effects of graphitic edge planes, a subsequent CV is run in a 2 M KCl aqueous solution. The presence of redox peaks in this second CV affirms the presence of ferricyanide ion adsorption along the edge planes[149], [150]. To characterize the electrochemical performance of the pyrolyzed PAN electrodes, the heterogeneous electron transfer rate, k^o_{app}, was calculated using the Nicholson method[151],

$$\Psi(\Delta E_{peak}) = (\frac{D_O}{D_R})^{1/2} k^o_{app} (\pi n F v D_O / RT)^{-1/2} \qquad (1)$$

In equation (3), n is the number of electrons transferred, v is the scan rate, F is the Faraday's constant, R is the universal gas constant, and D_O and D_R are oxidation and reduction diffusion coefficients for Ferricyanide redox couple, with values of 7.26 x 10^{-6} cm^2/s and 6.67 x 10^{-6} cm^2/s, respectively[152]. Ψ is a dimensionless function of ΔE_{peak} (distance between the cathodic and anodic current peaks) found for the conditions of a single step, single electron transfer process at the Temperature (T) of 300 K. k^o_{app} is determined by evaluating the ΔE_{peak} at a scan rate of 100 mV/s of each pyrolyzed PAN nanofiber mats.

4.1.3 Results and Discussion

4.1.3.1 Unwinding PAN molecular chains

Electrohydrodyamic forces offer a powerful tool to manipulate the configuration of polymer molecules embedded in electrically charged liquids. A method of choice for applying electrohydrodynamic forces is electrospinning, where an electric filed is used to draw out polymer nanofibers from a reservoir into fabric mats[153].

The underlying mechanism driving the electrospinning process is the interplay between molecular drag forces (F_D) in the electrospun polymer and the external electrostatic forces (F_{ES}), as illustrated in Fig. 4.1A. The electrostatic forces deform the meniscus of the polymer fluid protruding from the capillary, which forms a region called the Taylor cone[66], [67] (Region 2 in Fig. 4.1). When the Taylor cone is formed, the cross-sectional area of the polymer jet reduces from that of the capillary tube to the significantly smaller cross section

of the traveling jet. This change of cross sections brings about transition regions with drastically different flow velocity: a slow region within the polymer meniscus and a fast region within the traveling jet. The high velocity gradient zones developed at these interfaces result in sizable shear stress fields, which unwind the polymer chains in the jet flow[67]. Small-angle neutron scattering (SANS) and fluid mechanics studies have corroborated this confinement effect, and found a correlation between the gyration radius of the polymer, radius of the electrospun nanofiber, and the alignment of the polymer chains[154]–[156].

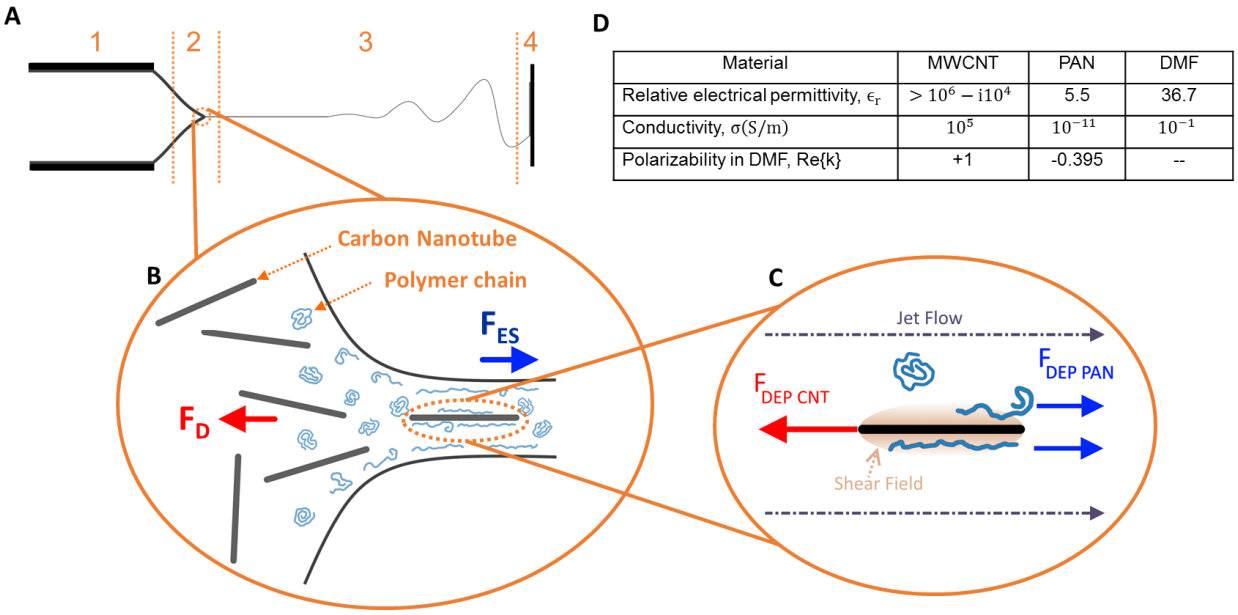

Material	MWCNT	PAN	DMF
Relative electrical permittivity, ϵ_r	$> 10^6 - i10^4$	5.5	36.7
Conductivity, $\sigma(S/m)$	10^5	10^{-11}	10^{-1}
Polarizability in DMF, Re{k}	+1	-0.395	--

Figure 4.1. Unwinding polymer chains during PAN-CNT electrospinning process. **(A)** Different regions in the electrospinning process: 1. conducting capillary tube, 2. Taylor cone, 3. traveling jet, and 4. receiving plate. **(B)** F_{ES} is the external electrostatic force pulling the polymer jet to the receiving plate and F_D is the molecular drag force resisting the F_{ES}. **(C)** $F_{DEP\ CNT}$ is the dielectrophoretic force acting on the carbon nanotubes and $F_{DEP\ PAN}$ is the dielectrophoretic force acting on the polymer chains. (**D)** Dielectrophoretic constants for multiwalled carbon nanotubes (MWCNT), polyacrylonitrile (PAN) and dimethylformamide (DMF). Reproduced with permission from [10].

The addition of MWCNTs into the polymer flow introduces dielectrophoresis phenomenon into the process. Here, the dielectrophoretic force (F_{DEP}) stems from the difference in the electrodynamic properties of the MWCNTs, polymer (PAN) and solvent medium (DMF) in the presence of a strong non-uniform electric field (Table in Fig. 4.1). The direction of the F_{DEP} is determined by the dimensionless Clausius-Mossotti factor (k) which depends on the complex permittivities of the particle ($\epsilon^* = \epsilon - \frac{\sigma}{i\omega}$), and the medium (ϵ_m^*)[157], [158]*:*

$$F_{DEP} \propto \varepsilon_m^* \,\mathrm{Re}\{k\}\nabla E^2 \qquad (2)$$

where,

$$k = \frac{\varepsilon_p^* - \varepsilon_m^*}{\varepsilon_p^* + 2\varepsilon_m^*} \qquad (3)$$

By substituting the permittivity values in Fig. 1, the k factor is determined to be positive for MWCNTs and negative for PAN molecular chains. Consequently, the F_{DEP} will drag the CNTs against the jet flow, while it pushes the polymer chains along the jet's flow direction. The interaction of these opposing forces generates additional shear force zones at the surfaces of the MWCNT that further align the polymer chains.

4.1.3.2 Formation of Stabilized PAN fibers

A critical stabilization phase is usually carried out prior to pyrolysis by heat treatment of the polyacrylonitrile under ambient air pressure (Fig. 4.2)[159]–[162]. In the course of stabilization, PAN molecular chains gain structural stability by cross-linking with the neighboring chains, thus forming conjugated ladder-like structures. The resulting

structural stability enables PAN to withstand the extreme heat treatment of the subsequent pyrolysis step[95], [159].

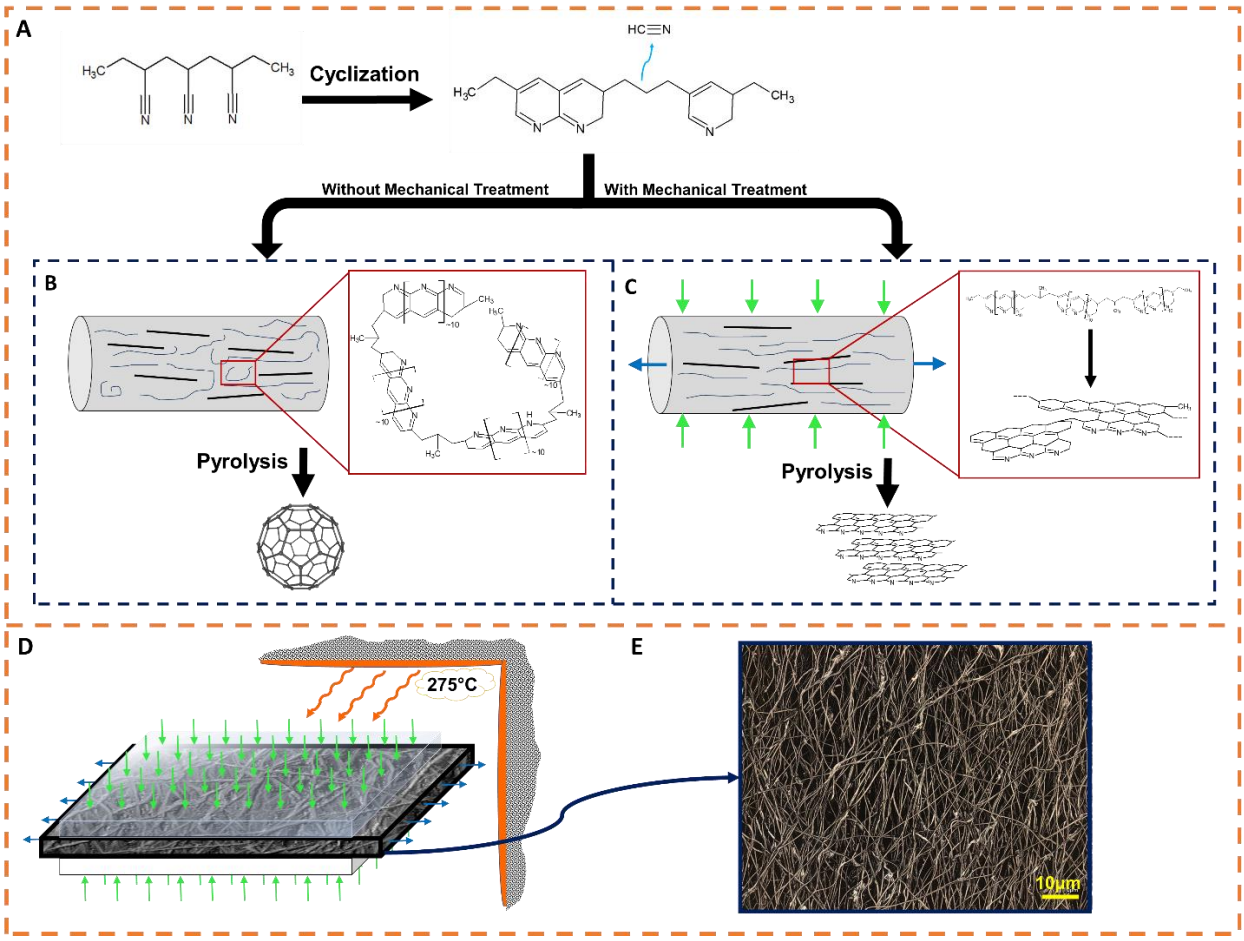

Figure 4.2. The influence of stabilization process on the microstructure of the pyrolyzed PAN fibers. **(A)** Non-ideal cyclization of PAN, which typically occurs in standard stabilization steps[95]. **(B)** Pyrolysis of as-electrospun PAN-CNT fibers (without mechanical treatment) results in amorphous carbon, and at higher temperatures in fullerenic microstructures. **(C)** Mechanical treatment of PAN-CNT fibers during the stabilization preserves the molecular alignment, which results in graphitic microstructures after pyrolysis. **(D)** Mechanical treatment of PAN fibers during the stabilization process. The electrospun PAN mat undergoes principal compressive strain and lateral tensile strain while being stabilized at 275 ^{0}C. **(E)** Confocal microscope image of the pyrolyzed PAN fibers. Reproduced with permission from [10].

During the stabilization of PAN, the polymer backbone chains tend to lose nitrogen groups in the cyclization process, resulting in sp^3 hybridized carbon bonds (Fig. 4.2A)[95], [159]. This leads to the formation of penta- and hepta-carbon rings, which due to their curved structures will yield amorphous carbon or fullerenes during the pyrolysis. Thermodynamic stability of fullerene structures inhibits the polymer from graphitizing into carbon planes even at extremely high temperatures. In other words, the foundation of the polymer microstructures is cast during the preceding synthesis and stabilization phases. Once the curved sp^3 carbon structures form in the stabilization process, the polymer chains are set up to form fullerenes. Accordingly, high-temperature pyrolysis cannot force the underlying carbon foundation to form planar sp^2 carbon planes, rendering the polymer "non-graphitizing".

Considering the impact of the stabilization phase on the orientation of the PAN molecular chains, one expects that the physical parameters of stabilization would influence the graphitization of the polymer precursors substantially. The gains of polymer chain alignment from electrospinning might well be undone by the thermal stresses induced during stabilization, an insight that seems to have been overlooked. Accordingly, during the stabilization process one should aim at providing conditions that preserve or further align the PAN precursor chains, which are already oriented by the shear fields in the electrospinning process. To implement this alignment process, one can apply mechanical forces to maintain/enhance the orientation of the PAN precursor chains during stabilization (Fig. 4.2B).

This approach simply boils down to the question of "how to mechanically suppress the formation of curved surfaces in the polymer microstructure during the stabilization

process". It is thus anticipated that applying surface compression and/or mechanical stretching to a stabilizing polymer mat will translate into the alignment of precursor chains at a molecular-level.

Following the outlined hypothesis, we performed mechanical treatment of the polymer fibers by subjecting the PAN mats to approximately 200 kPa compressive stress while they are being stabilized at 275 ^{0}C in an oven. By performing the stabilization process under such mechanical treatment, the carbon chains are maintained partially aligned and kept from curving during this formative step. This in turn reduces the extent of fullerene formation and sets up the stabilized polymer to form more graphitic carbon planes. We also investigated the influence of applying tensile mechanical stress to the stabilizing polymers. Interestingly, changing the axial stress from compressive to tensile affects the microstructure of final carbon fibers. We discuss this effect in our upcoming report.

Subsequently, we pyrolyzed pure PAN, CNT infused PAN (PAN-CNT) and mechanically-treated PAN-CNT (M-PAN-CNT) samples at 1000 ^{0}C. The resulting carbons' microstructure and properties were then characterized to investigate the effects of polymer chain alignment on the degree of graphitization.

4.1.3.3 Raman Spectroscopy and Conductivity Characterization

Over 100 Raman spectra were collected and averaged across each type of carbon fibers to characterize the microstructure of the resulting carbons. Lorentzian curves were then fitted to the D and G peaks of the representative Raman spectra for each type of synthesis (Fig. 4.3A-C). The heights, shapes, positions, and areas of Raman peaks can provide valuable information about electronic and structural properties of the final carbons[163],

[164]. Typically, the G peak, centered at 1560–1600 cm^{-1}, is the first order Raman mode activated by in-plane vibration of carbon atoms in sp^2-hybridized graphene planes. Thus, the height and sharpness of the G peak reveals the presence of a crystalline graphitic phase in carbon materials. The D peak at 1300–1400 cm^{-1} is the defect-originated Raman band that indicates the degree of disorder in graphitic sp^2 structures. Accordingly, the ratio of D band to G band peak heights, (I_D) /(I_G), has been consistently used to probe the graphitic quality of carbon materials microstructure[163]–[167].

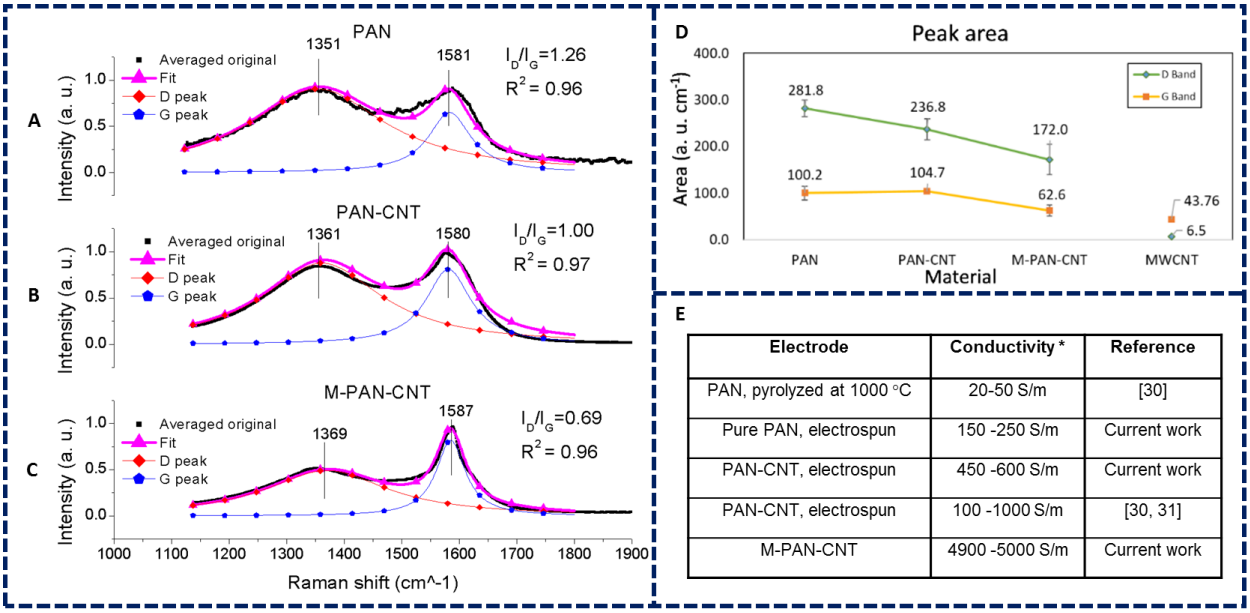

Electrode	Conductivity *	Reference
PAN, pyrolyzed at 1000 °C	20-50 S/m	[30]
Pure PAN, electrospun	150 -250 S/m	Current work
PAN-CNT, electrospun	450 -600 S/m	Current work
PAN-CNT, electrospun	100 -1000 S/m	[30, 31]
M-PAN-CNT	4900 -5000 S/m	Current work

Figure 4.3. Raman spectroscopy and conductivity measurements of the PAN-based pyrolytic carbons. Raman Spectra and Lorentzian fits for pyrolyzed electrospun mats made of **(A)** PAN, **(B)** PAN-CNT and **(C)** M-PAN-CNT. Averages of over 100 collections are used to represent each type of mat. ($\lambda_{excitation}$ = 532 nm) **(D)** Variation of D peak and G peak areas as functions of synthesis procedure. **(E)** Conductivity of the PAN-based pyrolytic carbon samples measured using 4-point probe method. Included for comparison, conductivities of pyrolyzed PAN carbons from other studies[168], [169]. Reproduced with permission from [10]

A quick examination of Lorentzian fitted Raman spectra indicates that with the application of CNTs during electrospinning, I_D decrease with respect to I_G and both peaks exhibit

approximately the same intensities. The implmentation of mechanical treatment reduces the relative intensity of disorder associated band by more than 30%. Accordingly, (I_D) /(I_G) ratio decreases from 1.26 in pure PAN fibers to 0.69 for mechanically treated PAN-CNT (M-PAN-CNT) fibers, revealing a remarkable increase in the graphitic structure of the resulting carbons (Fig. 4.3A-C).

The evolution in G and D peak areas, from PAN control samples to M-PAN-CNT fibers, supports the same upward trend of graphitization in the carbon fibers (Fig. 4.3D). Typically, broader Raman peaks with larger areas are correlated with a higher level of disorder and defects in the graphitic materials. The aquired Raman peak areas verify that mechanical treatment has markedly reduced the areas of D and G peaks, and thus resulted in lower level of disorder in the sp^2 network. Interstingly, the transistion from PAN-CNT to M-PAN-CNT exhibits larger drop in the peak areas, compared to that of pure PAN to PAN-CNT. Moreover, the appreciable impact of mechanical treatment on the Raman peak areas demonstrates that the improvement of the Raman quality index (I_D) /(I_G) is not due to the contribution of nanotubes, as mere addition of CNTs does not change the area of the G peak.

The electrical conductivities of the PAN-based carbons, measured by 4-point probe method, confirms the increasing trend of graphitization, from pyrolyzed pure PAN, to PAN-CNT, to M-PAN-CNT, with conductivity values of ~200 S/m, 550 S/m, and 5,000 S/m, respectively (Fig. 4.3E). The correlation between the microstructures and bulk properties reveals the uniformity of graphitization across the PAN mats, and demonstrates that the enhanced graphitic microstructures translate into improved bulk characteristics in the carbon fabrics.

4.1.3.4 High Resolution Transmission Electron Microscopy

High-Resolution Transmission Electron Microscopy (HRTEM) allows for detailed study of carbon microstructure in the pyrolyzed PAN specimen. Visual examination of lattice fringes in TEM micrographs illustrates the evolution of carbon microstructures developed by the outlined processes. In Fig. 4.4A we show the HRTEM micrograph of the carbon fibers produced by pyrolysis of pure PAN at 1000 ^{0}C. Consistent with the agreed-upon notion that PAN is "non-graphitizing", this micrograph reveals that the structure of the pyrolyzed PAN is highly disordered and randomly curled. The fast Fourier transform (FFT) of the micrograph yields symmetric rings, further evidencing the amorphous nature of the carbon fiber.

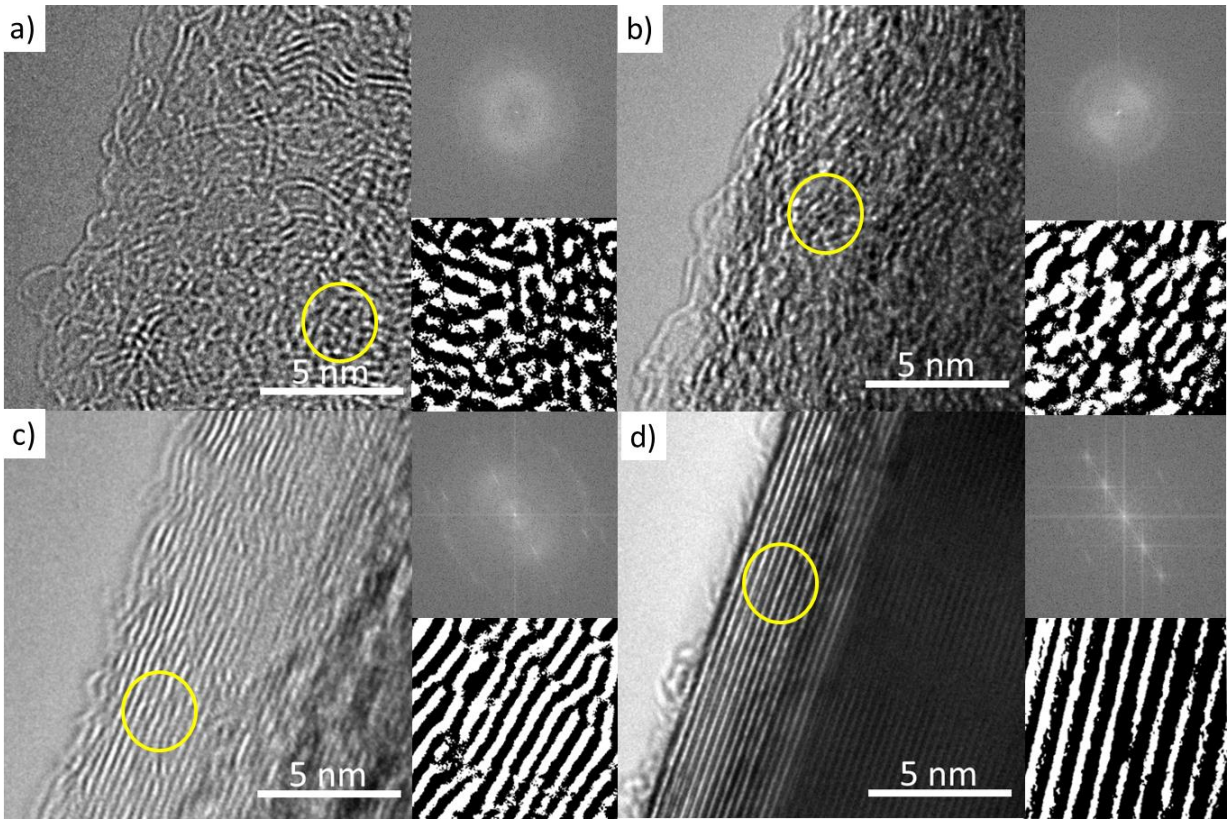

Figure 4.4. HRTEM micrographs of the PAN-based pyrolytic carbons. TEM micrographs of pyrolyzed **(A)** pure PAN, (**B)** PAN-CNT, **(C)** M-PAN-CNT and **(D)** CNT nanofibers. The inset on upper right corner of each micrograph shows the associated Fast Fourier Transform of the carbon microstructures. The lower inset shows the smaller portion of the micrograph (yellow circle) enlarged and processed for enhanced visualization of the lattice fringes. Reproduced with permission from [10].

The micrographs in Fig. 4.4B and 4.4C reveal the effects of electrohydrodynamic molecular alignment and mechanical treatment on the structure of the resulting pyrolyzed PAN. As can be seen in Fig. 4.4C, the structure of M-PAN-CNT specimen exhibits aligned carbon lattice fringes, which are stacked rather tightly together. Here, the carbon lamellae are generally well-oriented with slight undulations, demonstrating imperfect graphene planes. The fast Fourier transform of this image supports our observation by revealing directionally aligned carbon planes with a fringe separation-distance of 3.6 Å.

By comparison, the nanostructure of PAN-CNT appears to be in transition from an amorphous to a more graphitic material (Fig. 4.4B). Here, the carbon fringes are somewhat visible but more fragmented and randomly oriented. Moreover, there is a noticeable increase in the tortuosity of the carbon planes, compared to M-PAN-CNT. In some domains, the fiber nanostructure resembles that of pure pyrolyzed PAN of Fig. 4.4A. This is particularly meaningful considering that randomly oriented curves in atomic planes impede the development of tightly-packed parallel carbon planes; instead, they lead to the formation of fullerenic structures[6], [91], [170]. Such “wrinkles” are mechanically “flattened” during the stabilization processes of M-PAN-CNT (Fig. 4.4C). A higher level of tortuosity also increases the fringe separation, as manifested by the 3.8 Å interlayer spacing acquired from the FFT of the TEM image (Fig. 4B inset). Figure 4.4D, TEM

micrograph of pure MWCNT, is included for comparison with the pyrolyzed PAN samples. Expectedly, the CNT exhibits well-aligned, tightly stacked graphitic lattice planes with a minimal to zero tortuosity and fringe separation of 3.4 Å.

Image processing allowed us to reduce the noise from the HRTEM images of the M-PAN-CNT fibers and enhance the visualization of resulting carbon microstructures (Fig. 4.5). As clear from Fig. 4.5, the fragmented yet well-aligned lattice fringes in the M-PAN-CNT suggest a high ratio of edge planes to basal planes in the carbon structure. Such a high concentration of edge plane atoms makes for a highly reactive carbon surface, which holds great promise for enhanced electrochemical performance.

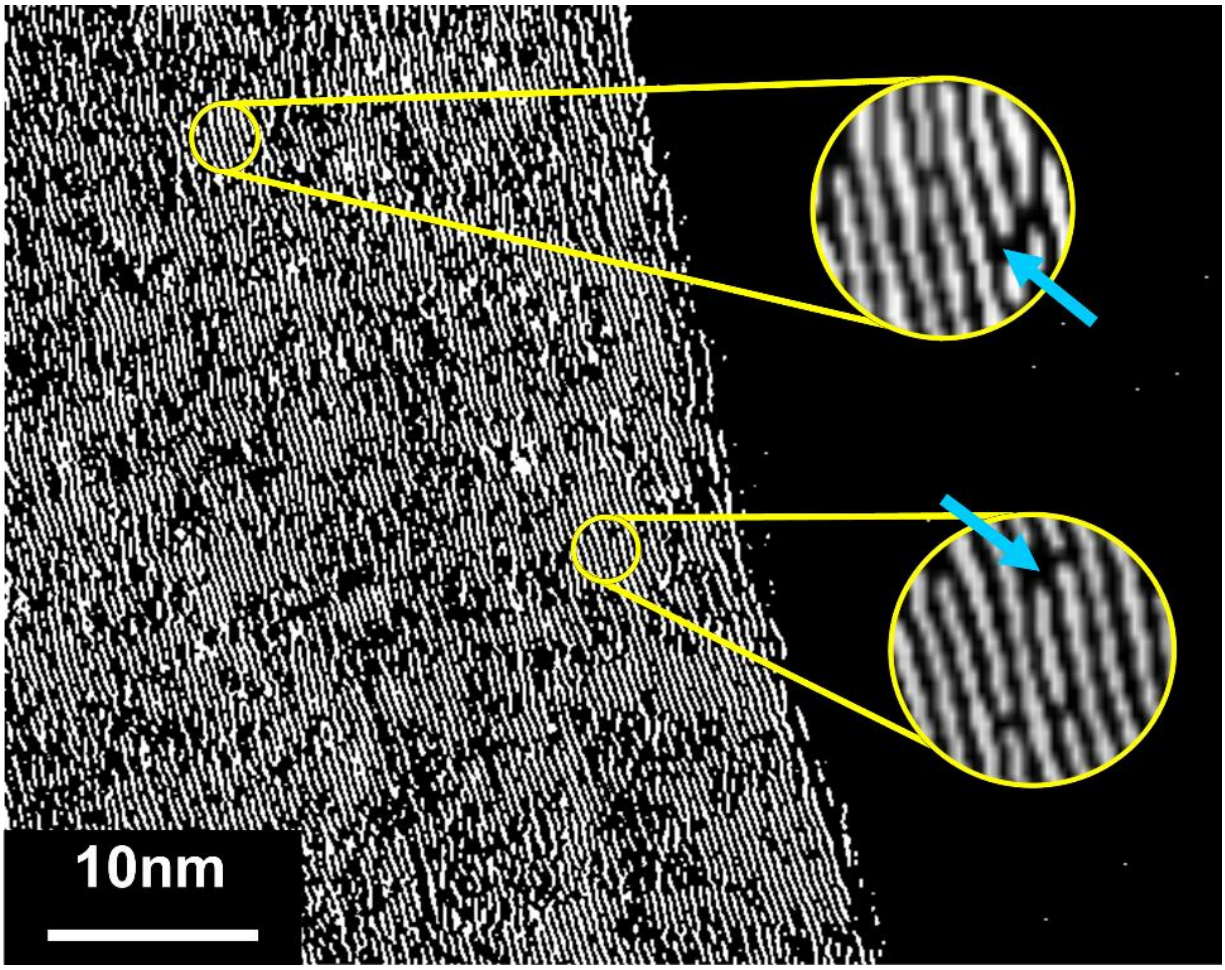

Figure 4.5. A processed image of the TEM micrograph of the M-PAN-CNT. Blue arrows point to the characteristic carbon edge planes. Reproduced with permission from [10].

Electrochemistry is fundamentally a bulk property of the carbon and therefore for the graphitization of PAN-based carbon nanofibers to have an impact on the electrochemical performance it must be uniformly distributed throughout the nanofiber. Therefore, averaged Raman spectra and Raman maps were determined based on 100 spectra collected across 5 μm X 5 μm area of the CNF mats (Figure 4.6). From the map we see that the I_D/I_G has comparable uniformity as untreated PAN-based CNF mats, indicating a promising change in overall microstructure that should have an impact on its electrochemistry. However, graphitization alone is not enough to ensure greater electrochemical

performance. Rather it's the quantity of "defects" within the graphitization that drives electron transfer processes governing all electrochemical applications. Thus, it is anticipated that the much more disorderly graphitic microstructure of the M-PAN-CNT compared to that of the embedded MWCNT, as seen in the HRTEM of Figure 2d, will have greater degree of electrochemical performance.

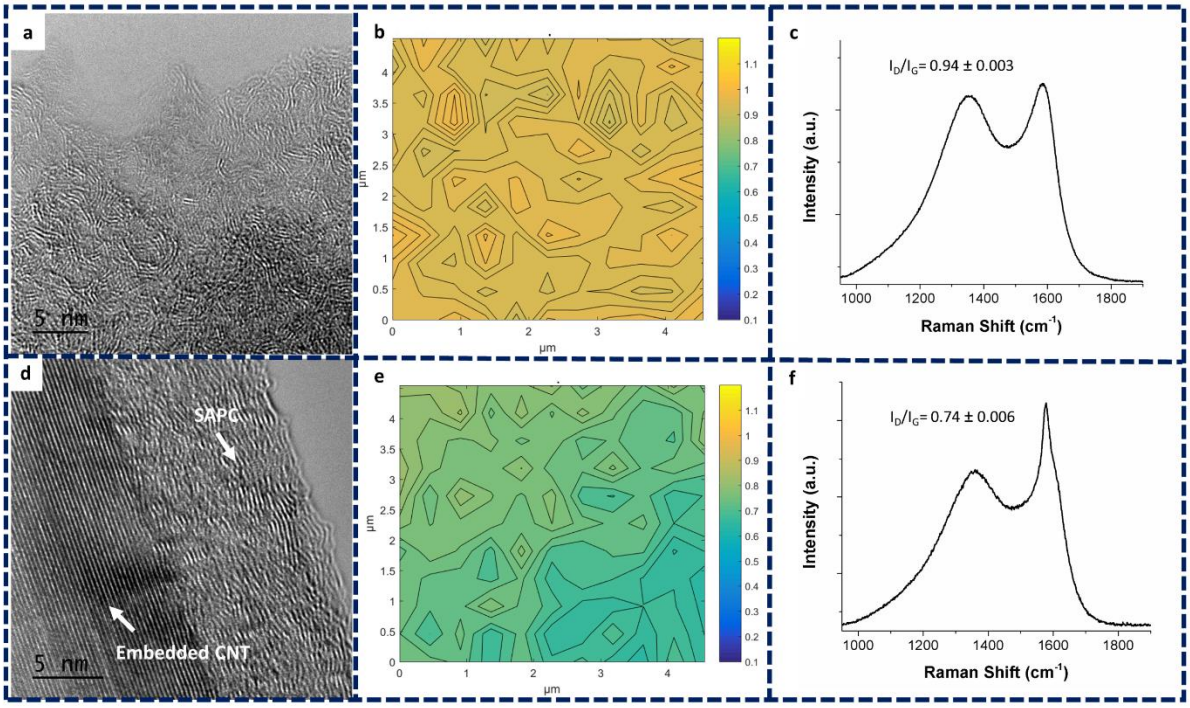

Figure 4.6. Material Characterization. a&d) High Resolution Transmission Electron Microscopy (HRTEM) of the carbon microstructure, b&e) topographical map of Raman spectrum's I_D/I_G ratio and c&f) average Raman Spectrum of the map (>100 points) of a-c) CNF and d-f) SAPC electrodes. Reproduced with permission from Materials Today, submitted for publication. Unpublished work under CC BY 4.0.

3.1.3.5 Electrochemical Performance

Cyclic voltammetry of Ferri/ferrocyanide ($[Fe(CN)_6]^{3-/4-}$) has been used as a standard method for evaluating the quality of a carbon electrode's electrochemical

performance[148], [149], [171]. The voltammograms in Fig. 4.7A-C allow us to evaluate the electrode's kinetics by estimating their heterogeneous electron transfer rate constant (k^o_{app}) via the Nicholson method[151],

$$\Psi(\Delta E_{peak}) = \left(\frac{D_O}{D_R}\right)^{1/2} k^o_{app} \left(\pi n F v D_O / RT\right)^{-1/2} \qquad (1)$$

Here, n is the number of electrons transferred, v is the scan rate, F is the Faraday's constant, R is the universal gas constant, and D_O and D_R are oxidation and reduction diffusion coefficients for $[Fe(CN)_6]^{3-/4-}$, with values of 7.26 x 10^{-6} cm^2/s and 6.67 x 10^{-6} cm^2/s, respectively[152]. Ψ is a dimensionless function of ΔE_{peak} (distance between the cathodic and anodic current peaks) found for the conditions of a single step, single electron transfer process at the Temperature (T) of 300 ^{0}K. It is important to note that the observed linear dependency between the current density of voltammograms' peaks and the square root of the scan rate for all carbon electrodes (insets of Fig. 4.7) is a characteristic of standard bulk diffusion, for which Nicholson formula is applicable.

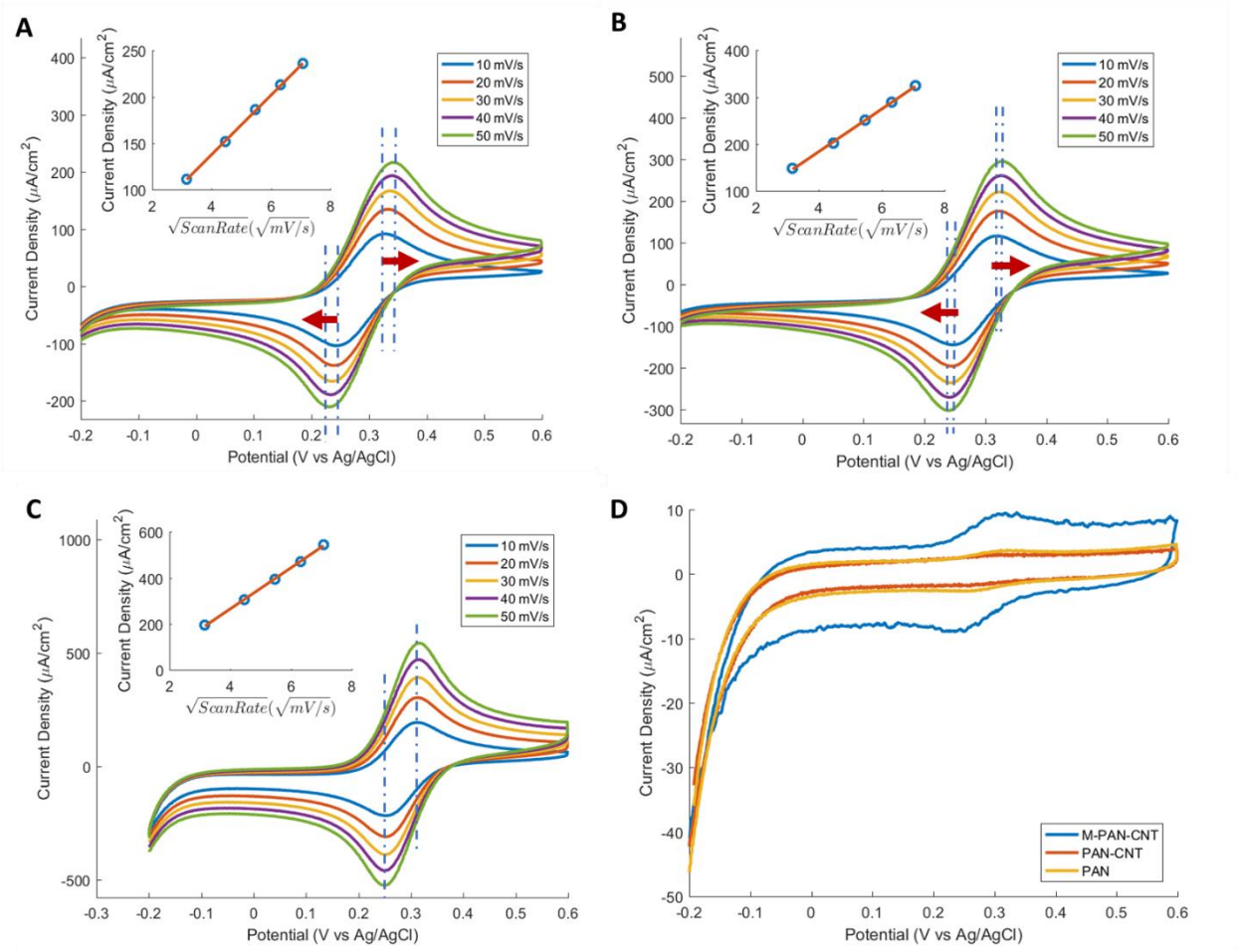

Figure 4.7. Electrochemical performance of the PAN-based pyrolytic carbons. Representative cyclic voltammograms of pyrolyzed **(A)** pure PAN, **(B)** PAN-CNT, and **(C)** M-PAN-CNT electrodes run in 1mM potassium ferricyanide and 2M potassium chloride aqueous solution. **(D)** The representative cyclic voltammograms of pure PAN, PAN-CNT, and M-PAN-CNT run in 2 M potassium chloride aqueous solution tested at 10 mV/s (The voltammograms were collected immediately after the $[Fe(CN)_6]^{3-/4-}$ characterization). All cyclic voltammograms were normalized by the geometric surface area of the pyrolyzed carbon fiber electrodes. Reproduced with permission from [10].

The mechanical treatment of PAN electrodes has significantly boosted their kinetics, increasing the k^o_{app} eleven-fold from 0.0029 cm/s in PAN to 0.0312 cm/s in M-PAN-CNT (Table 4.1). The enhanced kinetics is also evident from the lack of peak shift with

increasing scan rate, indicative of quasi-reversible electrochemical reaction[148]. The improvement in electrochemical performance stems from the abundance of graphitic edge planes in the carbon fiber microstructure[149], [150], [171]. Indeed, Compton *et al*. were able to model the electrochemical performance of carbon electrodes solely based on the quantity of graphitic edge domains on their surface[150], [172], [173]. Consistent with these studies, the k^o_{app} of M-PAN-CNT electrodes demonstrates an order-of-magnitude enhancement over pure CNT-based electrodes[174], [175], and approaches that of graphene and reduced graphene oxide electrodes[176], [177].

All carbon fiber electrodes were tested in a 2 M KCl solution immediately after the electrochemical characterization in $K_3[Fe(CN)_6]$ batch (Fig. 4.7D). Compared to pure PAN and PAN-CNT electrodes, the peaks in M-PAN-CNT's voltammograms are more pronounced, pointing to stronger adsorption of $[Fe(CN)_6]^{3-/4-}$ onto the surface of the mechanically treated fibers. This observation is consistent with previous studies, which reported that the adsorption of $[Fe(CN)_6]^{3-/4-}$ onto carbon occur predominantly on functionalized graphitic edge sites[171], [172], [178]. It is noteworthy that the observed enhanced kinetics and adsorption capacity in M-PAN-CNT are achieved without any additional activation process. The inherent aptitude of M-PAN-CNT for functionalization is particularly attractive because it addresses a main challenge in utilizing graphitic carbons for various electrochemical devices[1], [2], [8], [57], [179].

Table 4.1. Electrochemical, Raman and electrical characteristics of PAN based pyrolytic carbons compared to other carbon materials. Reproduced with permission from [10]

Carbon Type	Pyrolyzed Pure PAN	Pyrolyzed PAN-CNT	Pyrolyzed M-PAN-CNT	Glassy Carbon	MWCNT	Graphene
k^o_{app} (cm/s)	0.0029[a]	0.0053[a]	0.0312[a]	0.0013 – 0.029, 0.5[b]	$8.34x10^{-5}$ – 0.00367	$1.4x10^{-3}$ – 0.15 [e]
I_D/I_G	1.26	1.00	0.69	1.30 – 0.49	.2 -.1	3-.1 [e]
σ (S/m)	150-250	450-600	4900-5000	20,000-25,0000 [f]	$3x10^5$ [c] - $2x10^7$ [d]	200 – $2x10^5$ [e]
Reference	Current Work	Current Work	Current Work	[178], [180], [181]	[174]	[20], [176], [182]

a. Average k^o_{app} measured using Nicholson method at 100 mV/s

b. Laser/fracturing activated glassy carbon.

c. Carbon nanotube fibers and thin films.

d. Single carbon nanotube.

e. Depends on number of defects

f. Pyrolyzed at 3000 ^{0}C

4.2. Stress-Activated Pyrolytic Carbon's Electrochemistry

4.2.1 Introduction

The uniquely disorderly, graphitic microstructure and the high as-fabricated electrochemical kinetics prompted me to further investigate the electrochemical characteristic of the M-PAN_CNT, which became to be known as Stress-Activated Pyrolytic Carbon (SAPC). Thus, further material studies and more comprehensive electrochemical characterization were performed to analyze the microstructure and electrocatalytic aptitude of the synthesized carbon. First, the carbon's electrocatalytic performance is probed by its responses to three different redox systems with structural, surface and adsorption sensitives that can shed light on different aspects of the carbon

electrochemistry. The results demonstrate an overall enhancement in degree and stability of the graphitized carbon's electrocatalysis, with a particularly high propensity for surface and adsorption sensitive elements in comparison to traditional pyrolyzed carbons. The results prompted further investigation into selective simultaneous detection of several adsorptive species (dopamine, uric acid and ascorbic acid), which further demonstrated the great potential for the graphitized carbon for biosensing applications. Spectroscopy (XPS), reveal a pyrolytic carbon microstructure that it plentiful in both graphitic edges and nitrogen heteroatoms.

4.2.2 Result and Discussion

4.2.2.1 Material Characterization

Carbon's electrocatalytic behavior varies considerably based on its synthesis method, microstructure and chemistry. A number of studies suggest graphitic edge planes and heterogeneous atoms within carbon lattice are the main factors enhancing its catalysis, due to the higher density of electronic states at these "defects"[9], [21], [39], [172]. Accordingly, a significant amount of carbon research has focused on tuning these features to improve carbon's electrochemical performance[41], [172], [178]. As previously discussed, we demonstrate how inducing molecular alignment in organic precursors can influence their microstructure and carbonization upon pyrolysis[10]. Based on this method, a PAN-based pyrolytic carbon is synthesized with a uniformly graphitized structure, which is inherently abundant in edge planes. Additionally, the proposed synthesis method applies a low-temperature pyrolysis, which potentially allows for retention of nitrogen heteroatoms from PAN molecules in the resulting carbon structure. We expect that the unique structure of

this pyrolytic carbon and the propensity of the synthesis method for incorporation of nitrogen heteroatoms, to yield a boosted electrocatalytic response of final carbon electrodes.

To investigate the presence of heterogeneous atoms and the composition of the PAN-based carbons we employed X-ray photoelectron spectroscopy (XPS). The XPS data reveals the presence of nitrogen and oxygen in the pyrolytic carbons, with a composition breakdown of 94.5±0.1 at.% carbon, 4.4±0.5 at.% nitrogen and 1±0.3 at.% oxygen (Figure 4.8). Lorentzian curve fitting is applied to deconvolute the nitrogen peak, N 1s. The results point to a rather unique distribution of nitrogen groups, comprising of 19.2% pyridinic, 57.0 % graphitic, and negligible amount of pyrrolic nitrogen atoms in the synthesized carbon fibers[45], [46], [183]. The remaining nitrogen atoms are in the form of oxidized nitrogen groups that are represented the peaks located at 405 and 402.6 eV in Figure 4.8. The detected nitrogen heteroatoms most likely originate from the nitrogen-rich PAN precursors that endured the low-temperature pyrolysis. The breakdown of the nitrogen heteroatoms in the synthesized carbon is particularly of interest for its electrochemical performance, as pyridinic and graphitic nitrogen's higher density of electronic states enhances carbon's electrochemical transfer kinetics. It is important to note that the nitrogen heteroatoms are inherent in the as-pyrolyzed carbons, and no additional post-synthesis process, such as doping, has been

applied to introduce nitrogen into the resulting microstructure.

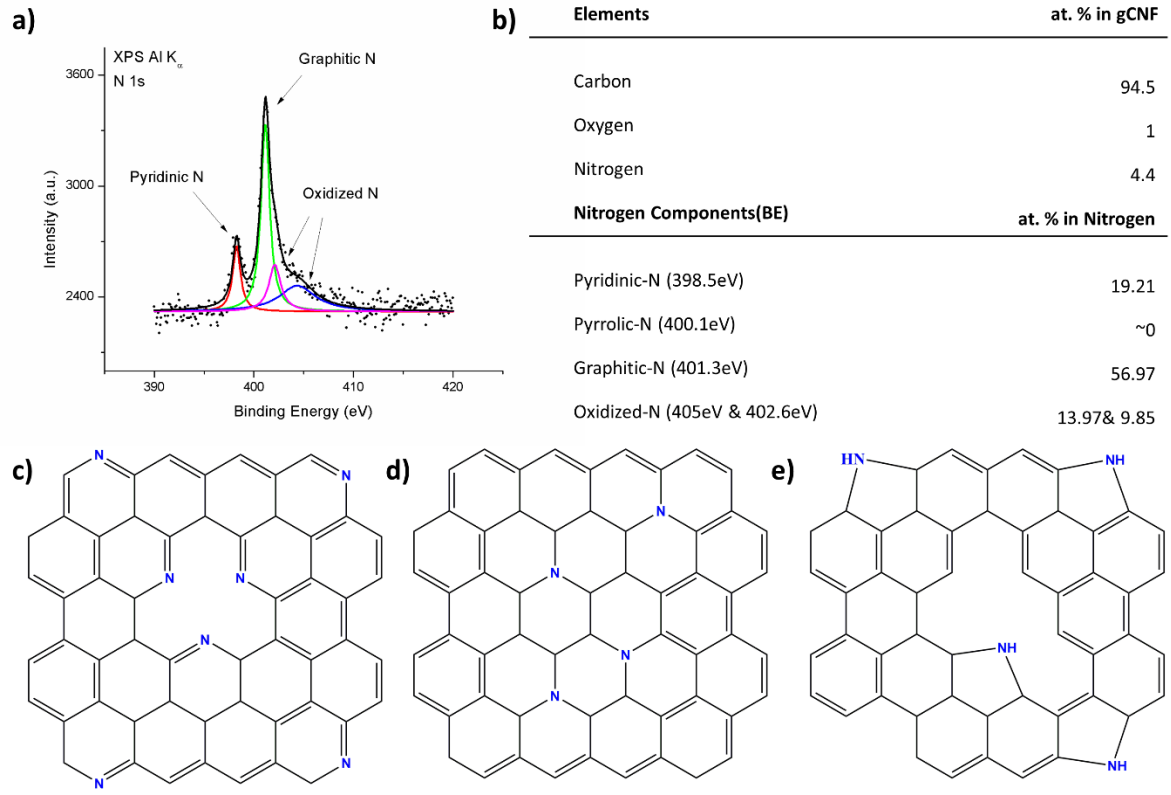

Figure 4.8. X-ray Photoelectron Spectroscopy (XPS). XPS spectrum of a) of the N 1s peak of SAPC. b) Table of elemental composition of the SAPC as determined by analysis of XPS spectrum. Chemical Structure of c) pyridinic, d) graphitic and e) pyrrolic nitrogen within the carbon lattice. Reproduced in part with permission from Advance Functional Materials submitted for publication. Unpublished work © 2018 John Wiley and Sons.

4.2.2.2 Electrochemical Kinetics

A defining parameter in electrode materials is the density of electronic states (DOS), which directly influences their kinetics and heterogeneous electron transfer rate. For carbon electrodes, the shape and size of the DOS distribution depend primarily on the carbon structure. The presence of disorders in graphitic lattice introduces defect states with

energies that enhances the electronic DOS near the Fermi level[9], [21]. This increases the electronic states in the carbon electrode with energy levels that overlap with the E° of the redox system, thus enhancing the electron transfer rates**.** Therefore, the electrochemical performance of disordered graphitic structures, with edge planes and dangling bonds, is superior to that of HOPG with ideal crystalline structure[21]. For electrodes tested in outer-sphere electron transfer systems (surface sensitive analytes), the electronic DOS is affected by the disorders in the underlying microstructure of the carbon. In the case of inner sphere redox systems (surface insensitive analytes), the electronic DOS and electron transfer rate depend on the carbon surface defects and their interactions with the redox systems.

Accordingly, to probe our carbon material from different aspects, we study its electrochemical responses in three different redox systems, namely, potassium hexachloroiridate $[IrCl_6]^{2-/3-}$ (surface insensitive), potassium ferricyanide $[Fe(CN)_6]^{3-/4-}$ (surface sensitive), and dopamine (adsorption sensitive)[9], [21], [178]. To this end, cyclic voltammetry tests were performed with PAN-based CNF, SAPC, and polished Glassy Carbon (included for comparison) in the above-mentioned probes. The collected cyclic voltammograms allow us to investigate the electrochemical reversibility of electrode materials by determining the heterogeneous electron transfer rate (k^o_{app}), the ratio between the reduction and oxidation current peaks (I_{red}/I_{ox}) and the linearity between the current peaks and the square root of the scan rate. Table 4.2 summarizes the results.

First, the collected voltammograms in Figure 4.9 demonstrate a linear relation between the square root of the scan rate and the peak current density. The linear correlation indicates that the nanofiber electrodes exhibit behavior akin to standard planar electrodes rather

than more complex electrochemistry, which validates k^o_{app} values determined by Nicholson Method[21], [151]. To study our carbon electrodes systematically, we first analyze their electrochemical behavior within each aqueous redox probe, and then by comparing their varying performances across the different probes.

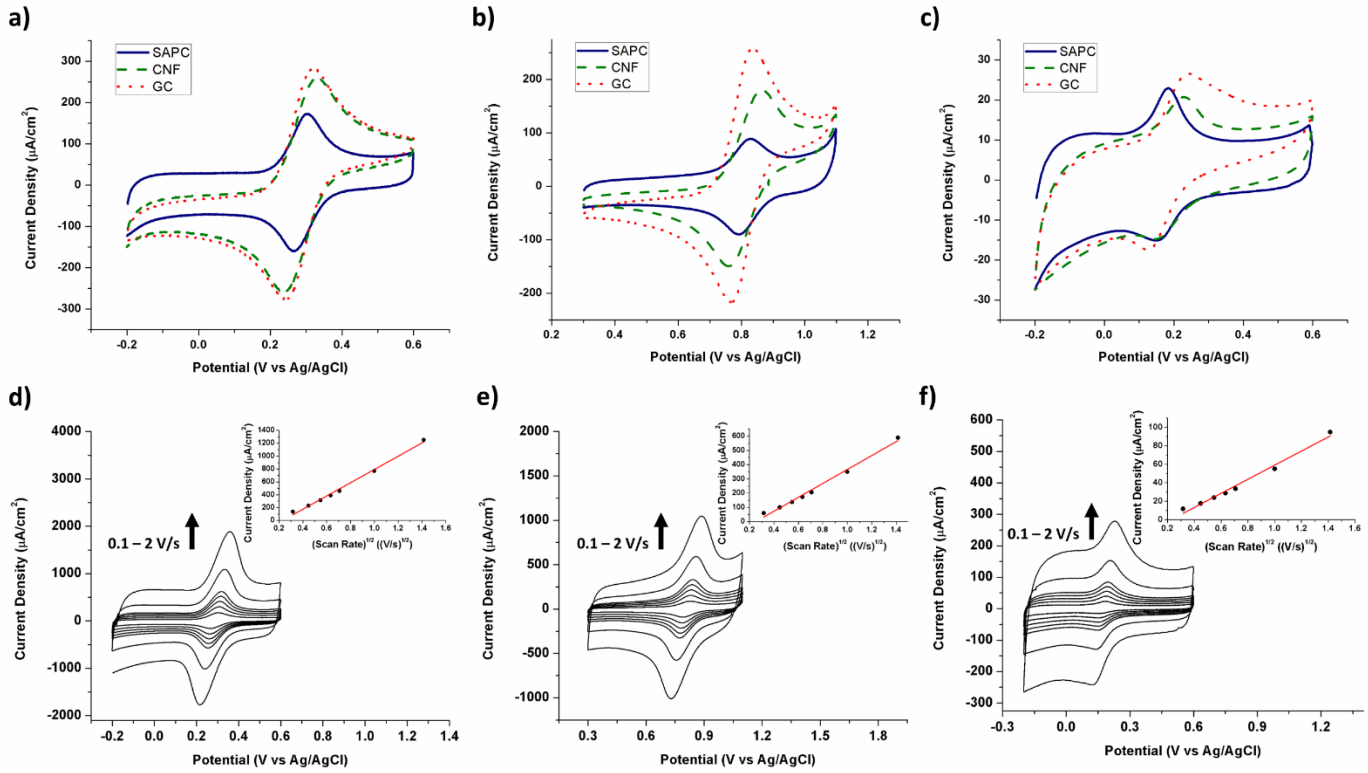

Figure 4.9. Electrochemical Kinetics of SAPC. Comparison of the representative cyclic voltammograms of SAPC, CNF and GC's electrochemical response to aqueous solution of a) 2 M KCl and 1 mM of $K_3Fe(CN)_6$, b) 2 M KCl and 1 mM of K_3IrCl_6 and c) pH 7.4, 1 mM PBS at and 0.1 mM of Dopamine at a scan rate of 100 mV/s. SAPC's cyclic voltammograms of its electrochemical response to varying scan rates in an aqueous solution of a) 2 M KCl and 1 mM of $K_3Fe(CN)_6$, b) 2 M KCl and 1 mM of K_3IrCl_6 and c) pH 7.4, 1 mM PBS at and 0.1 mM of Dopamine. Reproduced in part with permission from Advance Functional Materials submitted for publication. Unpublished work © 2018 John Wiley and Sons.

As mentioned earlier, potassium hexachloroiridate is an outer-sphere redox probe. Due to the tunneling of electrons through the electrode surface, the response of carbon electrodes

in $[IrCl_6]^{2-/3-}$ is more susceptible to the carbon underlying microstructure and is insensitive to the defects and interactions occurring on the surface[9], [21]. Thus, potassium hexachloroiridate is a suitable electrochemical probe for structural analysis of our pyrolytic carbon fibers. As seen in Table 4.2, the electrochemical reversibility of PAN-based carbons has increased 8 folds from CNF 0.00586 cm/s to SAPC 0.0461 cm/s, suggesting a remarkable increase in density of electronic states stemming from the graphitization of carbon microstructure of SAPC. This deduction is consistent with other structural characterization of our carbon material as shown in Figure 4.9, and reported in our previous study on graphitizing pan-based carbon with stress-induced routes[10]. The k^o_{app} value for SAPC is also approximately two times higher than that of alumina-polished glassy carbon, a standard activated carbon electrode used here as a ground for comparison. The enhanced kinetics of SAPC in $[IrCl_6]^{2-/3-}$ underlines the high proportion of disorders in form of edge sites within the structure of the SAPC electrodes. These structural disorders induce energy states between the conduction and valence bands, thus amplifying the electronic DOS near the E° of the $[IrCl_6]^{2-/3-}$analyte. The overlap between the energy levels of the carbon electrode and those of acceptor/donor in the redox system result in a boosted electron transfer rate. As expected, mechanical roughening of the electrode surface (as in the case of alumina polished GC) will not improve its kinetics more than that of SAPC in a surface insensitive analyte.

Next, we investigate surface defects and interactions of the pyrolytic carbons by evaluating the response of the carbon electrodes in $[Fe(CN)_6]^{3-/4-}$, a benchmark inner-sphere redox probe with high kinetic sensitivity to the state of electrodes surface[9], [21], [184]. A major factor in electrochemical response of carbon electrodes in $[Fe(CN)_6]^{3-/4-}$ is the density of

electronic states caused by the surface defects and functional groups. Here, the electron transport kinetics shows a similar upward trend by registering a 13-folds increase, from CNF electrodes 0.00795 cm/s to SAPC 0.114 cm/s. The higher enhancement in k^o_{app} values determined in $[Fe(CN)_6]^{3-/4-}$ (compared to that of potassium hexachloroiridate) points to the effectiveness of our carbon synthesis method in boosting the surface features, i.e., edge planes and other electroactive sites. Indeed, HRTEM characterization of the carbon electrodes surfaces corroborate this electrochemical deduction[10].

Table 4.2. Electrochemical Kinetics Values of the Carbon Electrodes. Reproduced in part with permission from Advance Functional Materials submitted for publication. Unpublished work © 2018 John Wiley and Sons.

Carbon Type	CNF	SAPC	Alumina-Polished Glassy Carbon
$[Fe(CN)_6]^{3-/4-}$			
k^o_{app} (cm/s)	0.00795	0.114	0.0135
I_{red}/I_{ox}	0.99	0.99	0.99
$[IrCl_6]^{2-/3-}$			
k^o_{app} (cm/s)	0.00586	0.0461	0.0232
I_{red}/I_{ox}	0.99	0.99	0.99
Dopamine			
k^o_{app} (cm/s)	0.00861	0.0418	0.00146
I_{red}/I_{ox}	0.751	0.92	0.705
Reference	Current Work	Current Work	Current Work

Moreover, our stress-induced fabrication method yields electrodes that are one order magnitude better that alumina-polished glassy carbons. While surface roughening of glassy carbon (GC) electrodes yields surface defects with high electronic DOS, these energy states and the kinetics improvement caused by them are often transient. The poor stability of polished GC electrodes is attributed to the coarse nature of mechanical abrasion, which

produces defects that are electrochemically unstable and can be rapidly passivated. On the other hand, the surface states of SAPC electrodes are forged at the elevated temperatures of pyrolysis and are therefore more resistant to passivation. We will discuss this phenomenon further in the stability analysis of the electrodes.

Perhaps, one of the most interesting redox systems is dopamine, whose layered and complex electrochemical interaction with carbon electrodes can reveal a variety of insights about them. Dopamine is an inner-sphere analyte that is principally sensitive to adsorption and state of electrodes surface[9], [185], and mostly indifferent to their inner structure. In this context, a dramatic shift in behavior is observed between the 3 carbons; for the first time the k^o_{app} of the amorphous CNF is higher than that of the better structured GC. Furthermore, the electrochemical kinetics in dopamine marks the largest enhancement from polished glassy carbon 0.00146 cm/s to SAPC electrodes 0.0418 cm/s, among the different analytes. Additionally, a dramatic change between the I_{red}/I_{ox} from a 0.751 and 0.705 of CNF and GC, respectively, to that of SAPC, exhibiting a near unity I_{red}/I_{ox} of 0.92. Both intriguing observations point to adsorption mechanisms that are active on the surface PAN-based electrodes (CNF, and SAPC).

The electrooxidized form of Dopamine (Dopamine o-quinone) can undergo a chemical oxidation, which reduces its concentration by converting it to an electrochemically inert agent[186], [187]. An observed drop in the reduction peak of the dopamine response reflects this phenomenon. It is believed that the adsorption due to π-π stacking and interaction between hydrogen groups at edge planes serve to promote its electrochemical reduction over chemical oxidation[45], [188], [189]. For carbon electrodes, adsorption

sites are mostly located near graphitic edge planes where heteroatoms are present and provide the necessary dipole interaction for adsorption to occur. Indeed, the results of the XPS elemental composition analysis reveal a significant quantity of nitrogen heteroatoms on the surface of the PAN-based electrodes. Though XPS data shows the presence of oxygen groups as well, prior studies have shown oxygen concentrations below 7% have negligible effect on the kinetics of dopamine electro-oxidation[190]. Therefore, the enhanced kinetics of dopamine oxidation is likely caused by the electrocatalytic performance of the electrodes' nitrogen groups and graphitic edge planes, particularly in the case of SAPC. Overall, enhanced kinetics displayed by the SAPC is comparable to some of the highest performing carbon electrodes studied to date, including reduced-graphene oxide and laser-activated Glassy Carbon electrodes[9], [19], [191]. Additionally, compared to other nitrogen-doped carbons, SAPC has a rather unique composition of C-N groups, consisting of primarily Graphitic and Pyridinic nitrogen groups at a ratio of 3 to 1. Both these nitrogen groups are highly stable. Therefore, considering the lack of post-pyrolysis activation process, it is anticipated that the remarkable high kinetics of SAPC will also exhibit a high degree of electrochemical stability.

4.2.2.3 Electrochemical Stability

As previously, discussed, pyrolytic carbons often require an additional activation step after their pyrolysis to achieve notable degree of electrocatalytic capacity. These activation step are typically transient in nature and only temporarily boosts the electrochemical performance of the carbons, as in the case of mechanical fracturing of HOPGs and glassy carbons[41], [184]. However, the as-fabricated SAPCs do not require such additional

process, and readily exhibit an enhanced degree of electrochemical performance, as established in the previous sections. It is anticipated that the robust, single-step fabrication process for SAPC's will translate to an intrinsically high electrochemical stability for their electrodes. To evaluate this attribute, cyclic voltammetry was performed with each redox system on SAPC for 300 cycles at 100 mV/s (~1.5 hour per test).

The stability of the electrochemical response over the numerous scans is extracted by decoupling the faradaic oxidation peak current density from the background capacitive current and presented Figure 4.10d-f). Analysis of the results of these prolonged cyclic voltammograms indeed points to stable electrochemical kinetics of as-fabricated SAPC electrodes, particularly in comparison with additionally processed carbon electrodes. As can be seen from Figure 4.10, SAPC electrodes in $[IrCl_6]^{2-/3-}$ and $[Fe(CN)_6]^{3-/4-}$ analytes experience less than one percent drop in current density and maintain their kinetics with only a negligible 2-3 mV increase in ΔE_{peak} over the course experiments. In contrast, carbons with similar kinetics, such as fractured HOPG and glassy carbons electrodes, immediately begin to lose activity from chemisorption of oxygen and other adsorbed impurities, reverting to the level of electrochemical activity in unactivated glassy carbon within hours[41], [184]. For example, both fractured HOPG and Glassy Carbons exhibit drastic ΔE_{peak} increases from ~70 mV to >550 mV in its response to $[Fe(CN)_6]^{3-/4-}$ after a single day of exposure to air. Even for $[IrCl_6]^{2-/3-}$ that is less sensitive to the effects of chemisorption of oxygen to edge planes, ΔE_{peak} will rise more than a 10 mV in Fractured HOPG and Glassy Carbon after a single day of exposure to air.

The response to dopamine exhibits higher degree of variation on day-1 experiments. This increased instability likely stems from the adsorption process, the dominant electron exchange mechanism in dopamine oxidation, exacerbates the kinetic behavior by slowing the transport of the oxidized dopamine away from the electrode, thus blocking the transport of fresh dopamine to adsorption sites. Additionally, this phenomenon would cause a larger initial drop in the current density, as it would take longer for the electron transfer and transport mechanism to reach an equilibrium. However, after soaking the SAPC electrodes in DI water for two days, the stability improves significantly and compares well with the other two analytes ($[IrCl_6]^{2-/3-}$ and $[Fe(CN)_6]^{3-/4-}$) on day-3 experiments.

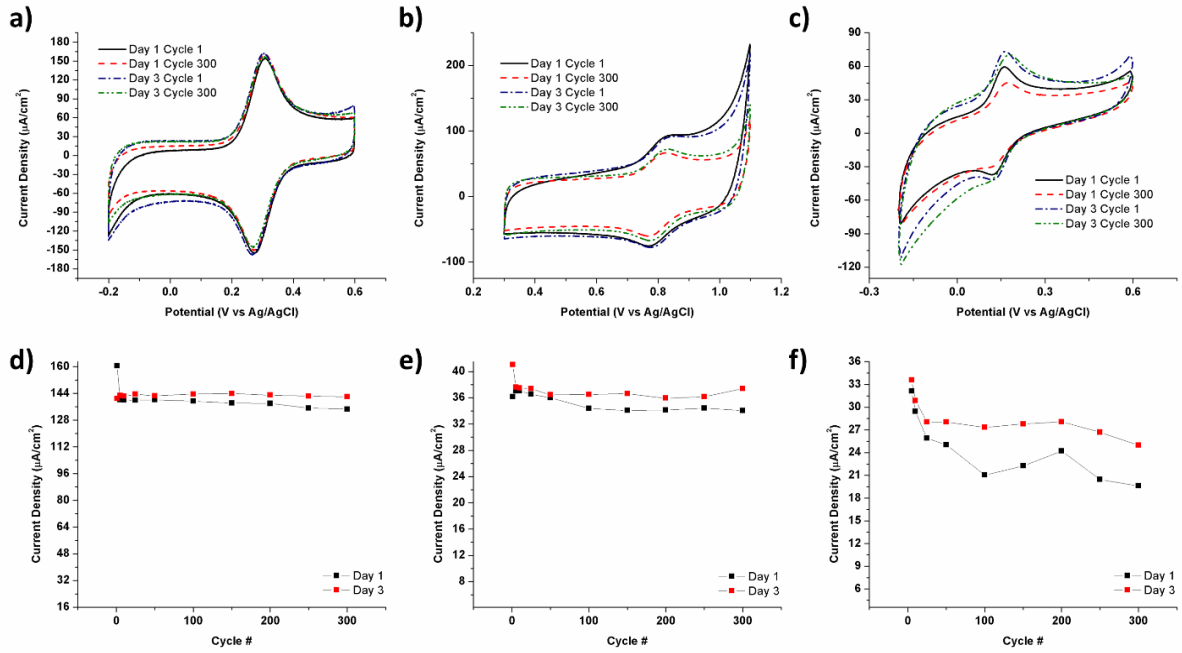

Figure 4.10. Electrochemical Stability of SAPC. Representative cyclic voltammograms of SAPC's electrochemical response to prolong cycles at 100 mV/s in an aqueous solution of a) 2M KCl and 1 mM of $K_3Fe(CN)_6$, b) 2M KCl and 1mM of K_3IrCl_6 and c) pH 7.4, 1mM PBS at and 0.1 mM of Dopamine. The faradaic oxidation peak current density of SAPC response to an aqueous solution of d) 2M KCl and 1 mM of $K_3Fe(CN)_6$, e) 2M KCl and 1mM of K_3IrCl_6 and f) pH 7.4, 1mM PBS at and 0.1 mM of Dopamine. Reproduced in part with

It is important to note that the initial drop in the current density of SAPC electrodes (in all analytes) is an artifact caused by the limited mass transport within the hydrophobic, nanoporous SAPC matrix[192]. Therefore, it is not indicative of lack of stability in the tested electrodes. Soaking the electrode mats in DI water effectively exposes active electrochemical surface of the SAPC matrix, thus realizing its full potential by enhancing the mass transport within the nanoporous matrix. This increased exposure results in an overall rise in the peak current density and a reduction in its fluctuation, as reflected by the day-3 stability test results in Figure 4.10.

From day-3 results, the stability of SAPC's response to dopamine compares favorably with additionally-processed GC (laser, fractured, or polished), as well as more expensive alternatives, such as graphene-based electrodes, such as the case with the graphene nanoflakes reported by Shang et al that saw a 20% drop in current density after 50 scans[193]. Additionally, recovering the electrochemical response with rinsing is not a viable option for graphene-based electrodes as they are prone to structural damage. In comparison, SAPC's electrochemical stability is far more resilient to physical damage and leeching effects. Such robustness is evident from the fact that the high stability of SAPC electrodes does not waver when these electrodes are cut into smaller pieces from a larger mat (a process akin to mechanical fracturing methods for activation in other pyrolytic carbons). This superb electrochemical stability and kinetics exhibited by SAPCs is unique among carbon electrodes and is particularly well suited for various biosensing applications.

5 – Applications

The remarkably high and enduring electrochemical kinetics of the SAPCs pushed for further investigating into its potential electrochemical applications. Due to the similarities in material and electrochemical characteristic of SAPCs to nitrogen-doped graphene, SAPCs electrocatalytic to selective biomarker detection, hydrogen peroxide reduction and oxygen reduction were investigated. Finally, SAPCs capacity as a biofuel cell cathode or Laccase immobilization was investigated.

5.1 Dopamine Biosensor

The unique electrocatalytic behavior of SAPC allows for an efficient and simultaneous detection of dopamine (DA), ascorbic acid (AA), and uric acid (UA) without the need for additional activation or post-processing of the pyrolytic carbon. Dopamine is a neurotransmitter that modulates critical functions of the central nervous system and its concentration can directly affect the health of the host. Ascorbic acid and uric acid are another common chemical found throughout the human body whose electrochemical response overlaps with that of dopamine for most forms of carbon-based electrodes. The results demonstrate that SAPC has a sensitivity and limit of detection that compares favorably with expensive graphene and CNT based sensors. The capability of SAPC for detecting biomarkers accentuates its potential for biomedical sensing applications. Additionally, the SAPC exhibits an enhanced mechanical stability compared to its graphene-

based counterparts, which are fragile and suffers from with leeching effects. The SAPCS are monolithic carbon structures with nitrogen groups embedded throughout its microstructure, and therefore, suffers minimal loss in electrochemical performance from either leeching or physical damage to the structure.

The electrocatalysis aptitude of SAPC in adsorption-sensitive analytes makes this carbon electrode an appealing candidate for biosensing applications. A particular area of interest in biochemical sensing is selective electrochemical detection of ascorbic acid (AA), Uric Acid (UA) and dopamine (DA). AA, UA and DA are important biomarkers whose concentration within the body can be directly attributed to health status of the host[45], [189], [193], [194]. Shifts in the concentration levels of AA, UA and DA have been directly linked to neurodegenerative diseases, like Parkinson's and Alzheimer's disease, and has prompted concerted efforts for developing facile, sensitive, and selective biosensors for their detection.

Carbon electrodes have traditionally had subpar performance for selective detection of AA, UA, and DA, due to overlapping electrochemical responses for these analytes[193], [194]. As illustrated in the cyclic voltammograms in Figure 5.1, the degree of separation between the peak potentials of AA, UA and DA indeed correlates directly with the heterogenous electron rate, determined in the earlier sections. For carbons lacking an adequate quantity of strong adsorption sites (such as glassy carbon) the sluggish electron transfer kinetics results in a drastic positive shift in oxidation peak potential in all three species, causing their response to overlap and become indiscernible. As the surface of carbon is modified to enhance the adsorption and electron transfer kinetics of AA, DA and UA, the individual

oxidation peaks of each species undergo a negative potential shift, which differentiate them from each other, as seen in the electrocatalytic oxidation voltammograms of SAPC electrodes.

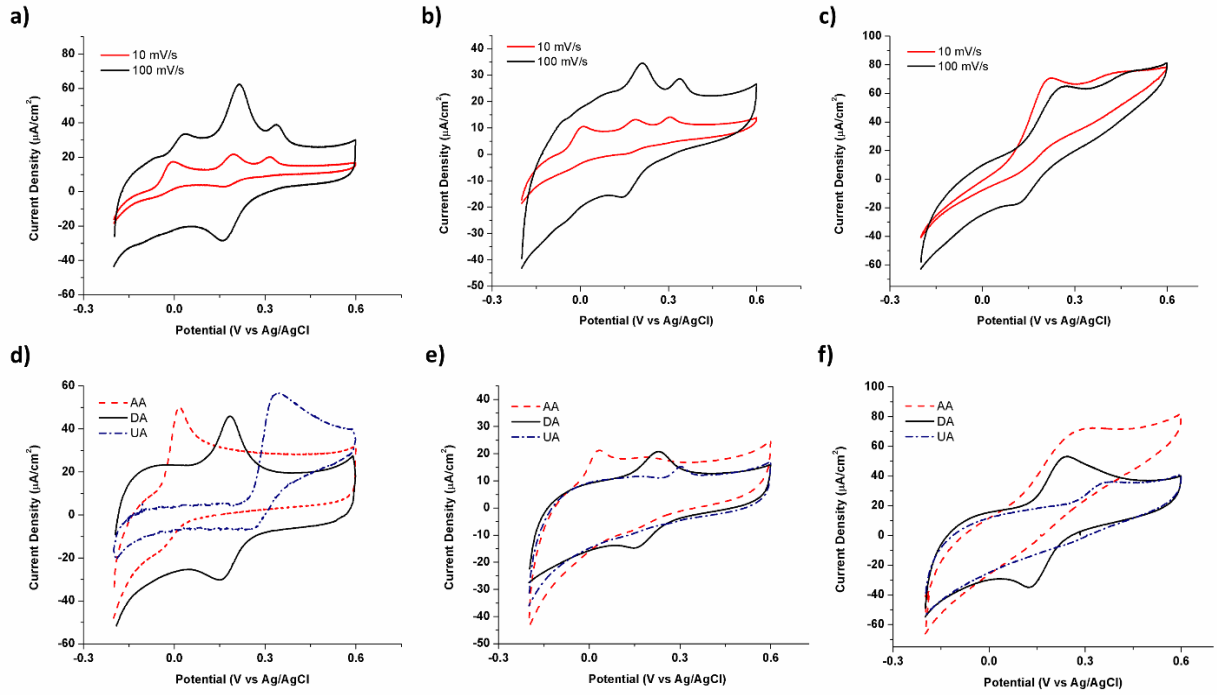

Figure 5.1. Electrocatalytic oxidation of Dopamine, Ascorbic Acid and Uric Acid. Cyclic Voltammograms of a) SAPC, b) CNF and c) GC electrodes' response to in 1 mM Ascorbic Acid, 0.1 mM Uric Acid and 0.1mM Dopamine in a pH 7.4 PBS buffer. Combined Cyclic Voltammograms of a) SAPC, b) CNF and c) GC electrodes' responses to separate solutions of in 1 mM Ascorbic Acid in pH 7.4 PBS buffer, 0.1 mM Uric Acid in pH 7.4 PBS buffer and 0.1mM Dopamine in a pH 7.4 PBS buffer. Reproduced in part with permission from Advance Functional Materials submitted for publication. Unpublished work © 2018 John Wiley and Sons.

Comparing SAPC and CNF simultaneous detection response, SAPC's superior kinetics is evident from the appearance of AA peak at the higher scan rates (100 mV/s) that is absent in CNF's simultaneous response, but present in its individual response. The differing AA

response with CNF between the individual response and simultaneous response stems from the sluggish kinetics caused by competition between the three electroactive species interfering with each other's electron transfer and ion transport process at the at CNF's adsorption active sites. This effect becomes noticeably worse at higher concentrations of UA (1 mM), DA(1 mM) and AA(10 mM), as the charge transfer and transport begins to saturate with the increasing concentration, and CNFs' simultaneous response begins to resemble that of glassy carbon. Here SAPC's superior electrocatalysis for adsorption sensitive species is further demonstrated as its voltammogram continues to exhibit three distinct peaks at these higher concentrations. For both concentrations, SAPCs simultaneous response exhibit AA, DA, and UA peaks to be located between -2.76 mV and 37 mV, 198 mV and 214 mV, and 316 mV and 337 mV, respectively. This separation in electrochemical response results in an average difference of 189 mV between the AA and DA peaks (ΔE_{DA-AA}), and 120 mV between the DA and UA peaks (ΔE_{UA-DA}). Furthermore, these peak separations are comparable to those seen in prior studies on graphene-based electrodes[45], [189], [193]. The distinguishable electrochemical response and lack of interference between the electroactive species makes SAPC a superior platform for selective detection of these biomarkers.

Differential pulse voltammetry (DPV) is a highly sensitive voltammetric sweep technique that decouple the background capacitive current from the faradaic response[195]. Application of this technique allows us to investigate SAPC's capability to simultaneously measure the concentration of AA, UA, and DA via analysis of their oxidation peak current. Here, DPV was performed in a 1 mM pH 7.4 PBS buffer in a potential range between -0.2 and 0.6 V vs Ag/AgCl. Each test began with a PBS solution containing 50 μM AA, 5 μM DA

and 5 μM AA and then the concentration of the target analyte is incrementally increased while the remaining two analytes' concentrations are kept constant.

Figure 5.2 demonstrate the results of DPV test. The correlation between the current density and the bioanalytes' concentration is extracted from their respective peak current density in DPV, as shown in the calibration curves (insets of Figure 5.2). The linear correlation between the peak current density and the concentration of the analytes allows us to determine the sensitivity of the SAPC from the slope of the curve. Accordingly, SAPC electrode displays sensitivities of 0.189 μA cm^{-2} μM^{-1}, 1.51μA cm^{-2} μM^{-1}, and 5.21 μA cm^{-2} μM^{-1} for detecting AA, UA, and DA, respectively. The limit of detection (LOD) can therefore be estimated with the following equation[196],

$$\boldsymbol{LOD = \frac{3\sigma}{S}} \qquad (1)$$

where, σ is the standard deviation of the current signal in a blank solution, S is the sensitivity and a signal to noise of 3 (S/N) is used. As summarized in Table in Figure 5.2d, the calculated sensitivity and limit of detection are comparable to the highest values reported to date for graphene-based electrodes[45], [189], [193]. It is also important to note that the peak current density of each electroactive species is not influenced by the addition of the other two species. For the calibration curve of DA, two separate linear regions are observed, both with relatively high linearity, which likely stems from a saturation effect. However, the high linearity of the region, particularly for the lower concentrations, allows us to determine the sensitivity and estimate the LOD from the lower concentration region. Overall, the similarities among the AA, DA, and UA electrochemical response of SAPC, graphene nanoflakes[193], and nitrogen-doped graphene[45], [188],

[189] suggest that the high sensitivity and rapid kinetics of SAPC stems from a combination of its abundant edge planes and heteroatoms.

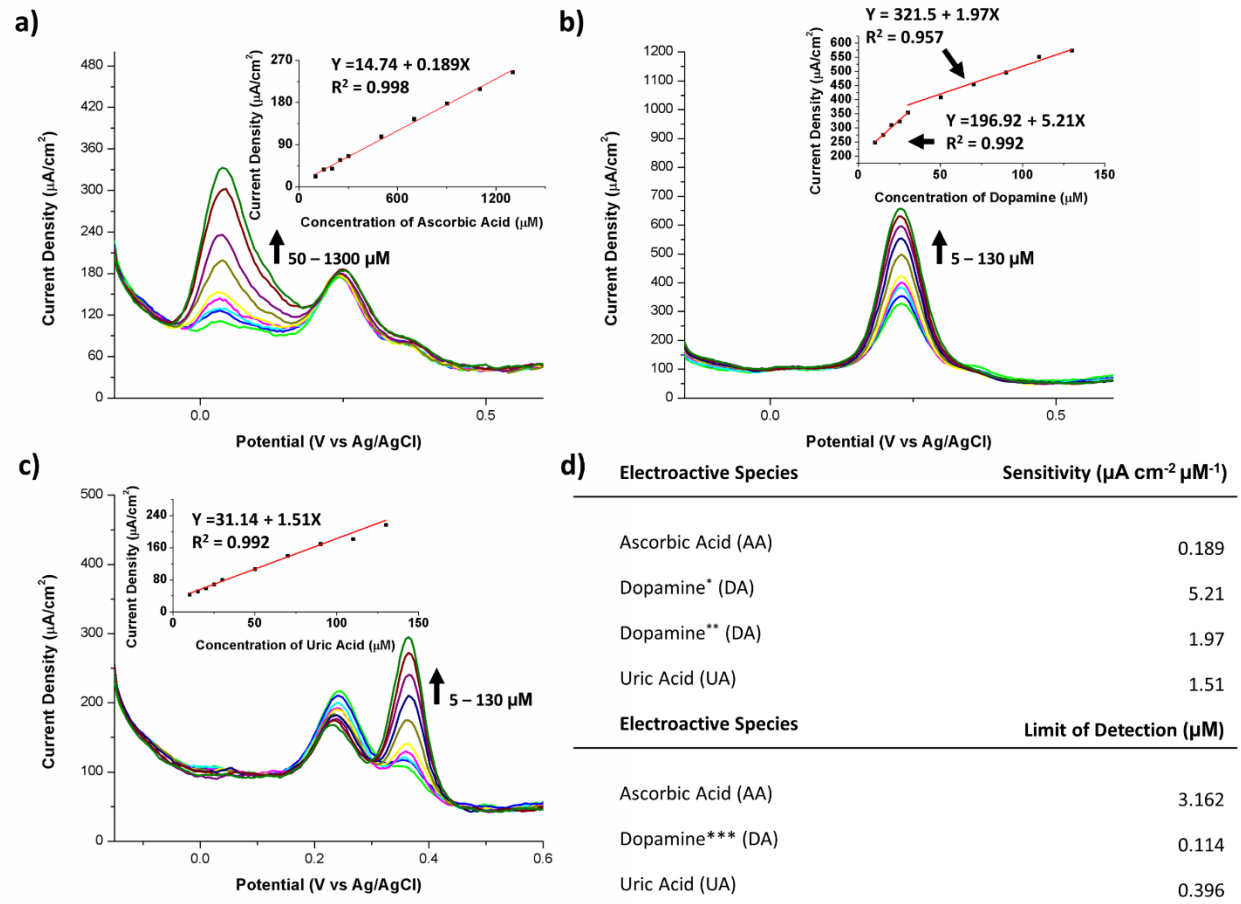

Electroactive Species	Sensitivity (μA cm^{-2} μM^{-1})
Ascorbic Acid (AA)	0.189
Dopamine* (DA)	5.21
Dopamine** (DA)	1.97
Uric Acid (UA)	1.51
Electroactive Species	**Limit of Detection (μM)**
Ascorbic Acid (AA)	3.162
Dopamine*** (DA)	0.114
Uric Acid (UA)	0.396

Figure 5.2. Differential Pulse Voltammetry (DPV). DPV of SAPC response to aqueous pH 7.4 PBS buffer solution containing a) 50-1000 μM AA, 5 μM DA, 5 μM UA, b) 50 μM AA, 5-100 μM DA, 5 μM UA and c) 50 μM AA, 5 μM DA, 5-100 μM UA. Insets show the relationship between peak current density and concentration. D) Table summarizing the sensitivity and limit of detection of SAPC to each analyte. SAPC's dopamine sensitivity measured by *lower linear region and **higher linear region. ***The LOD of Dopamine is determined using the sensitivity of the lower linear region. Reproduced in part with permission from Advance Functional Materials submitted for publication. Unpublished work © 2018 John Wiley and Sons.

5.2 Hydrogen Peroxide Sensor

5.2.1 Introduction

Hydrogen peroxide (H_2O_2) is a common byproduct of many biochemical reactions and is therefore a common analyte used to indirectly detect cellular signaling, aging mechanism and various oxidases such as glucose oxidase, NADPH oxidase, urate oxidase, and lactate oxidase [197]–[202]. Though its major application lies in biosensing, its detection is of high importance in various other fields including textile industry, food industry, and paper manufacturing as well [203]. Consequently, the detection of H_2O_2 is a major field of research for many sensing related applications.

Various techniques have been employed to achieve sensing of H_2O_2 such as fluorescence, colorimetric, and electrochemical methods [197]–[199]. Among these, electrochemical detection, in general, has the reputation of having high sensitivity, selectivity and affordability. However, early experiments of H_2O_2 sensing used noble metals such as platinum and gold as catalytic surface for attaining high sensitivity, making the electrochemical detection of H_2O_2 an expensive option [204]–[206]. This has eventually led to the use of various carbon allotropes such as pure graphene, carbon nanotubes, and graphite for this purpose, which not only circumvents the use of expensive noble metals but also allows for a non-enzymatic method of sensing [207]–[211]. Despite the advantages, the performances of these carbon allotropes are not on par with the existing

sensors with noble elements. The main challenges carbon based H_2O_2 sensors are facing includes slow kinetics and interferences from species such as ascorbic acid and uric acid, prompting investigation in carbon modification[212].

In recent years, studies on the incorporation of heteroatoms into the carbon lattice have gained attention for its ability to enhance the catalysis of the modified carbon. The insertion of heteroatoms into the carbon matrices can tailor the electro-catalytic activity of the material to either enhance or diminish its electrons density. P-type graphene showed enhanced capability to oxidize, whereas the presence of n-type showed improved reduction capacity in various carbon allotropes [200]–[202]. The reducing nature of n-type carbon material, such as NRGC, is found to be highly advantageous in various applications such as fuel cell and biosensors [213]–[216]. In particular, characterization of electrochemistry of nitrogen-rich graphitic carbons (NRGC) have revealed their potential as catalysts for various analytes such as hydrogen peroxide, ascorbic acid, dopamine, and uric acid [217]. Furthermore, NRGC's enhanced electrocatalysis has been demonstrated to allow for the simultaneous detection of these analytes within the same solution [218]. Specifically, NRGC's capacity for H_2O_2 reduction reaction is used as one of the standard measure of its catalytic performance [217].

Various techniques have been reported for the synthesis of nitrogen rich graphite, including doping methods such as chemical vapor deposition (CVD), ball milling, plasma treatment, arc discharge method and thermal treatment [208], [219], [220]. Among which, CVD delivers controllable doping whereas ball milling is known for its simplicity and scalability. However, CVD incurs excessive cost and low yield and ball milling doping is difficult to control and dopes only at edges [208]. Nitrogen plasma treatment introduces as

high as 8 at. % of nitrogen, but often leads to low electrocatalytic activity due to the damage to the carbon lattice incurred by the process [221]. Both arc discharge and thermal treatment methods results only in a very low nitrogen content (~1 at.%)[208]. These doping methods inherently involve multiple processing steps after synthesis of carbon platform. They often include introducing nitrogen into previously synthesized graphitic carbons by damaging the graphitic carbon lattice to introduce holes and defects to allow nitrogen assimilation. The nature of such process is cumbersome and costly to control. Alternatively, there has been a growing interest in single step fabrication of nitrogen rich carbon using electrospun fibers [222]. The main challenge with this approach is that the microstructure of the resulting electrospun carbon fibers are reported to be mainly amorphous and glassy-like carbons, causing low conductivity and reduced sensitivity. Therefore, the similarity between the nitrogen-doped carbon microstructure of nitrogen doped graphitic carbons and that of SAPCs prompted us to investigate its ability for hydrogen peroxide reduction.

5.2.2 Materials and Methods

5.2.2.1 Electrochemical Characterization

A Princeton Applied Research VersaSTAT 4 Potentiostat running VersaStudio 2.48.5 was used for all electrochemical experiments. To prepare the CNF for electrochemical characterization, the mats are cut and then placed onto a cured sheet of Polydimethylsiloxane (PDMS, Sylgard 184 Silicone Elastomer, Dow Corning Corporation). Copper enamel coated wire is bonded onto the CNF electrode at the very edge with conductive carbon paint (Structure Probe, Inc.). Two pieces of cured PDMS are then placed

on the ends of each CNF electrodes and secured in place with uncured PDMS. Careful attention was paid to cover the wire bonded area completely with PDMS. The electrode assemblies are then placed on a hot plate so the PDMS would cure. This PDMS backbone allows the normally fragile CNF electrodes to be more durable while the center section remains free. The geometric area of the CNF electrode is taken from the exposed length (L) and width (W) dimensions and calculated as a flat electrode.

For electrochemical characterization, a blank electrolyte solution of 1X Phosphate-buffered saline (PBS) was used. 1X PBS solutions are made by dissolving Disodium phosphate (Na_2HPO_4, Fisher Chemical), Monopotassium phosphate (KH_2PO_4, Sigma Aldrich), Sodium chloride (NaCl, Fisher Chemical) and Potassium chloride (KCl, Sigma Aldrich) in DI water. The target final concentrations of the 1X PBS was 0.14 M NaCl, 0.0027 M KCl, and 0.010 M PO_4^{3-}. The pH was adjusted to 7.4 with the addition of HCl or NaOH as necessary. The PBS solution was purged of oxygen via bubbling of nitrogen gas prior to the test. During the test, nitrogen gas was left flowing in the headspace above the liquid to help prevent any oxygen from dissolving back into the solution. All electrochemical tests were run while the solution was stirring. A Ag/AgCl reference electrode in saturated 3M KCl solution was used and all potentials are in reference to this electrode. For a counter electrode, a Glassy Carbon electrode was used. Electrochemical Impedance Spectroscopy experiments (EIS) were conducted in the 1X PBS solution to estimate resistivity and capacitance of the electrode [223]. Cyclic Voltammetry tests (CV) were performed 1X PBS with and without presence of 2.5mM Hydrogen Peroxide (H_2O_2 , 30% (w/w), Fisher Chemical). The CV's of H_2O_2 were analyzed and the potential where the maximum current response was noted for the following Chronoamperometric (CA) experiments. The CA were conducted with various

concentrations of H_2O_2 and with common interfering substances. The interfering substances used were Ascorbic Acid (AA, Sigma Aldrich), Glucose (Glu, EMD Millipore) and Uric Acid (UA, Sigma Aldrich).

5.2.3 Results and Discussion

5.2.3.1. Electrochemistry

It has been shown that N-doped graphene sheets have higher electrocatalytic capacity for H_2O_2 reduction as compared to that of pure graphene [217]. This phenomenon is attributed to the presence of pyridinic-N and graphitic-N sites, which assist H_2O_2 reduction by weakening the o-o bond [224].

Additionally, it is expected that graphitic carbon structures with edge planes would demonstrate higher electrocatalytic activity as compared to amorphous carbons. In the previous characterizations, we demonstrated that our SAPCs is inherently rich in graphitic edge planes, and possess high concentrations of pyridinic and graphitic nitrogen atoms. Thus, we anticipate that the synthesized carbons exhibit high propensity for H_2O_2 sensing owing to enhanced electrocatalytic reduction of hydrogen peroxide.

Electrochemical Impedance Spectroscopy (EIS) was performed in a blank solution if 1X PBS (pH 7.4) in order to determine the electrochemically active surface area. From this equivalent circuit the double layer capacitance (C_{dl}) and electrode resistance can be determined [225]. The active surface area (A_{act})of the electrode was calculated using Eq. (1) [223]:

$$A_{act} = \frac{C_{dl} * v}{I_c} \quad (1)$$

Here the C_{dl} was calculated from the constant phase element as the capacitance (μF) EIS plots divided the geometric area (A_g,as calculated in section 2.5). The scan rate is given as v (V/s) and the double layer charging current is I_c. The active surface area is used to normalize the current responses for all electrochemical tests.

Cyclic Voltammetry allows us to investigate the aptitude of SAPCs for H_2O_2 reduction. In Figure 5.3 there are two sets of representative Cyclic Voltammograms (CV) which were run at 50 mV/s in 1X PBS (pH 7.4) with 2.5 mM of H_2O_2 (see Figure 5.3). All voltages are compared against Ag/AgCl. Figure 5.3a shows a comparison of the CVs of SAPC in 1X PBS with and without the presence of 2.5 mM of H_2O_2. With the addition of the H_2O_2 there is a clear increase in the current response, exhibiting a 300 μA increase at -0.5 V vs Ag/AgCl. Furthermore, the treated CNFs exhibit an onset potential of -0.1 V vs Ag/AgCl, comparable to other nitrogen-doped graphene based sensors[226]. It is worth noting that there is a peak seen in plain 1X PBS of SAPC, which could be a result of residual amounts of oxygen being reduced. This response will be further investigated in future works.

The CVs of SAPC is compared with that of the electrodes made from Toray (a type of commercially available graphitic fiber), and untreated pure PAN based CNF (Figure 5.3b). Toray exhibited no noticeable increase in current response after the addition of hydrogen peroxide, indicating little to no electrocatalysis of hydrogen peroxide reduction. Between

pure PAN CNFs and treated PAN CNFs electrodes, treated PAN CNF electrodes demonstrated much larger current response with the addition of hydrogen peroxide.

The reported electrochemical results echo previous studies on NRGC electrocatalysis of hydrogen peroxide. As seen from the XPS data, pure PAN CNF contains small amounts of pyridinic-N and graphitic-N, which contributes to its reduction of hydrogen peroxide. Toray, on the other hand contains no nitrogen groups due to the high temperatures used for its synthesis and therefore has no reduction of hydrogen peroxide. Between treated and untreated CNFs, the much larger current response to hydrogen peroxide could largely be attributed to the higher graphitization seen in the treated CNFs, which is known to contribute to enhance electron transfer efficiencies.

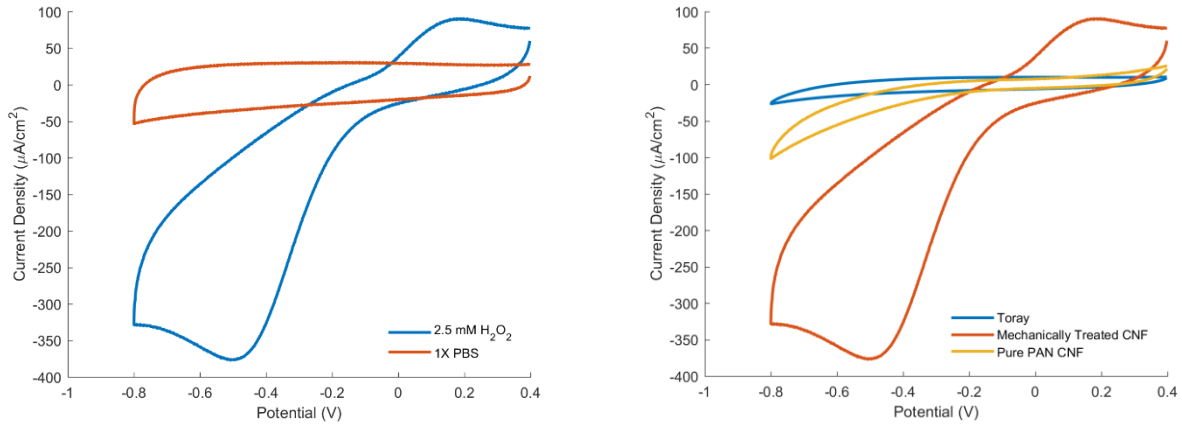

(**a**) (**b**)

Figure 5.3. Cyclic voltammograms at 50 mV/s of (**a**) SAPC run in blank 1X PBS and in the presence of 1X PBS in the presence of 2.5 mM H_2O_2; (**b**). Toray, SAPC, and pure PAN CNF electrodes in 1X PBS in the presence of 2.5 mM H_2O_2. Reproduced with permission from [227].

Chronoamperometry (CA) allows us to determine the sensitivity and limit of detection (LOD) of SAPC as H_2O_2 sensor as seen by the representative CA graph in Figure 5.4a. The CA were performed at -.5V vs Ag/AgCl, the typical potential at which the current density peaks

for the treated PAN electrodes. During the CA, the current was allowed to stabilize before each subsequent additions of hydrogen peroxide and the concentration versus the current density was then extracted from the CA and plotted in Figure 5.4b. Error bars were calculated by examining multiple CA tests and taking the standard deviation of the current response at the various concentrations.

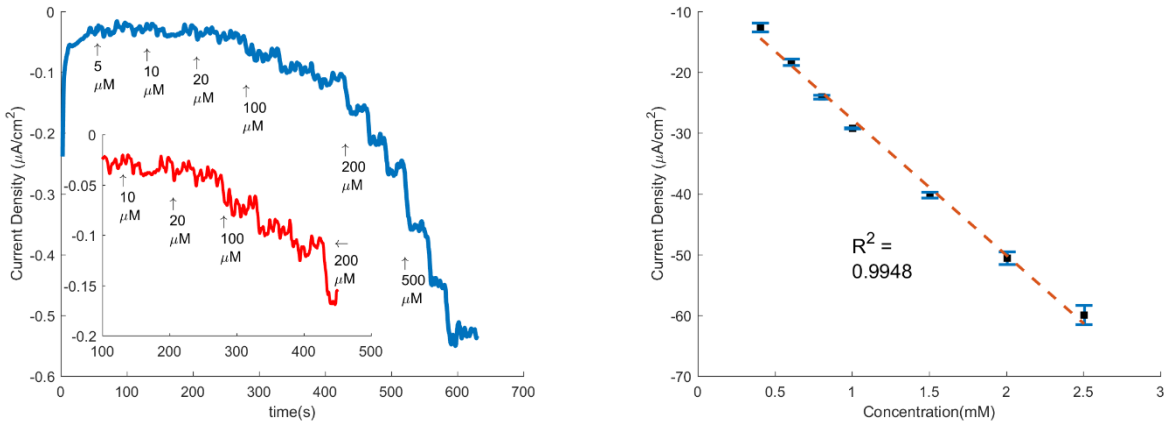

(**a**) (**b**)

Figure 5.4. (**a**) Chronoamperometry of the SAPC electrode running at -0.5V. Each addition concentration is indicated on the graph and was repeated three times after the initial indication prior to the next concentration addition. The inset is a zoomed in portion of the main graph; (**b**) Concentration vs Current Density data from the chronoamperometry fitted with linear regression trend line. Reproduced with permission from [227].

From this Figure 5.4b, the sensitivity was calculated by the linear regression equation:

$$I = -1.98C - 0.471, \quad (2)$$

where C is the concentration in mM and I is the current density in μA cm^{-2}. Here, the slope, and thus sensitivity, is 1.98 μA cm^{-2} mM^{-1} with a correlation coefficient (R^2) of 0.9948. The

LOD was then calculated by Equation 3, where a signal to noise ratio of 3 (S/N=3) was used [228].

$$LOD = \frac{3\sigma}{S}. \quad (3)$$

The standard deviation, σ, was taken from the stable signal of a blank solution and S is the linear regression equation's slope. The LOD was calculated to be 0.781 μM. An average response time of 4.6 seconds was observed after each addition.

In addition, CA was used to investigate the selectivity of the hydrogen peroxide reduction in the presence of other analytes, specifically Ascorbic Acid (AA), Uric Acid (UA), and Glucose (Glu). Figure 5.5 shows the representative graph of CA showing the resulting current responses after additions of 0.15 mM AA, 1mM Glu and 0.5 mM UA and to 1mM H_2O_2 introduced at the indicated times. The results demonstrate that at the working potential of -.5V there was little to no response from any of the tested substances while there was still a noticeable response from additions of H_2O_2, demonstrating the high selectivity of the treated PAN electrodes to hydrogen peroxide reduction.

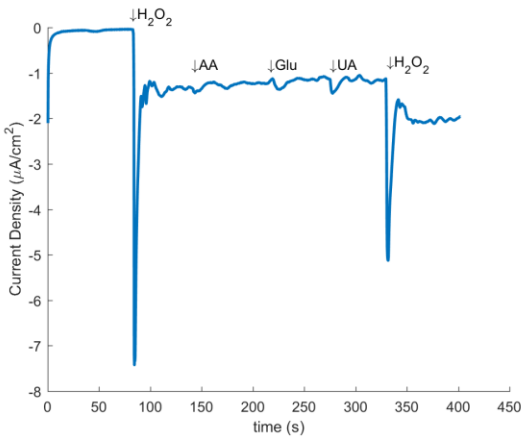

Figure 5.5. Amperometric response of the SAPC at a potential of -0.5V vs Ag/AgCl when sequential additions of 1mM H_2O_2, 0.15 mM AA, 1mM Glu, 0.5 mM UA, and 1 mM H_2O_2 were added. Reproduced with permission from [227].

5.2.4 Conclusion

A number of works have reported application of different forms of carbon allotropes as a basis for H_2O_2 sensing with platforms such as nitrogen doped carbon nanotubes [229], graphene platinum nanocomposites [230] and nitrogen-doped graphene nanoribbons [231]. Such studies have resulted in sensitivities ranging between 0.967 – 154.78 μA mM^{-1} and LODs of 0.15 to 90 μM [231], [232]. In comparison, the SAPC sensors produce a sensitivity of 2.23 μA mM^{-1} when multiplied by active surface area. The acquired sensitivity suggests that, in spite of their facile synthesis route, the electrocatalytic performance of SAPC sensors is comparable to that of the graphene-based sensors with more complex synthesis routes. Furthermore, the SAPC demonstrated high selectivity towards H_2O_2 in the presence of common interfering analytes: Glu, AA and UA. It is important to note that the H_2O_2 sensors were developed from as-pyrolyzed CNFs without additional processing. Refinement of the presented synthesis method will potentially yield additional

enhancement in both the carbon graphitization degree and the quantity of nitrogen groups to further reduce the LOD and augment the sensitivity of the electrodes.

5.3 Oxygen Reduction

Previous nitrogen-doped graphene and carbon nanotubes has demonstrated an enhanced capacity to catalyst the reduction of oxygen[43], [183], [202]. These studies attribute the enhanced electrocatalysis to the presence of pyridinic and graphitic nitrogen groups within the graphene lattice. Therefore, it is also anticipated that SAPC with its nitrogen heteroatoms would exhibit a similar penchant for oxygen reduction. Figure 5.6 show that indeed SAPC exhibit the best electrocatalysis for oxygen reduction among the untreated amorphous PAN-based carbon nanofibers and highly graphitic Toray paper electrodes. It is interesting to note that PAN-based CNF electrodes, which has similar quantity of nitrogen groups as SAPC, demonstrated moderate amount of oxygen reduction. While Toray, with almost no nitrogen groups, display no electrocatalysis of oxygen reduction. The composition of nitrogen is also important here as studies have largely attributed the rate of oxygen reduction to the presence of pyridinic and graphitic nitrogen specifically. Although, there is currently no consensus as to which of these two groups is more efficient for oxygen reduction. The unique composition of the as-fabricated SAPC may provide further insight into this phenomenon with more comprehensive studies in the future.

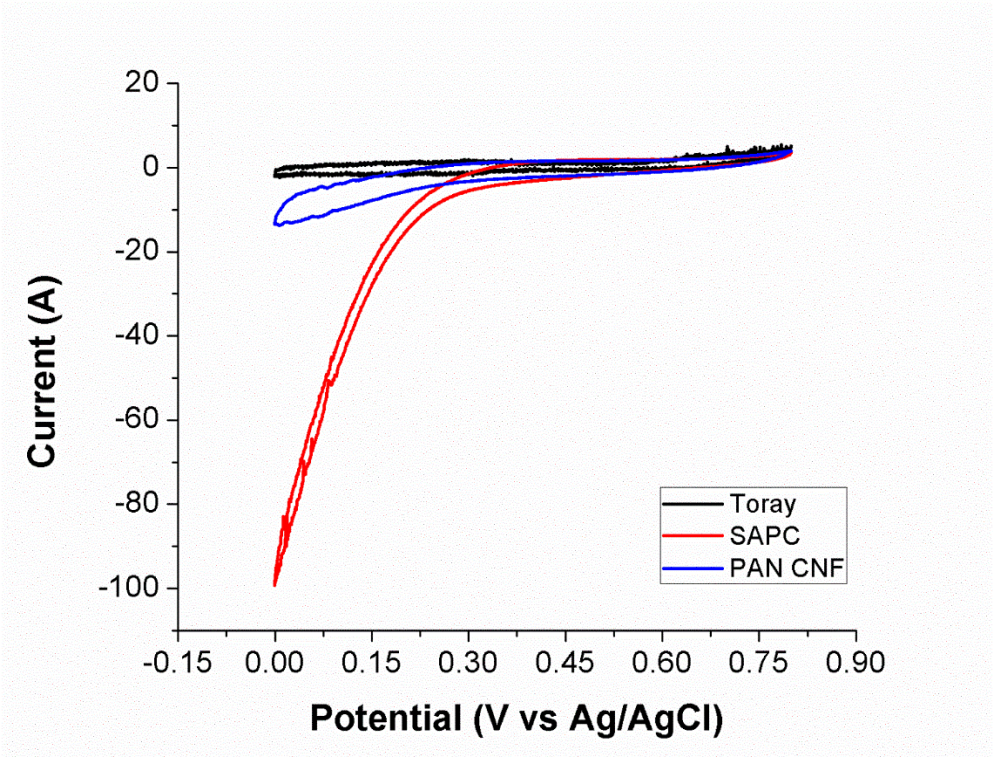

Figure 5.6. Cyclic Voltammetry Response of various carbon nanofiber electrodes for oxygen reduction.

5.4 Laccase Biosensor/Biofuel Cell

This section is reproduced in part with permission from ACS Catalysis submitted for publication. Unpublished work © 2018 American Chemical Society.

5.4.1 Introduction

Finally, SAPCs' enhanced electrocatalysis is further explored to gauge its potential as platform for Laccase immobilization in similar manner that was previously demonstrated with carbon nanotubes. As previously discussed, Laccase is a multicopper oxidase that is commonly utilized in biofuel cell applications for its highly efficient capability to reduce oxygen at a wide range of pH 4-7[233]–[235]. It has multiple electroactive sites imbedded in highly-conserved monomeric glycoprotein, one located on Type-1 (T1) copper oxidizing

phenolic substrates and the other on Type-2 (T2) and Type-3 (T3) copper clusters that reduce oxygen to water[235], [236] Intramolecular electron transfer between T1 and T2/T3 clusters occurs via highly-ordered histidine-cysteine-histidine peptide bridges, allowing insulated internal electron transfer in the protein matrix while possessing high catalytic efficiency at high redox potentials[237]. For efficient direct electron transfer (DET), the proximity of laccase and the surface of the electrode must be less than 1.5nm to allow for the quantum tunneling effect to occur[238], [239]. Therefore, researchers have been investigating various immobilization methods to properly orient laccases (T1 site) towards the electrodes to conduct efficient DET[161], [240], [240]–[243]. For example, in the work of *Fei et al*[242], orientation-controlled laccase immobilization on SWCNT was successfully conducted by simply using organic solvent as a surfactant, relying on the affinity of ethanol on enzymatic hydrophobic pockets of laccase and the substrate.

In this context, it was hypothesized that SAPC would demonstrate a similar capacity to serve as electron exchange platforms as SWCNT for Laccase immobilization. Therefore, electrochemical characterization of SAPCs was performed under various conditions to examine the overall effect of its heterogenous microstructures on laccase electrocatalysis of oxygen reduction. The results exhibit an overall enhancement in electrocatalytic performance of laccase on SAPCs with a remarkably high stability and large current density, compared to other traditional carbon materials. Furthermore, topographical studies of SAPCs were also conducted using High-Resolution Transmission Electron Microscopy (HR-TEM), X-ray photoelectron spectroscopy (XPS), and Raman spectroscopy. The finding of these studies reveals enriched graphitization within SAPCs compared to traditional polyacrylonitrile-derived pyrolytic carbon, possessing high concentration of

both graphitic edge planes and nitrogen heteroatoms. Therefore, this study reveals an outstanding capacity of the new class of pyrolytic carbon, SAPCS, as a promising carbon material for enhancing bioelectrocatalysis in biofuel cell application.

5.4.2 Materials and Methods

5.4.2.1. Materials and Apparatus

Polyacrylonitrile (PAN) solution (M.W. 150,000g/mol), commercial grade multi-walled carbon nanotubes (MWCNTs), and catalase (H_2O_2/H_2O_2 Oxidoreductase) from bovine liver were purchased from Sigma-Aldrich Co. LLC. N, N-dimethylformamide (DMF, 99.9%, B.P. = 157°C), citric acid monohydrate, sodium phosphate dibasic heptahydrate, sodium chloride, sodium fluoride, and hydrogen peroxide, ethyl alcohol, and Linberg Blue M Tube Furnace were purchased from ThermoFischer Scientific, Inc. Ultra-Pure Oxygen was purchased from Air Gas, Inc. Conductive carbon paste was purchased from Structure Probe, Inc. Citrate-phosphate buffers were prepared by mixing 0.1M of citric acid and 0.2M sodium phosphate dibasic heptahydrate solution until the desired pH 4.0 was achieved. Branson 2800 Cleaner was purchased from Branson Ultrasonics. Lab-Line Imperial II Radiant Heat Oven was purchased from Lab Line Instruments, Inc.

5.4.2.2 Laccase Source and Purification of Isoforms

Laccases were purified from *P. Sanguineus CS43*, a native white-rot fungus strain found in northeastern part of Mexico and were cultured at Universidad Autónoma de Nuevo León (Monterrey, NL, México). They were cultured at 4°C and sub-cultured weekly on 2°C (w/v) malt extract agar plate at 30°C before enzymes production as carried out[244]. New

Brunswick's 14-L Bioreactor was used for laccase production and fermentation for 11 days. The samples were then collected, filtered and centrifuged at 4000g for 10 minutes to acquire the crude enzyme extract of laccases. Further serial filtration steps were conducted to acquire purified enzyme extracts. FLUOstarTM Microplate Reader (420nm, BMG LABTECH, Ortenberg, Germany) was used to obtain the activity level of the laccase extracts by measuring the reaction of laccase with ABTS at a wavelength of 420nm (ε=36000 M^{-1} cm^{-1}). The activity was expressed in International Units (U), which is defined as the amount of enzyme that converts a micromole of substrate per minute (µmol / L / min).

5.4.2.3 Fabrication of Stress-Activated Pyrolytic CNF (SAPC) and pure PAN CNF (CNF)

Mechanically-treated carbon nanofibers mats were synthesized by far-field electrospinning technique using dispersed 8% PAN and 1% MWCNT in DMF solution. Electrospun carbon nanofibers (CNF) mats were then electromechanically compressed repeatedly to give the mat an even surface and preserve fiber alignment prior to its thermal treatment at 280°C in air for 6 hours. The stabilized CNF mats were then pyrolyzed in multiple-staged with a continuous flow of N_2 at a rate of 1scfm during the process, initially heated to 300°C at a rate of 4.5°C/min and dwelled at the temperature for an hour. Followed by increasing it to 1050°C at a ramp rate of 3°C/min, the furnace was held at the temperature for another hour before cooling to ambient temperature at a rate of 5°C/min. Pure PAN CNF (CNF) were electrospun without 1% CNT and were processed without mechanical treatment.

5.4.3.4 Immobilization of Laccases on electrodes

Each electrode was rinsed with 70% ethanol solution to increase its surface wettability by disrupting hydrophobic surfaces and then washed with deionized water thoroughly prior to enzyme loading (Figure 5.7). Laccase stock solution was diluted in a 2:1 (v/v) with deionized water followed by 1:1 dilution with 20% ethanol solution. The mixed solution was then dropped onto Toray, SAPC, or CNF electrode and was dried completely with a heat gun for 5 minutes for sufficient enzymatic adsorption on the electrodes.

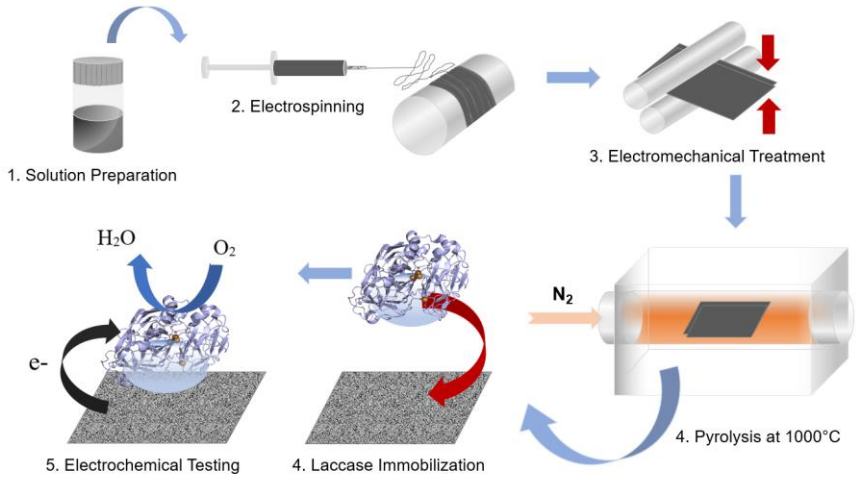

Figure 5.7. Schematic of electrode fabrication of SAPC. Fabrication of CNF electrode skips step 3. Reproduced with permission from ACS Catalysis submitted for publication. Unpublished work © 2018 American Chemical Society.

5.4.3.5. Electrochemical Analysis

Enzyme-immobilized electrodes were characterized by electrochemical measurement at room temperature using Princeton Applied Research VersaSTAT 4 Potentiostat running VersaStudio 2.48.5. software. For half-cell test, a conventional 3-electrode cell setup was used with an Ag/AgCl reference electrode (in a saturated 3M KCl solution) and commercial grade glassy carbon electrode as a counter electrode. The experiments were conducted in a

sealed 100mL-glass container containing 50mL of citrate/phosphate buffer at pH 4.0. Chronoamperometry, EIS, and cyclic voltammetry with a scan rate (V/s) of 0.005 were recorded. For O_2 saturation test, O_2 gas flows were set at 1 scfm to obtain reproducible conditions for each experiment. Current densities were measured using EIS and geometric surface areas of the electrodes. For stability study, chronoamperometry (CA) was used and collected data under O_2 saturated solution with the flow rate of 1 scfm for 12 hours. For the O_2 and N_2 saturation study, the buffer was purged with oxygen or nitrogen in a sealed glass container for 10 minutes prior to measurement. All electrochemical measurements were obtained in a citrate/phosphate buffer at pH 4.0, an overlapping optimal pH environment suited for both isoforms of Laccase from *Pycnoporus Sanguineus,* LAC-1 and LAC-2[237], [244]. All data were measured in triplicates.

5.4.3.6 UV-Vis Absorption Spectroscopy: Leaching Study

To further examine the stability of laccase immobilization, UV-Vis spectrophotometric analysis was used to obtain quantitative measurement of laccases leaching from the bioelectrodes. UV-Vis spectra for these specific laccases was monitored at 280nm and measured via Cary-60 Spectrophotometer. Absorbance measurements were obtained every 5 minutes consecutively for 2 hours. All measurements were obtained in triplicates.

5.4.3 Results and Discussion

5.4.3.1 Raman Spectroscopy

While HR-TEM is a superb tool for understanding the underlying carbon microstructures, Raman spectroscopy allows us to further differentiate the breadth of graphitization in

these microstructures by delivering quantitative analysis of enhancement in degree and uniformity of graphitization. Raman spectrum shown in Figure 5.8 are the averaged spectrum collected from over 100 randomly selected areas of each carbon electrode. The degree of graphitization can be gauged by the ratio of the D peak, located between 1300 – 1400 cm^{-1}, and the G peak, located between 1560 – 1600 cm^{-1}. The G peak correlates with the vibration mode of the sp-2-hybridized graphene planes, whereas the D peak represents the degree of disorder within the sp-2-hybridized planes. In this context, high degree of graphitization correlates with a lower D/G ratio (I_d/I_g). Based on the results of the Raman spectroscopy shown in Figure 5.8, we see an increasing trend of graphitization from CNF to SAPC to Toray that reflects what is seen in the HR-TEM micrographs. Here it is important to not only point out the enhanced I_d/I_g of 0.73 ± 0.036 of the SAPC from that of CNF with a I_d/I_g of .95 ± 0.003, but also small standard deviation. This is particularly significant for electrochemical applications as it indicates homogeneity of the graphitization throughout the sap CNF electrode, which should be reflected by a greater degree of electrocatalytic activity.

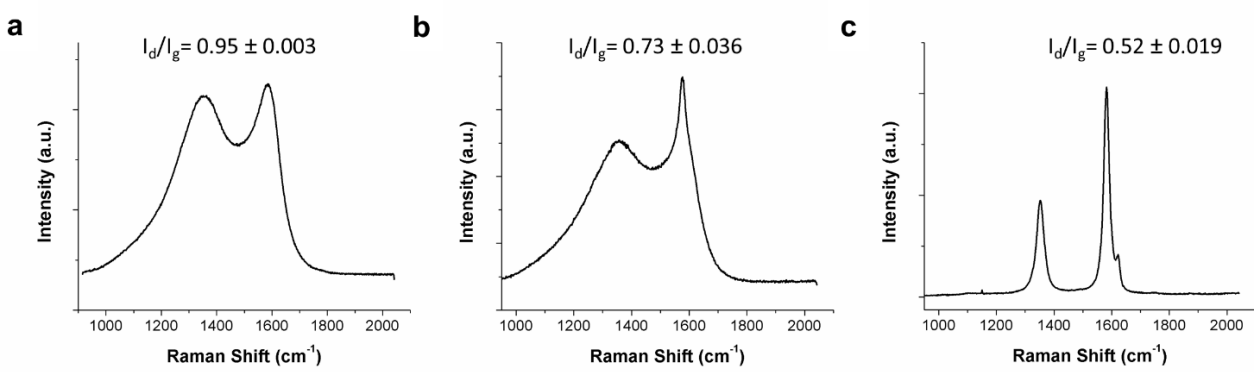

Figure 5.8. Raman spectroscopic comparison of peak intensities and peak width of (a)CNF, (b)SAPC, (c)Toray. Reproduced with permission from ACS Catalysis submitted for publication. Unpublished work © 2018 American Chemical Society.

5.4.3.2 X-Ray Photoelectron Spectroscopy (XPS)

Carbon's electrochemical performance is largely defined by the quantity of "defect" sites within its sp2-hybridized planes, which are primarily consists of graphitic edge planes and heteroatoms. These "defects" greatly increase the electronic state density of the carbon microstructures, and is, therefore, responsible for its electron transfer processes. In this aspect, it is apt to perform X-ray Photoelectron Spectroscopy (XPS) to determine the elemental composition of the carbon microstructures. The XPS spectrum shown in Figure 5.9. reveals the presence the nitrogen and oxygen heteroatoms within SAPC composition. The 2.85% content oxygen could largely be disregarded as prior studies have shown that oxygen content below 7% has negligible impact on the electrochemical performance of the carbon[193]. However, the 7% of nitrogen is very significant, especially the nature of these nitrogen heteroatoms. Further analysis with Lorentzian fitting reveals graphitic nitrogen (67.4%) and pyridinic nitrogen (32.6%), which have been demonstrated to have profound impact on the electrocatalysis for other graphitic allotropes such as graphene and carbon

nanotubes. Hence, it is anticipated from the results of the materials characterization that SAPC should exhibit good electron transfer kinetics with Laccase's T1 copper redox center.

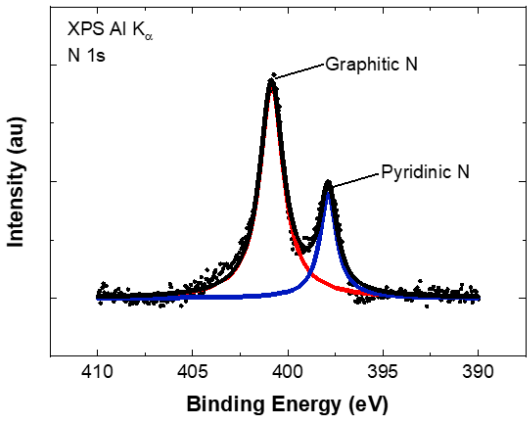

Component (BE)	at.% sapCNF
Pyridinic-N (398.0 eV)	32.6
Pyrrolic-N (400.1 eV)	~0*
Graphitic-N (401.2 eV)	67.4

Elemental Components	pCNF	sapCNF	Toray
C 1s	91.25%	91.31%	97.96%
N 1s	5.60%	5.84%	~0%
O 1s	3.15%	2.85%	2.04%

Figure 5.9. XPS Analysis of SAPC and Elemental Components of (a)CNF, (b)SAPC, (c)Toray. Reproduced with permission from ACS Catalysis submitted for publication. Unpublished work © 2018 American Chemical Society

5.4.3.3 Electrochemical Characterization of Bioelectrodes

Electrochemical analyses were conducted to investigate how structurally-varied carbons can alter the electrocatalytic behavior of laccases. In Figure 5.10, the onset potential of LAC-1 oxygen reduction reaction (ORR) for SAPC started at 650 ± 6mV (vs Ag/AgCl) which was comparable to that of Toray at 648 ± 7mV and CNF at 650 ± 9mV. Similarly, LAC-2 on SAPC exhibited the earliest onset potential at 657 ± 4mV (vs Ag/AgCl), followed by Toray and CNF, observed at 655 ± 8mV and 651 ± 3mV, respectively. The onset reduction potential of laccases is determined by the reaction kinetics of electron exchange between the laccase and the electrode, the nature of enzymatic activities, and the efficiency of enzyme immobilization. Based on these driving factors and the measured onset potential, both laccases did not have any preferential catalytic behavior. Despite the comparable onset

potentials among all electrodes, CNF with LAC-1 displayed the earliest peak potential at 480±15mV under ambient condition. This was slightly earlier than other two, LAC-1-SAPC and LAC-1-Toray which peaked at 473±40mV and 465±23mV, respectively. Based on the results for LAC-1, the large variation in peak potential for all three electrodes with the relatively small change with the respect to these variations indicate that LAC-1 had shown no preferential performance towards specific carbons.

In Figure 5.11, LAC-2 with SAPC peaked at 523±21mV, followed by CNF and Toray, at 498±15mV and 470±6mV, respectively. The study by *Orlikowska et al*[237], LAC-1 had a polar protein residue, Serine 195, at its hydrophobic pocket, creating an additional hydrogen bonding in the presence of polarized atoms. The proneness of LAC-1 to form intrahelical hydrogen bonding with water molecules may increases the physical distance between laccase and electrode. Since all carbon electrodes in this experiment were treated with ethanol to increase the surface wettability of the electrodes, LAC-1 may not show a preferential performance. Conversely, LAC-2's earliest peak with SAPC may be due to its replacement of Serine 185 with Alanine 185, a hydrophobic amino acid (a.a.) residing near the T1 site pocket. Therefore, this additional hydrophobic molecule may prefer more hydrophobic carbon structures such as SAPC and Toray for forming a hydrophobic interaction with graphitic carbons. Additionally, the edge planes and heteroatoms of SAPC also contribute to its faster peak potential than Toray. Although Toray is more graphitic, its lack of heterogenous atoms and edge planes on the surface makes the interfacial electron transfer between laccase and electrode more sluggish. Therefore, in the case of Lac-2 (Figure 5.11), CNF exhibited an earlier peak than Toray due to its highly-reactive surface attributed by heterogeneous groups. In this respect, the joint effects of noncovalent

bonding and the heterogenous surface of SAPC create more favorable ambiance for faster electrocatalytic reaction of LAC-2.

More evident effects of carbon microstructures on the electrocatalytic activity of laccases is shown when comparing the current densities of the electrodes. In Figures 5.10 and 5.11, both LAC-1 and LAC-2 immobilized on SAPC revealed the highest current density at 266.7±61 μA/cm^2 and 212±26 μA/cm^2, respectively. The current density of LAC-1 on Toray was 123±23 μA/cm^2 while LAC-2 had 165±20 μA/cm^2, resulting in a lower current density than SAPC but higher than CNF. This was due to the presence of highly-graphitic areas available for laccases, but, a lack of heteroatoms on the surface of CNF, resulting in slow y-axial electron transfer. Regardless of its earlier onset and peak potential for LAC-1, CNF exhibited the lowest current density at 15±2 μA/cm^2 for LAC-1 and 11±2μA/cm^2 for LAC-2.

Similar trends were observed where SAPC had the highest current density at 375±31μA/cm^2 for LAC-1 and 600±39μA/cm^2 for LAC-2, compared to Toray (180±20μA/cm^2 for LAC-1 and 251±11μA/cm^2 for LAC-2). The lowest current density was observed in CNF with LAC-1 and LAC-2 at 39±10μA/cm^2 and 48±2μA/cm^2. The kinetics, conductivity, and active site availability of electrodes accounts for this current density. In this case, the effect of conductivity can be ruled out since Toray, which has the highest conductivity among those studied[10], did not reveal the highest current density as shown in Figure 5.10c and 5.11c CNF saw the lowest current density which may have been due to it having limited active sites available for laccase immobilization. Although both Toray and SAPC have graphitic structures, SAPC's faster electron transfer at the interface of electrode

and laccase and high concentration of laccase per area, due to its heterogenous microstructure, give SAPC the highest current density as seen in both Figure 5.10 and 5.11.

Furthermore, in the work of *Holmberg et al*[245], LAC-1 and LAC-2, derived from the same strain, produced high density at 825 ± 88 μA/cm^2 and 1220 ± 106 μA/cm^2, reporting with the loading concentration of 822±6kU/L and 2890±5kU/L, respectively. Compared to the previous study, SAPCs showed higher current densities for both LAC-1 and Lac-2 with respect to the given loading concentration of laccases. These overall electrochemical analyses reveal SAPCs as an excellent platform for highly-efficient bioelectrocatalysis in laccase biofuel cell system.

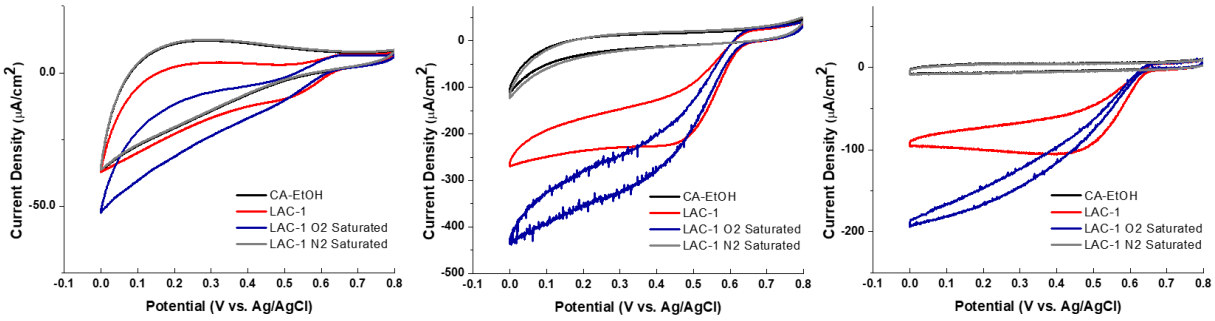

Figure 5.10. Cyclic voltammograms of LAC-1 on bioelectrodes: (a) CNF, (b) SAPC, and (c) Toray at a scan rate of 5mV/s in citrate/phosphate buffer at pH 4.0 without laccase (black), with laccase (red) under hydrostatic condition, laccase under hydrodynamic condition by continuous oxygen bubbling (blue), laccase under hydrodynamic condition by continuous nitrogen bubbling (grey). Reproduced with permission from ACS Catalysis submitted for publication. Unpublished work © 2018 American Chemical Society.

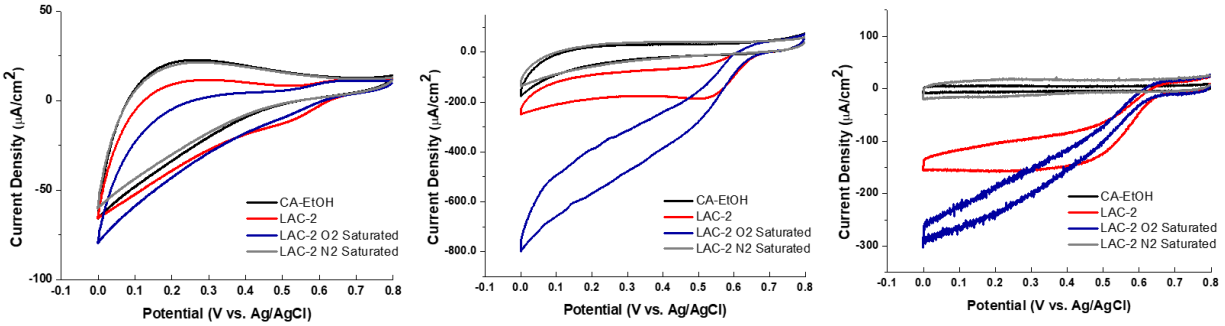

Figure 5.11. Cyclic voltammograms of LAC-2 on bioelectrodes: (a) CNF, (b) SAPC, and (c) Toray at a scan rate of 5mV/s in citrate/phosphate buffer at pH 4.0 without laccase (black), with laccase (red) under hydrostatic condition, laccase under hydrodynamic condition by continuous oxygen bubbling (blue), laccase under hydrodynamic condition by continuous nitrogen bubbling (grey). Reproduced with permission from ACS Catalysis submitted for publication. Unpublished work © 2018 American Chemical Society

5.4.3.4 Electrochemical Stability

One of the requirements for ensuring the long-term stability of performance of enzymatic biofuel cell is vastly relied on the catalytic stability of enzymes immobilized on the surface of biocathode over time. Therefore, the stability study was conducted to investigate the effect of microstructures of each carbon electrode on the catalytic stability of immobilized laccases for 12 hours.

In Figure 5.12, LAC-1 in SAPC exhibited the highest catalytic stability, losing only 23±9% of its initial current density, followed by that in Toray and CNF, losing 63±4% and 69±1%, respectively. Sharp incline in leaching (%) is observed across all the electrodes within 1st hour of the experiment and gradually decreases as most of loosely-bound laccases initially leaches off by convection driven by continuous oxygen bubbling. Similarly, LAC-2 in SAPC retained the most stable catalytic activity of LAC-2, losing 34±6% while Toray and CNF lost

36±17% and 57±1%, respectively. As previously mentioned, laccase immobilized by ethanol can be achieved via the high affinity of ethanol to the hydrophobic regions of both electrode and enzyme, orienting the enzymes favorable for efficient electron transfer via quantum tunneling[237]. Since its methodology involves in creating a noncovalent interaction (i.e. pie-pie stacking) between hydrophobic sites of substrates, higher degree and uniformity of graphitization can be an optimal ambiance for such reaction to occur, resulting in a less leaching effect of immobilized laccase and conferring a protection via weak chemical bonding to keep laccase intact on the electrode during the extensive stability experiment.

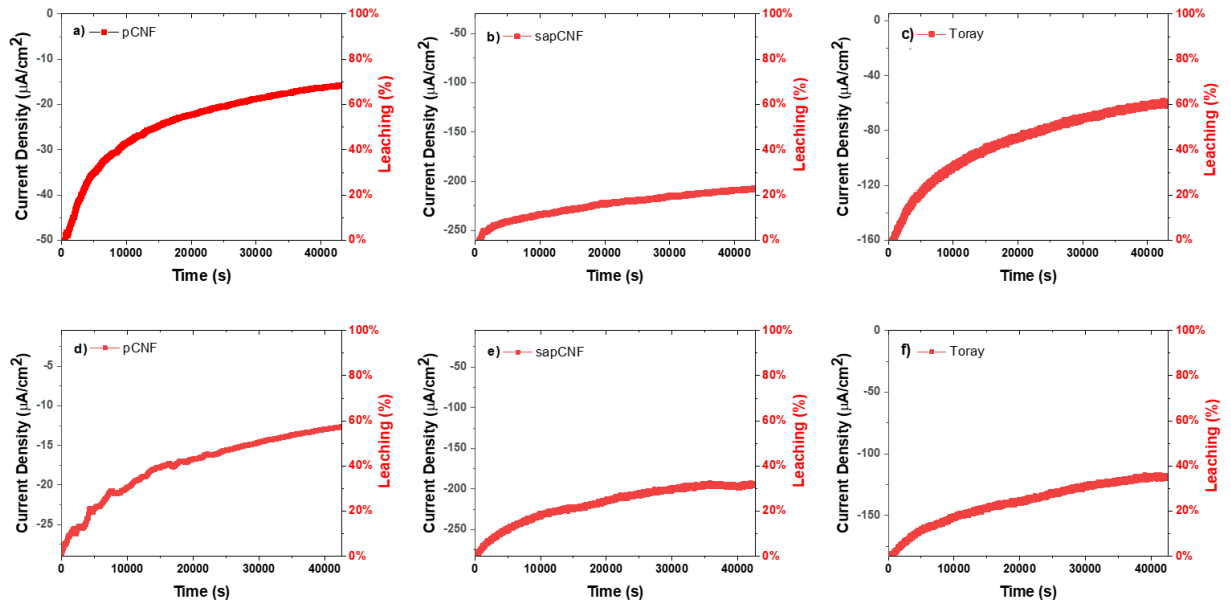

Figure 5.12. Chronoamperometric measurement of stability test on: LAC-1 on (a) CNF, (b) SAPC, (c) Toray, and LAC-2 on (d) CNF, (e) SAPC, and (f) Toray bioelectrodes at 0.4V vs Ag/AgCl in citrate/phosphate buffer at pH 4.0 under continuous O_2 bubbling at room temperature for 12 hr. Reproduced with permission from ACS Catalysis submitted for publication. Unpublished work © 2018 American Chemical Society.

5.4.3.5 Leaching Study: UV-Vis Absorption Spectrometer

The results of electrochemical stability test revealed the enhanced stability of SAPC. Since the electrodes were all immobilized with the same isoforms of laccase, it is believed that the drop in current density likely stems from leaching of the laccase from the surface of the electrodes due to weaker surface attachment. To corroborate this effect, UV-vis absorption spectroscopy was performed to measure the leaching rate of each electrode. Each carbon electrode immobilized with Laccase is dipped into a quartz cuvette containing DI water and the absorption spectrum is scanned from 500 nm to 190 nm is measured periodically over the course of 2 hours. Enzymes typically show a peak response at 280 nm associated with their amine and carboxylate groups, which are present within the Laccase macromolecule structure. Indeed, the spectrum showed a clear plateau starting at 280 nm after the introduction of the enzymes solution. A spectrum of 20% ethanol is also taken and shows only a small spike after 200 nm, indicating that ethanol does not interfere with the measurement of leached laccase. The absorption peak intensity at 280 nm is therefore used to judge the amount of enzyme leached.

The results of the UV absorption leaching test show that the rate of leaching corresponds well with the loss seen in the electrochemical stability test (Figure 5.13). The amount of leaching in CNF was more than 3 times larger after 2 hours in DI than SAPC for both isoforms of Laccase and also saw a comparable degree of drop in electrochemical response than both SAPC. In contrast, the difference in stability response between SAP-CNF and Toray is subtler. For Lac-2, SAPC has larger initial drops in current density and large leaching within the first 1 hr, but becomes more stable later on, with a lower rate of leaching than Toray. The larger initial leaching may stem from the larger surface area of SAPC, which would trap more enzymes within its pores that leach out more rapidly as they

are not as strong adsorbed to the surface of the fibers. The lower rate of leaching after this initial drop, may indicate that SAPC is more stable than even Toray in longer stability test. For Lac-1, SAPC outperforms both Toray and CNF in stability by more than 2 folds in both UV leach rate and electrochemical response. Here, it is interesting to note that Toray's stability substantially dropped in comparison and is comparable to the stability of CNF. This likely stem from the extra hydrogen bond, which also impacted the electrochemical kinetics as described earlier.

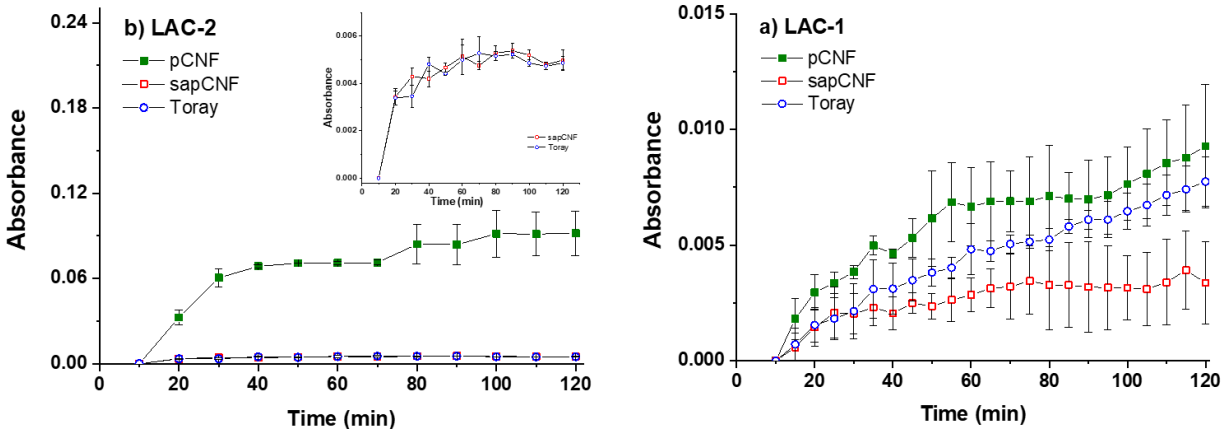

Figure 5.13. UV Absorption Spectroscopy Leaching Study. Carbon Nanofiber electrodes with a) Lac-2 and b) Lac-1 were soaked in DI and the Leaching of the Laccase were measured by the peak seen at 280 nm over the course of 2 hours. Reproduced with permission from ACS Catalysis submitted for publication. Unpublished work © 2018 American Chemical Society.

5.4.3 Conclusion

In this chapter, we explored the capacity for stress-activated pyrolytic carbon nanofiber (SAPC) to serve as an efficient platform for Laccase-catalyzed oxygen reduction, dopamine sensor oxygen sensor and hydrogen peroxide sensor. SAPC is a new class of pyrolytic

carbon that has been shown to demonstrate remarkable electrocatalytic activity without additional activation process. Prior studies of its electrocatalysis demonstrates that SAPC has a particularly high electrocatalysis for surface and adsorption sensitive redox species, marking it as an effective platform for bioelectrochemical application. Cyclic Voltammetry was performed on various carbon electrodes to evaluate their capacity to facilitate efficient electron transfer as well as the stability of their electrocatalysis. Indeed, the results showed that among the carbon electrodes evaluated, SAPC exhibited the highest electron transfer efficiency as demonstrated by high current density.

For Laccase electrodes in particular, SAPC exhibited enhanced electrocatalysis, with peak potential that are greater than 20 mV of the other two carbon electrodes. Furthermore, the highly-adsorptive surface of SAP-CNF demonstrated high electrochemical stability, resulting in 3 times lower loss in current density than CNF. In this regard, both SAPC and Toray showed their enhanced electrochemical stability, indicating that the loss in performance for CNF may have stem from the leaching of immobilized laccases on the electrode. A closer comparison of the stability between SAPC and Toray, SAPC showed smaller loss in performance after the first hour of testing, suggesting that SAPC could have even greater long-term stability than Toray. Moreover, despite its circumstance to undergo its denaturation due to the presence of ethanol, laccase strain of *Pycnoporus Sanguineus CS43* still retained its enzymatic activities for electrochemical performance. Based on these results, SAPC may be an optimal platform for highly-efficient oxygen reduction in biofuel cell and biosensing application.

5 – Conclusion and Future Outlook

In this work, we discussed how electro-mechanical parameters of synthesis influence molecular alignment in a polymer precursor to enhance its graphitization. We focused on carbonization of polyacrylonitrile as the carbon precursor, since it is generally considered a "non-graphitizing polymer" and is a main source for commercial carbon fibers. The application of electrospinning allowed us to utilize electrohydrodynamic forces, boosted by addition of carbon nanotubes, to align polymer molecular chains within the spun fibers. The polymer chain alignment was then preserved by mechanical compression of the polymer fabrics during the formative stabilization step. Subsequently, a myriad of material analysis techniques, including Raman spectroscopy, transmission electron microscopy, electrical conductivity, and electrochemical measurements allowed us to evaluate the graphitization level of the pyrolyzed PAN specimen. Pyrolyzing the curved polymer chains lead to formation of amorphous carbon or fullerenic structures, whereas mechanically aligned carbon precursors are poised to form more graphitic carbon planes. This result underlines the correlation between the physical conditions exerted on a stabilizing polymer and its graphitization, thereby, emphasizing that the foundation of the final carbon structure is cast during the stabilization of the precursor polymer.

Graphitization of organic precursors is a complex phenomenon and it is unlikely to find a comprehensive solution to develop graphitic carbons from different polymer precursors. This work addresses the physical aspect of polymer graphitization and explores the influence of the synthesis parameters on the microstructure of the pyrolytic carbons. By investigating the effects of applied electro-mechanical stresses during the carbon synthesis process, the presented results reveal further insight into the underlying mechanism of graphitization and provides an attractive pathway for tailoring the microstructure of carbon materials.

This is particularly the case when considering the impact on the electrochemical performance of the resulting carbon. The presence of intrinsic lattice "disorders" and heterogeneous nitrogen atoms within the carbon yield enhanced electrocatalytic behavior from the as-fabricated carbon electrodes. The resulting carbon exhibit an oriented but fragmented lattice structure, as visualized by HRTEM imaging. Further material characterization with XPS indicates that the pyrolytic carbon derived from PAN is innately rich in nitrogen heteroatoms. The presence of these chemical and structural "defects" in the SAPC prompted us to perform a comprehensive electrochemical study with surface insensitive (potassium hexachloroiridite), surface sensitive (potassium ferricyanide), and adsorption sensitive (dopamine) electroactive species. The electrochemical kinetics show that SAPC's heterogenous electron transfer rate is 20 to 35 times higher than that of standard pyrolytic PAN carbons and 2 to 10 times higher than polished commercial glassy carbon in both the surface insensitive and sensitive redox probes. The results indicate a correlation between the enhanced sensitivity of SAPC towards surface sensitive species and the numerous graphitic edges and nitrogen heteroatoms present in the carbon lattice.

The presence of these “defects” is associated with the quantity of the electroactive sites on the carbon electrodes.

The unique electrocatalytic behavior of SAPC allows for an efficient and simultaneous detection of dopamine (DA), ascorbic acid (AA), and uric acid (UA), without the need for additional activation or post-processing of the pyrolytic carbon. The results demonstrate that SAPC has a sensitivity and limit of detection for dopamine that compares favorably with expensive graphene and CNT based sensors. The capability of SAPC for detecting biomarkers accentuates its potential for biomedical sensing applications. Additionally, the SAPC exhibits an enhanced mechanical stability compared to its graphene-based counterparts. In fact, the electrochemical behavior of SAPC is so similar to graphene’s that it exhibited other electrocatalytic capabilities akin to the carbon nanoallotrope. Specifically, the capacity for oxygen and hydrogen peroxide reduction due to the presence of nitrogen-heteroatoms, as in nitrogen-doped graphene[183], [217], [226], [231]. In addition, it was demonstrated how the SAPC could serve as an ideal platform for laccase immobilization for oxygen reduction process in enzymatic fuel cell applications.

It is important to note that the mere presence of heterogeneous atoms and edge planes in carbon structure does not constitute enhanced electrochemical behavior, since their effect could be countered by a low-degree of graphitization in the resulting carbon. The results reported here suggest that a key concept in carbon’s electrochemistry is the right amount of select “disorders” within a generally “ordered” framework. The former increases the localized DOS around the E° of the redox systems of interest, facilitating heterogeneous electron transfer, and the latter provides paths of least resistance for electron transport

within the carbon electrode. The proposed stress-induced approach produces a graphitic framework, incorporating heteroatoms and structural features that are tuned for electrochemical performance.

Current work on applying the SAPCs to various other applications that has not been described in this work includes biomedical applications such as iodide ions sensor and dopaminergic stem cell growth and differentiation. A tremendous effort to manipulate the carbon's microstructure has been made to improve uniformity with varying degree of graphitization. Finally, there is also a concerted effort being made to develop strategies for patterning the SAPCs to fully integrate the technology into other C-MEMS applications. The application described in this work as well as future application potentially foreshadows an exciting new-wave of C-MEMS driven technology.

Bibliography

[1] C. Wang and M. Madou, "From MEMS to NEMS with carbon," *Biosens. Bioelectron.*, vol. 20, no. 10, pp. 2181–2187, Apr. 2005.

[2] H. Xu, K. Malladi, C. Wang, L. Kulinsky, M. Song, and M. Madou, "Carbon post-microarrays for glucose sensors," *Biosens. Bioelectron.*, vol. 23, no. 11, pp. 1637–1644, Jun. 2008.

[3] C. Wang, G. Jia, L. H. Taherabadi, and M. J. Madou, "A novel method for the fabrication of high-aspect ratio C-MEMS structures," *J. Microelectromechanical Syst.*, vol. 14, no. 2, pp. 348–358, Apr. 2005.

[4] R. R. Kamath and M. J. Madou, "Three-Dimensional Carbon Interdigitated Electrode Arrays for Redox-Amplification," *Anal. Chem.*, vol. 86, no. 6, pp. 2963–2971, Mar. 2014.

[5] J. Bauer, A. Schroer, R. Schwaiger, and O. Kraft, "Approaching theoretical strength in glassy carbon nanolattices," *Nat. Mater.*, vol. 15, no. 4, pp. 438–443, Apr. 2016.

[6] P. J. F. Harris, "Structure of non-graphitising carbons," *Int. Mater. Rev.*, vol. 42, no. 5, pp. 206–218, 1997.

[7] S. Sharma and M. Madou, "Micro and nano patterning of carbon electrodes for bioMEMS," *Bioinspired Biomim. Nanobiomaterials*, vol. 1, no. 4, pp. 252–265, Aug. 2012.

[8] G. S. Bisht, S. Holmberg, L. Kulinsky, and M. Madou, "Diffusion-Free Mediator Based Miniature Biofuel Cell Anode Fabricated on a Carbon-MEMS Electrode," *Langmuir*, vol. 28, no. 39, pp. 14055–14064, Oct. 2012.

[9] R. L. McCreery, "Advanced Carbon Electrode Materials for Molecular Electrochemistry," *Chem. Rev.*, vol. 108, no. 7, pp. 2646–2687, Jul. 2008.

[10] M. Ghazinejad, S. Holmberg, O. Pilloni, L. Oropeza-Ramos, and M. Madou, "Graphitizing Non-graphitizable Carbons by Stress-induced Routes," *Sci. Rep.*, vol. 7, no. 1, p. 16551, Nov. 2017.

[11] Q. L. Zhang *et al.*, "Reactivity of Large Carbon Clusters: Spheroidal Carbon Shells and Their Possible Relevance to the Formation and Morphology of Soot," *J Phys Chem U. S.*, vol. 90:4, no. 4, Feb. 1986.

[12] S. Iijima, "Helical microtubules of graphitic carbon," *Nature*, vol. 354, no. 6348, p. 56, 1991.

[13] K. S. Novoselov *et al.*, "Electric Field Effect in Atomically Thin Carbon Films," *Science*, vol. 306, no. 5696, pp. 666–669, Oct. 2004.

[14] G. Centi and S. Perathoner, "Carbon Nanotubes for Sustainable Energy Applications," *ChemSusChem*, vol. 4, no. 7, pp. 913–925, Jul. 2011.

[15] S. K. Tiwari, V. Kumar, A. Huczko, R. Oraon, A. D. Adhikari, and G. C. Nayak, "Magical Allotropes of Carbon: Prospects and Applications," *Crit. Rev. Solid State Mater. Sci.*, vol. 41, no. 4, pp. 257–317, Jul. 2016.

[16] K. S. Kim *et al.*, "Large-scale pattern growth of graphene films for stretchable transparent electrodes," *Nature*, vol. 457, no. 7230, pp. 706–710, Feb. 2009.

[17] M. F. El-Kady, V. Strong, S. Dubin, and R. B. Kaner, "Laser Scribing of High-Performance and Flexible Graphene-Based Electrochemical Capacitors," *Science*, vol. 335, no. 6074, pp. 1326–1330, Mar. 2012.

[18] T. Georgiou *et al.*, "Vertical field-effect transistor based on graphene–WS_2 heterostructures for flexible and transparent electronics," *Nat. Nanotechnol.*, vol. 8, no. 2, pp. 100–103, Feb. 2013.

[19] M. Pumera, "Electrochemistry of graphene, graphene oxide and other graphenoids: Review," *Electrochem. Commun.*, vol. 36, pp. 14–18, Nov. 2013.

[20] A. Ambrosi, C. K. Chua, A. Bonanni, and M. Pumera, "Electrochemistry of Graphene and Related Materials," *Chem. Rev.*, vol. 114, no. 14, pp. 7150–7188, Jul. 2014.

[21] D. A. C. Brownson, D. K. Kampouris, and C. E. Banks, "Graphene electrochemistry: fundamental concepts through to prominent applications," *Chem. Soc. Rev.*, vol. 41, no. 21, p. 6944, 2012.

[22] M. M. J. Treacy, T. W. Ebbesen, and J. M. Gibson, "Exceptionally high Young's modulus observed for individual carbon nanotubes," *Nature*, vol. 381, no. 6584, pp. 678–680, Jun. 1996.

[23] B. G. Demczyk *et al.*, "Direct mechanical measurement of the tensile strength and elastic modulus of multiwalled carbon nanotubes," *Mater. Sci. Eng. A*, vol. 334, no. 1, pp. 173–178, Sep. 2002.

[24] W. Primak and L. H. Fuchs, "Electrical Conductivities of Natural Graphite Crystals," *Phys. Rev.*, vol. 95, no. 1, pp. 22–30, Jul. 1954.

[25] A. K. Dutta, "Electrical Conductivity of Single Crystals of Graphite," *Phys. Rev.*, vol. 90, no. 2, pp. 187–192, Apr. 1953.

[26] T. Ando, "The electronic properties of graphene and carbon nanotubes," *NPG Asia Mater.*, vol. 1, no. 1, pp. 17–21, Oct. 2009.

[27] X. Li, X. Wang, L. Zhang, S. Lee, and H. Dai, “Chemically Derived, Ultrasmooth Graphene Nanoribbon Semiconductors,” *Science*, vol. 319, no. 5867, pp. 1229–1232, Feb. 2008.
[28] R. H. Baughman, A. A. Zakhidov, and W. A. de Heer, “Carbon Nanotubes--the Route Toward Applications,” *Science*, vol. 297, no. 5582, pp. 787–792, Aug. 2002.
[29] M. S. Strano *et al.*, “Electronic Structure Control of Single-Walled Carbon Nanotube Functionalization,” *Science*, vol. 301, no. 5639, pp. 1519–1522, Sep. 2003.
[30] T. W. Odom, J.-L. Huang, P. Kim, and C. M. Lieber, “Atomic structure and electronic properties of single-walled carbon nanotubes,” *Nature*, vol. 391, no. 6662, pp. 62–64, Jan. 1998.
[31] A. G. Güell, N. Ebejer, M. E. Snowden, J. V. Macpherson, and P. R. Unwin, “Structural Correlations in Heterogeneous Electron Transfer at Monolayer and Multilayer Graphene Electrodes,” *J. Am. Chem. Soc.*, vol. 134, no. 17, pp. 7258–7261, May 2012.
[32] K. Ping Loh, Q. Bao, P. Kailian Ang, and J. Yang, “The chemistry of graphene,” *J. Mater. Chem.*, vol. 20, no. 12, pp. 2277–2289, 2010.
[33] F. A. de Bruijn, V. a. T. Dam, and G. J. M. Janssen, “Review: Durability and Degradation Issues of PEM Fuel Cell Components,” *Fuel Cells*, vol. 8, no. 1, pp. 3–22, Feb. 2008.
[34] N. Zamel *et al.*, “Experimental measurements of effective diffusion coefficient of oxygen–nitrogen mixture in PEM fuel cell diffusion media,” *Chem. Eng. Sci.*, vol. 65, no. 2, pp. 931–937, Jan. 2010.
[35] Z. Zhu, L. Garcia-Gancedo, A. J. Flewitt, H. Xie, F. Moussy, and W. I. Milne, “A Critical Review of Glucose Biosensors Based on Carbon Nanomaterials: Carbon Nanotubes and Graphene,” *Sensors*, vol. 12, no. 5, pp. 5996–6022, May 2012.
[36] C. B. Jacobs, M. J. Peairs, and B. J. Venton, “Review: Carbon nanotube based electrochemical sensors for biomolecules,” *Anal. Chim. Acta*, vol. 662, no. 2, pp. 105–127, Mar. 2010.
[37] W. Shi, X. Li, and H. Ma, “A Tunable Ratiometric pH Sensor Based on Carbon Nanodots for the Quantitative Measurement of the Intracellular pH of Whole Cells,” *Angew. Chem.*, vol. 124, no. 26, pp. 6538–6541, Jun. 2012.
[38] R. R. Moore, C. E. Banks, and R. G. Compton, “Basal Plane Pyrolytic Graphite Modified Electrodes: Comparison of Carbon Nanotubes and Graphite Powder as Electrocatalysts,” *Anal. Chem.*, vol. 76, no. 10, pp. 2677–2682, May 2004.
[39] I. Streeter, G. G. Wildgoose, L. Shao, and R. G. Compton, “Cyclic voltammetry on electrode surfaces covered with porous layers: An analysis of electron transfer kinetics at single-walled carbon nanotube modified electrodes,” *Sens. Actuators B Chem.*, vol. 133, no. 2, pp. 462–466, Aug. 2008.
[40] J. Zhang, *PEM Fuel Cell Electrocatalysts and Catalyst Layers: Fundamentals and Applications*. Springer Science & Business Media, 2008.
[41] Q. Chen and G. M. Swain, “Structural Characterization, Electrochemical Reactivity, and Response Stability of Hydrogenated Glassy Carbon Electrodes,” *Langmuir*, vol. 14, no. 24, pp. 7017–7026, Nov. 1998.
[42] S. C. Wang, K. S. Chang, and C. J. Yuan, “Enhancement of electrochemical properties of screen-printed carbon electrodes by oxygen plasma treatment,” *Electrochimica Acta*, vol. 54, no. 21, pp. 4937–4943, Aug. 2009.
[43] S. Kundu *et al.*, “Electrocatalytic Activity and Stability of Nitrogen-Containing Carbon Nanotubes in the Oxygen Reduction Reaction,” *J. Phys. Chem. C*, vol. 113, no. 32, pp. 14302–14310, Aug. 2009.
[44] J. Wang and L. D. Hutchins, “Activation of glassy carbon electrodes by alternating current electrochemical treatment,” *Anal. Chim. Acta*, vol. 167, pp. 325–334, Jan. 1985.
[45] S.-M. Li *et al.*, “Controllable synthesis of nitrogen-doped graphene and its effect on the simultaneous electrochemical determination of ascorbic acid, dopamine, and uric acid,” *Carbon*, vol. 59, pp. 418–429, Aug. 2013.
[46] H. Wang, T. Maiyalagan, and X. Wang, “Review on Recent Progress in Nitrogen-Doped Graphene: Synthesis, Characterization, and Its Potential Applications,” *ACS Catal.*, vol. 2, no. 5, pp. 781–794, May 2012.
[47] C. Zhang, N. Mahmood, H. Yin, F. Liu, and Y. Hou, “Synthesis of Phosphorus-Doped Graphene and its Multifunctional Applications for Oxygen Reduction Reaction and Lithium Ion Batteries,” *Adv. Mater.*, vol. 25, no. 35, pp. 4932–4937, Sep. 2013.
[48] P. A. Denis, “Band gap opening of monolayer and bilayer graphene doped with aluminium, silicon, phosphorus, and sulfur,” *Chem. Phys. Lett.*, vol. 492, no. 4, pp. 251–257, Jun. 2010.
[49] T. B. Martins, R. H. Miwa, A. J. R. da Silva, and A. Fazzio, “Electronic and Transport Properties of Boron-Doped Graphene Nanoribbons,” *Phys. Rev. Lett.*, vol. 98, no. 19, p. 196803, May 2007.

[50] Z.-H. Sheng, H.-L. Gao, W.-J. Bao, F.-B. Wang, and X.-H. Xia, "Synthesis of boron doped graphene for oxygen reduction reaction in fuel cells," *J. Mater. Chem.*, vol. 22, no. 2, pp. 390–395, 2012.
[51] M. Terrones *et al.*, "Efficient route to large arrays of CNx nanofibers by pyrolysis of ferrocene/melamine mixtures," *Appl. Phys. Lett.*, vol. 75, no. 25, pp. 3932–3934, Dec. 1999.
[52] X. Li *et al.*, "Preparation and characterization of graphitic carbon nitride through pyrolysis of melamine," *Appl. Phys. A*, vol. 94, no. 2, pp. 387–392, Feb. 2009.
[53] J. Yang *et al.*, "Synthesis and characterization of nitrogen-rich carbon nitride nanobelts by pyrolysis of melamine," *Appl. Phys. A*, vol. 105, no. 1, p. 161, Oct. 2011.
[54] O. J. A. Schueller, S. T. Brittain, and G. M. Whitesides, "Fabrication of glassy carbon microstructures by pyrolysis of microfabricated polymeric precursors," *Adv. Mater.*, vol. 9, no. 6, pp. 477–480, Jun. 1997.
[55] S. Ranganathan, R. Mccreery, S. M. Majji, and M. Madou, "Photoresist-derived carbon for microelectromechanical systems and electrochemical applications," *J. Electrochem. Soc.*, vol. 147, no. 1, pp. 277–282, 2000.
[56] J. Kim, X. Song, K. Kinoshita, M. Madou, and R. White, "Electrochemical Studies of Carbon Films from Pyrolyzed Photoresist," *J. Electrochem. Soc.*, vol. 145, no. 7, pp. 2314–2319, Jul. 1998.
[57] C. Wang, L. Taherabadi, G. Jia, M. Madou, Y. Yeh, and B. Dunn, "C-MEMS for the Manufacture of 3D Microbatteries," *Electrochem. Solid-State Lett.*, vol. 7, no. 11, pp. A435–A438, Nov. 2004.
[58] M. J. Madou, *Manufacturing Techniques for Microfabrication and Nanotechnology*. CRC Press, 2011.
[59] R. Martinez-Duarte, M. J. Madou, G. Kumar, and J. Schroers, "A novel method for amorphous metal micromolding using Carbon MEMS," in *TRANSDUCERS 2009 - 2009 International Solid-State Sensors, Actuators and Microsystems Conference*, 2009, pp. 188–191.
[60] Y. Wang, L. Pham, G. P. S. de Vasconcellos, and M. Madou, "Fabrication and characterization of micro PEM fuel cells using pyrolyzed carbon current collector plates," *J. Power Sources*, vol. 195, no. 15, pp. 4796–4803, Aug. 2010.
[61] K. Malladi, C. Wang, and M. Madou, "Fabrication of suspended carbon microstructures by e-beam writer and pyrolysis," *Carbon*, vol. 44, no. 13, pp. 2602–2607, Nov. 2006.
[62] S. Y. Chou, P. R. Krauss, and P. J. Renstrom, "Nanoimprint lithography," *J. Vac. Sci. Technol. B Microelectron. Nanometer Struct. Process. Meas. Phenom.*, vol. 14, no. 6, pp. 4129–4133, Nov. 1996.
[63] V. Penmatsa, H. Kawarada, and C. Wang, "Fabrication of carbon nanostructures using photo-nanoimprint lithography and pyrolysis," *J. Micromechanics Microengineering*, vol. 22, no. 4, p. 045024, 2012.
[64] S. Juodkazis, V. Mizeikis, K. K. Seet, M. Miwa, and H. Misawa, "Two-photon lithography of nanorods in SU-8 photoresist," *Nanotechnology*, vol. 16, no. 6, p. 846, 2005.
[65] D. H. Reneker and A. L. Yarin, "Electrospinning jets and polymer nanofibers," *Polymer*, vol. 49, no. 10, pp. 2387–2425, May 2008.
[66] G. Taylor, "Disintegration of water drops in an electric field," in *Proceedings of the Royal Society of London A: Mathematical, Physical and Engineering Sciences of London A: Mathematical, Physical and Engineering Sciences*, 1964, vol. 280, p. 1382.
[67] A. L. Yarin, S. Koombhongse, and D. H. Reneker, "Taylor cone and jetting from liquid droplets in electrospinning of nanofibers," *J. Appl. Phys.*, vol. 90, no. 9, pp. 4836–4846, Nov. 2001.
[68] D. H. Reneker, A. L. Yarin, H. Fong, and S. Koombhongse, "Bending instability of electrically charged liquid jets of polymer solutions in electrospinning," *J. Appl. Phys.*, vol. 87, no. 9, pp. 4531–4547, Apr. 2000.
[69] D. Sun, C. Chang, S. Li, and L. Lin, "Near-Field Electrospinning," *Nano Lett.*, vol. 6, no. 4, pp. 839–842, Apr. 2006.
[70] C. S. Sharma, A. Sharma, and M. Madou, "Multiscale Carbon Structures Fabricated by Direct Micropatterning of Electrospun Mats of SU-8 Photoresist Nanofibers," *Langmuir*, vol. 26, no. 4, pp. 2218–2222, Feb. 2010.
[71] M. Park, J. Im, J. Park, and U. Jeong, "Micropatterned Stretchable Circuit and Strain Sensor Fabricated by Lithography on an Electrospun Nanofiber Mat," *ACS Appl. Mater. Interfaces*, vol. 5, no. 17, pp. 8766–8771, Sep. 2013.
[72] M. Shin, H. Yoshimoto, and J. P. Vacanti, "In Vivo Bone Tissue Engineering Using Mesenchymal Stem Cells on a Novel Electrospun Nanofibrous Scaffold," *Tissue Eng.*, vol. 10, no. 1–2, pp. 33–41, Jan. 2004.
[73] X. Xin, M. Hussain, and J. J. Mao, "Continuing differentiation of human mesenchymal stem cells and induced chondrogenic and osteogenic lineages in electrospun PLGA nanofiber scaffold," *Biomaterials*, vol. 28, no. 2, pp. 316–325, Jan. 2007.

[74] G. Ren *et al.*, “Electrospun poly(vinyl alcohol)/glucose oxidase biocomposite membranes for biosensor applications,” *React. Funct. Polym.*, vol. 66, no. 12, pp. 1559–1564, Dec. 2006.
[75] X. Wang, Y.-G. Kim, C. Drew, B.-C. Ku, J. Kumar, and L. A. Samuelson, “Electrostatic Assembly of Conjugated Polymer Thin Layers on Electrospun Nanofibrous Membranes for Biosensors,” *Nano Lett.*, vol. 4, no. 2, pp. 331–334, Feb. 2004.
[76] A. Hasan *et al.*, “Electrospun scaffolds for tissue engineering of vascular grafts,” *Acta Biomater.*, vol. 10, no. 1, pp. 11–25, Jan. 2014.
[77] J. A. Matthews, G. E. Wnek, D. G. Simpson, and G. L. Bowlin, “Electrospinning of Collagen Nanofibers,” *Biomacromolecules*, vol. 3, no. 2, pp. 232–238, Mar. 2002.
[78] P. Katta, M. Alessandro, R. D. Ramsier, and G. G. Chase, “Continuous Electrospinning of Aligned Polymer Nanofibers onto a Wire Drum Collector,” *Nano Lett.*, vol. 4, no. 11, pp. 2215–2218, Nov. 2004.
[79] H. Pan, L. Li, L. Hu, and X. Cui, “Continuous aligned polymer fibers produced by a modified electrospinning method,” *Polymer*, vol. 47, no. 14, pp. 4901–4904, Jun. 2006.
[80] B. Sundaray, V. Subramanian, T. S. Natarajan, R.-Z. Xiang, C.-C. Chang, and W.-S. Fann, “Electrospinning of continuous aligned polymer fibers,” *Appl. Phys. Lett.*, vol. 84, no. 7, pp. 1222–1224, Feb. 2004.
[81] W. E. Teo and S. Ramakrishna, “A review on electrospinning design and nanofibre assemblies,” *Nanotechnology*, vol. 17, no. 14, p. R89, 2006.
[82] S. Zhao, Q. Zhou, Y.-Z. Long, G.-H. Sun, and Y. Zhang, “Nanofibrous patterns by direct electrospinning of nanofibers onto topographically structured non-conductive substrates,” *Nanoscale*, vol. 5, no. 11, pp. 4993–5000, 2013.
[83] J. M. Deitzel, J. D. Kleinmeyer, J. K. Hirvonen, and N. C. Beck Tan, “Controlled deposition of electrospun poly(ethylene oxide) fibers,” *Polymer*, vol. 42, no. 19, pp. 8163–8170, Sep. 2001.
[84] J. Lee, S. Y. Lee, J. Jang, Y. H. Jeong, and D.-W. Cho, “Fabrication of Patterned Nanofibrous Mats Using Direct-Write Electrospinning,” *Langmuir*, vol. 28, no. 18, pp. 7267–7275, May 2012.
[85] D. Li, Y. Wang, and Y. Xia, “Electrospinning of Polymeric and Ceramic Nanofibers as Uniaxially Aligned Arrays,” *Nano Lett.*, vol. 3, no. 8, pp. 1167–1171, Aug. 2003.
[86] G. Canton, “Development of Electro-Mechanical Spinning for Controlled Deposition of Carbon Nanofibers,” Ph.D., University of California, Irvine, United States -- California, 2014.
[87] Z. H. Liu, C. T. Pan, L. W. Lin, and H. W. Lai, “Piezoelectric properties of PVDF/MWCNT nanofiber using near-field electrospinning,” *Sens. Actuators Phys.*, vol. 193, pp. 13–24, Apr. 2013.
[88] † Il-Doo Kim, * Avner Rothschild, † Byong Hong Lee, † Dong Young Kim, † and Seong Mu Jo, and H. L. Tuller‡, “Ultrasensitive Chemiresistors Based on Electrospun TiO2 Nanofibers,” 28-Jul-2006. [Online]. Available: http://pubs.acs.org/doi/abs/10.1021/nl061197h. [Accessed: 21-Feb-2018].
[89] J. Xu *et al.*, “Accuracy Improvement of Nano-fiber Deposition by Near-Field Electrospinning,” in *IWMF 9th International Workshop on Microfactories*, 2014.
[90] R. E. Franklin, “Crystallite growth in graphitizing and non-graphitizing carbons,” in *Proceedings of the Royal Society of London A: Mathematical, Physical and Engineering Sciences*, 1951, vol. 209, pp. 196–218.
[91] P. J. F. Harris, “Fullerene-like models for microporous carbon,” *J. Mater. Sci.*, vol. 48, no. 2, pp. 565–577, Jan. 2013.
[92] P. J. F. Harris †, “Fullerene-related structure of commercial glassy carbons,” *Philos. Mag.*, vol. 84, no. 29, pp. 3159–3167, Oct. 2004.
[93] J. J. Kipling, J. N. Sherwood, P. V. Shooter, and N. R. Thompson, “Factors influencing the graphitization of polymer carbons,” *Carbon*, vol. 1, no. 3, pp. 315–320, Apr. 1964.
[94] M. Ghazinejad, S. Holmberg, and M. Madou, “Manufacturing carbon nanofiber electrodes with embedded metallic nanoparticles using block copolymers templates,” in *Carbon Nanotubes, Graphene, and Emerging 2D Materials for Electronic and Photonic Devices IX*, 2016, vol. 9932, p. 99320G.
[95] J.-B. Donnet and R. C. Bansal, *Carbon Fibers, Third Edition,*. CRC Press, 1998.
[96] V. Madhavi and S. S. Lele, “Laccase: properties and applications,” *Bioresources*, vol. 4, no. 4, pp. 1694–1717, 2009.
[97] O. V. Morozova, G. P. Shumakovich, M. A. Gorbacheva, S. V. Shleev, and A. I. Yaropolov, “‘Blue’ laccases,” *Biochem. Mosc.*, vol. 72, no. 10, pp. 1136–1150, 2007.
[98] A. I. Yaropolov, O. V. Skorobogat’Ko, S. S. Vartanov, and S. D. Varfolomeyev, “Laccase,” *Appl. Biochem. Biotechnol.*, vol. 49, no. 3, pp. 257–280, 1994.
[99] A. M. Mayer and R. C. Staples, “Laccase: new functions for an old enzyme,” *Phytochemistry*, vol. 60, no. 6, pp. 551–565, 2002.

[100] D. L. Johnson, J. L. Thompson, S. M. Brinkmann, K. A. Schuller, and L. L. Martin, "Electrochemical characterization of purified Rhus vernicifera laccase: voltammetric evidence for a sequential four-electron transfer," *Biochemistry (Mosc.)*, vol. 42, no. 34, pp. 10229–10237, 2003.
[101] D. Ivnitski and P. Atanassov, "Electrochemical Studies of Intramolecular Electron Transfer in Laccase from Trametes versicolor," *Electroanalysis*, vol. 19, no. 22, pp. 2307–2313, Nov. 2007.
[102] A. Le Goff, M. Holzinger, and S. Cosnier, "Recent progress in oxygen-reducing laccase biocathodes for enzymatic biofuel cells," *Cell. Mol. Life Sci.*, vol. 72, no. 5, pp. 941–952, Jan. 2015.
[103] W. Zheng, Q. Li, L. Su, Y. Yan, J. Zhang, and L. Mao, "Direct Electrochemistry of Multi-Copper Oxidases at Carbon Nanotubes Noncovalently Functionalized with Cellulose Derivatives," *Electroanalysis*, vol. 18, pp. 587–594, 2006.
[104] Y. Yan, W. Zheng, L. Su, and L. Mao, "Carbon-Nanotube-Based Glucose/O2 Biofuel Cells," *Adv. Mater.*, vol. 18, pp. 2639–2643, 2006.
[105] C. F. Blanford, R. S. Heath, and F. A. Armstrong, "A stable electrode for high-potential, electrocatalytic O2 reduction based on rational attachment of a blue copper oxidase to a graphite surface," *Chem. Commun.*, no. 17, p. 1710, 2007.
[106] M. S. Thorum *et al.*, "Direct, Electrocatalytic Oxygen Reduction by Laccase on Anthracene-2-methanethiol-Modified Gold," *J. Phys. Chem. Lett.*, vol. 1, no. 15, pp. 2251–2254, Aug. 2010.
[107] M. Sosna, J.-M. Chrétien, J. D. Kilburn, and P. N. Bartlett, "Monolayer anthracene and anthraquinone modified electrodes as platforms for Trametes hirsuta laccase immobilisation.," *Phys. Chem. Chem. Phys. PCCP*, vol. 12, no. 34, pp. 10018–26, Sep. 2010.
[108] W. Gellett, J. Schumacher, M. Kesmez, D. Le, and S. D. Minteer, "High Current Density Air-Breathing Laccase Biocathode," *J. Electrochem. Soc.*, vol. 157, no. 4, pp. B557–B562, Apr. 2010.
[109] M. T. Meredith, M. Minson, D. Hickey, K. Artyushkova, D. T. Glatzhofer, and S. D. Minteer, "Anthracene-Modified Multi-Walled Carbon Nanotubes as Direct Electron Transfer Scaffolds for Enzymatic Oxygen Reduction," *ACS Catal.*, vol. 1, no. 12, pp. 1683–1690, Dec. 2011.
[110] R. D. Milton, F. Giroud, A. E. Thumser, S. D. Minteer, and R. C. T. Slade, "Hydrogen peroxide produced by glucose oxidase affects the performance of laccase cathodes in glucose/oxygen fuel cells: FAD-dependent glucose dehydrogenase as a replacement," *Phys. Chem. Chem. Phys.*, vol. 15, no. 44, p. 19371, 2013.
[111] F. Giroud and S. D. Minteer, "Anthracene-modified pyrenes immobilized on carbon nanotubes for direct electroreduction of O2 by laccase," *Electrochem. Commun.*, vol. 34, pp. 157–160, Sep. 2013.
[112] M. T. Meredith and S. D. Minteer, "Biofuel Cells: Enhanced Enzymatic Bioelectrocatalysis," *Annu. Rev. Anal. Chem.*, vol. 5, no. 1, pp. 157–179, 2012.
[113] P. Scodeller, R. Carballo, R. Szamocki, L. Levin, F. Forchiassin, and E. J. Calvo, "Layer-by-Layer Self-Assembled Osmium Polymer-Mediated Laccase Oxygen Cathodes for Biofuel Cells: The Role of Hydrogen Peroxide," *J. Am. Chem. Soc.*, vol. 132, no. 32, pp. 11132–11140, Aug. 2010.
[114] R. D. Milton, F. Giroud, A. E. Thumser, S. D. Minteer, and R. C. T. Slade, "Bilirubin oxidase bioelectrocatalytic cathodes: the impact of hydrogen peroxide," *Chem Commun*, vol. 50, no. 1, pp. 94–96, 2014.
[115] A. Zebda, C. Gondran, A. Le Goff, M. Holzinger, P. Cinquin, and S. Cosnier, "Mediatorless high-power glucose biofuel cells based on compressed carbon nanotube-enzyme electrodes," *Nat. Commun.*, vol. 2, p. 370, Jun. 2011.
[116] J. Jordaan and W. D. Leukes, "Isolation of a thermostable laccase with DMAB and MBTH oxidative coupling activity from a mesophilic white rot fungus," *Enzyme Microb. Technol.*, vol. 33, no. 2–3, pp. 212–219, Aug. 2003.
[117] D. D'Souza-Ticlo, D. Sharma, and C. Raghukumar, "A thermostable metal-tolerant laccase with bioremediation potential from a marine-derived fungus," *Mar. Biotechnol.*, vol. 11, no. 6, pp. 725–737, 2009.
[118] F. J. Enguita, L. O. Martins, A. O. Henriques, and M. A. Carrondo, "Crystal structure of a bacterial endospore coat component a laccase with enhanced thermostability properties," *J. Biol. Chem.*, vol. 278, no. 21, pp. 19416–19425, 2003.
[119] L. I. Ramírez-Cavazos *et al.*, "Enhanced production of thermostable laccases from a native strain of Pycnoporus sanguineus using central composite design," *J. Zhejiang Univ. Sci. B*, vol. 15, no. 4, pp. 343–352, Apr. 2014.
[120] L. I. Ramírez-Cavazos *et al.*, "Purification and Characterization of two thermostable laccases from Pycnoporus sanguineus and potential role in degradation of Endocrine Disrupting Chemicals," *J Mol Catal B Enzym*, vol. 104, pp. 32–42, 2014.

[121] L. Halámková, J. Halámek, V. Bocharova, A. Szczupak, L. Alfonta, and E. Katz, "Implanted biofuel cell operating in a living snail," *J. Am. Chem. Soc.*, vol. 134, no. 11, pp. 5040–5043, 2012.
[122] S. Cosnier, A. Le Goff, and M. Holzinger, "Towards glucose biofuel cells implanted in human body for powering artificial organs: Review," *Electrochem. Commun.*, vol. 38, pp. 19–23, Jan. 2014.
[123] S. Aquino Neto and A. R. De Andrade, "New energy sources: the enzymatic biofuel cell," *J. Braz. Chem. Soc.*, vol. 24, no. 12, pp. 1891–1912, 2013.
[124] V. Coman *et al.*, "A Direct Electron Transfer-Based Glucose/Oxygen Biofuel Cell Operating in Human Serum," *Fuel Cells*, vol. 10, no. 1, pp. 9–16, 2010.
[125] X. Wang *et al.*, "Mediatorless sugar/oxygen enzymatic fuel cells based on gold nanoparticle-modified electrodes," *Biosens. Bioelectron.*, vol. 31, no. 1, pp. 219–225, 2012.
[126] M. Rasmussen, R. E. Ritzmann, I. Lee, A. J. Pollack, and D. Scherson, "An implantable biofuel cell for a live insect," *J. Am. Chem. Soc.*, vol. 134, no. 3, pp. 1458–1460, 2012.
[127] C. Eggert, U. Temp, and K. L. Eriksson, "The Ligninolytic System of the White Rot Fungus Pycnoporus cinnabarinus : Purification and Characterization of the Laccase," *Appl. Environ. Microbiol.*, vol. 62, no. 4, pp. 1151–1158, 1996.
[128] S. Holmberg *et al.*, "Bioelectrochemical study of thermostable Pycnoporus sanguineus CS43 laccase bioelectrodes based on pyrolytic carbon nanofibers for bioelectrocatalytic O2 reduction," *ACS Catal.*, vol. 5, no. 12, pp. 7507–7518, 2015.
[129] R. C. Minussi *et al.*, "Purification, characterization and application of laccase from Trametes versicolor for colour and phenolic removal of olive mill wastewater in the presence of 1- hydroxybenzotriazole," *Afr. J. Biotechnol.*, vol. 6, no. 10, 2007.
[130] M. Han, H. Choi, and H. Song, "Purification and characterization of laccase from the white rot fungus Trametes versicolor," *J. Microbiol.-SEOUL-*, vol. 43, no. 6, p. 555, 2005.
[131] J. Krejci *et al.*, "Effective Surface Area of Electrochemical Sensors," *J. Electrochem. Soc.*, vol. 161, no. 6, pp. B147–B150, 2014.
[132] M. Pita *et al.*, "High redox potential cathode based on laccase covalently attached to gold electrode," *J. Phys. Chem. C*, vol. 115, pp. 13420–13428, 2011.
[133] S. C. Barton, J. Gallaway, and P. Atanassov, "Enzymatic biofuel cells for implantable and microscale devices," *Chem. Rev.*, vol. 104, pp. 4867–4886, 2004.
[134] C. Gutiérrez-Sánchez *et al.*, "Enhanced direct electron transfer between laccase and hierarchical carbon microfibers/carbon nanotubes composite electrodes. Comparison of three enzyme immobilization methods," *Electrochimica Acta*, vol. 82, pp. 218–223, 2012.
[135] W. Jia *et al.*, "Towards a high potential biocathode based on direct bioelectrochemistry between horseradish peroxidase and hierarchically structured carbon nanotubes," *Phys. Chem. Chem. Phys.*, vol. 12, pp. 10088–10092, 2010.
[136] A. G. Pandolfo and A. F. Hollenkamp, "Carbon properties and their role in supercapacitors," *J. Power Sources*, vol. 157, pp. 11–27, 2006.
[137] R. D. Milton and S. D. Minteer, "Investigating the Reversible Inhibition Model of Laccase by Hydrogen Peroxide for Bioelectrocatalytic Applications," *J. Electrochem. Soc.*, vol. 161, no. 13, pp. H3011–H3014, Sep. 2014.
[138] A. Naqui and S. D. Varfolomeev, "Inhibition mechanism of Polyporus laccase by fluoride ion," *FEBS Lett.*, vol. 113, no. 2, pp. 157–160, 1980.
[139] U. Salaj-Kosla, S. Pöller, W. Schuhmann, S. Shleev, and E. Magner, "Direct electron transfer of Trametes hirsuta laccase adsorbed at unmodified nanoporous gold electrodes.," *Bioelectrochemistry Amst. Neth.*, vol. 91, pp. 15–20, Jun. 2013.
[140] H. P. Call and I. Mücke, "History, overview and applications of mediated lignolytic systems, especially laccase-mediator-systems (Lignozym®-process)," *J. Biotechnol. 532 1997*, vol. 53, pp. 163–202, 1997.
[141] H. Hou and D. H. Reneker, "Carbon Nanotubes on Carbon Nanofibers: A Novel Structure Based on Electrospun Polymer Nanofibers," *Adv. Mater.*, vol. 16, no. 1, pp. 69–73, Jan. 2004.
[142] Y. Liu, H. Teng, H. Hou, and T. You, "Nonenzymatic glucose sensor based on renewable electrospun Ni nanoparticle-loaded carbon nanofiber paste electrode," *Biosens. Bioelectron.*, vol. 24, no. 11, pp. 3329–3334, 2009.
[143] Q. Guo *et al.*, "Supercapacitors based on hybrid carbon nanofibers containing multiwalled carbon nanotubes," *J. Mater. Chem.*, vol. 19, no. 18, pp. 2810–2816, 2009.

[144] P. Santhosh, K. M. Manesh, S. Uthayakumar, S. Komathi, A. I. Gopalan, and K.-P. Lee, "Fabrication of enzymatic glucose biosensor based on palladium nanoparticles dispersed onto poly (3, 4-ethylenedioxythiophene) nanofibers," *Bioelectrochemistry*, vol. 75, no. 1, pp. 61–66, 2009.
[145] J. Huang, Y. Liu, H. Hou, and T. You, "Simultaneous electrochemical determination of dopamine, uric acid and ascorbic acid using palladium nanoparticle-loaded carbon nanofibers modified electrode," *Biosens. Bioelectron.*, vol. 24, no. 4, pp. 632–637, 2008.
[146] S. Park *et al.*, "Macroscopic 10-terabit–per–square-inch arrays from block copolymers with lateral order," *Science*, vol. 323, no. 5917, pp. 1030–1033, 2009.
[147] G. Kästle *et al.*, "Micellar nanoreactors—Preparation and characterization of hexagonally ordered arrays of metallic nanodots," *Adv. Funct. Mater.*, vol. 13, no. 11, pp. 853–861, 2003.
[148] A. J. Bard and L. R. Faulkner, *Electrochemical Methods: Fundamentals and Applications*. Wiley, 2000.
[149] R.L. McCreery, "Advanced carbon electrode materials for molecular electrochemistry," *Chem. Rev.*, vol. 108, no. 7, pp. 2646–2687, 2008.
[150] C. E. Banks and R. G. Compton, "New electrodes for old: from carbon nanotubes to edge plane pyrolytic graphite," *Analyst*, vol. 131, no. 1, pp. 15–21, 2006.
[151] R. S. Nicholson, "Theory and Application of Cyclic Voltammetry for Measurement of Electrode Reaction Kinetics.," *Anal. Chem.*, vol. 37, no. 11, pp. 1351–1355, Oct. 1965.
[152] S. J. Konopka and B. McDuffie, "Diffusion coefficients of ferri- and ferrocyanide ions in aqueous media, using twin-electrode thin-layer electrochemistry," *Anal. Chem.*, vol. 42, no. 14, pp. 1741–1746, 1970.
[153] J. Doshi and D. H. Reneker, "Electrospinning process and applications of electrospun fibers," *J. Electrost.*, vol. 35, no. 2, pp. 151–160, Aug. 1995.
[154] S. D. Mohan, G. R. Mitchell, and F. J. Davis, "Chain extension in electrospun polystyrene fibres: a SANS study," *Soft Matter*, vol. 7, no. 9, pp. 4397–4404, 2011.
[155] Y. Ji *et al.*, "Confinement-induced super strong PS/MWNT composite nanofibers," *EPL Europhys. Lett.*, vol. 84, no. 5, p. 56002, Dec. 2008.
[156] A. Arinstein, "Confinement mechanism of electrospun polymer nanofiber reinforcement," *J. Polym. Sci. Part B Polym. Phys.*, vol. 51, no. 9, pp. 756–763, May 2013.
[157] H. A. Pohl, "The Motion and Precipitation of Suspensoids in Divergent Electric Fields," *J. Appl. Phys.*, vol. 22, no. 7, pp. 869–871, Jul. 1951.
[158] C. Wei, T.-Y. Wei, C.-H. Liang, and F.-C. Tai, "The separation of different conducting multi-walled carbon nanotubes by AC dielectrophoresis," *Diam. Relat. Mater.*, vol. 18, no. 2–3, pp. 332–336, Feb. 2009.
[159] M. S. A. Rahaman, A. F. Ismail, and A. Mustafa, "A review of heat treatment on polyacrylonitrile fiber," *Polym. Degrad. Stab.*, vol. 92, no. 8, pp. 1421–1432, Aug. 2007.
[160] S. Dalton, F. Heatley, and P. M. Budd, "Thermal stabilization of polyacrylonitrile fibres," *Polymer*, vol. 40, no. 20, pp. 5531–5543, Sep. 1999.
[161] A. Gupta and I. R. Harrison, "New aspects in the oxidative stabilization of PAN-based carbon fibers: II," *Carbon*, vol. 35, no. 6, pp. 809–818, 1997.
[162] H. G. Chae, M. L. Minus, A. Rasheed, and S. Kumar, "Stabilization and carbonization of gel spun polyacrylonitrile/single wall carbon nanotube composite fibers," *Polymer*, vol. 48, no. 13, pp. 3781–3789, Jun. 2007.
[163] A. C. Ferrari and D. M. Basko, "Raman spectroscopy as a versatile tool for studying the properties of graphene," *Nat. Nanotechnol.*, vol. 8, no. 4, pp. 235–246, Apr. 2013.
[164] A. C. Ferrari and J. Robertson, "Interpretation of Raman spectra of disordered and amorphous carbon," *Phys. Rev. B*, vol. 61, no. 20, pp. 14095–14107, May 2000.
[165] A. C. Ferrari, "Raman spectroscopy of graphene and graphite: Disorder, electron–phonon coupling, doping and nonadiabatic effects," *Solid State Commun.*, vol. 143, no. 1, pp. 47–57, Jul. 2007.
[166] C. Casiraghi *et al.*, "Raman Spectroscopy of Graphene Edges," *Nano Lett.*, vol. 9, no. 4, pp. 1433–1441, Apr. 2009.
[167] J. Sandler *et al.*, "Variations in the Raman peak shift as a function of hydrostatic pressure for various carbon nanostructures: A simple geometric effect," *Phys. Rev. B*, vol. 67, no. 3, p. 035417, Jan. 2003.
[168] E. J. Ra, K. H. An, K. K. Kim, S. Y. Jeong, and Y. H. Lee, "Anisotropic electrical conductivity of MWCNT/PAN nanofiber paper," *Chem. Phys. Lett.*, vol. 413, no. 1–3, pp. 188–193, Sep. 2005.
[169] I.-H. Chen, C.-C. Wang, and C.-Y. Chen, "Fabrication and characterization of magnetic cobalt ferrite/polyacrylonitrile and cobalt ferrite/carbon nanofibers by electrospinning," *Carbon*, vol. 48, no. 3, pp. 604–611, Mar. 2010.

[170] R. L. Vander Wal, A. J. Tomasek, M. I. Pamphlet, C. D. Taylor, and W. K. Thompson, "Analysis of HRTEM images for carbon nanostructure quantification," *J. Nanoparticle Res.*, vol. 6, no. 6, pp. 555–568, Dec. 2004.
[171] D. A. C. Brownson and C. E. Banks, "Interpreting Electrochemistry," in *The Handbook of Graphene Electrochemistry*, London: Springer London, 2014, pp. 23–77.
[172] K. K. Cline, M. T. McDermott, R. L. McCreery, and others, "Anomalously slow electron transfer at ordered graphite electrodes: influence of electronic factors and reactive sites," *J. Phys. Chem.*, vol. 98, no. 20, pp. 5314–5319, 1994.
[173] R. G. Compton, E. Laborda, and K. R. Ward, *Understanding voltammetry: simulation of electrode processes*. World Scientific, 2013.
[174] M. Pumera, T. Sasaki, and H. Iwai, "Relationship between Carbon Nanotube Structure and Electrochemical Behavior: Heterogeneous Electron Transfer at Electrochemically Activated Carbon Nanotubes," *Chem. – Asian J.*, vol. 3, no. 12, pp. 2046–2055, Dec. 2008.
[175] I. Dumitrescu, P. R. Unwin, and J. V. Macpherson, "Electrochemistry at carbon nanotubes : perspective and issues," *Chem. Commun.*, vol. 0, no. 45, pp. 6886–6901, 2009.
[176] M. Velický *et al.*, "Electron Transfer Kinetics on Mono- and Multilayer Graphene," *ACS Nano*, vol. 8, no. 10, pp. 10089–10100, Oct. 2014.
[177] S. Boopathi, T. N. Narayanan, and S. S. Kumar, "Improved heterogeneous electron transfer kinetics of fluorinated graphene derivatives," *Nanoscale*, vol. 6, no. 17, pp. 10140–10146, 2014.
[178] P. Chen and R. L. McCreery, "Control of electron transfer kinetics at glassy carbon electrodes by specific surface modification," *Anal. Chem.*, vol. 68, no. 22, pp. 3958–3965, 1996.
[179] C. Wang, R. Zaouk, B. Y. Park, and M. J. Madou, "Carbon as a MEMS material: micro and nanofabrication of pyrolysed photoresist carbon," *Int. J. Manuf. Technol. Manag.*, vol. 13, no. 2, pp. 360–375, Jan. 2008.
[180] O. J. A. Schueller, S. T. Brittain, C. Marzolin, and G. M. Whitesides, "Fabrication and Characterization of Glassy Carbon MEMS," *Chem. Mater.*, vol. 9, no. 6, pp. 1399–1406, 1997.
[181] R. Antiochia, I. Lavagnini, F. Magno, F. Valentini, and G. Palleschi, "Single-Wall Carbon Nanotube Paste Electrodes: a Comparison with Carbon Paste, Platinum and Glassy Carbon Electrodes via Cyclic Voltammetric Data," *Electroanalysis*, vol. 16, no. 17, pp. 1451–1458, Sep. 2004.
[182] A. T. Valota *et al.*, "Electrochemical behavior of monolayer and bilayer graphene," *ACS Nano*, vol. 5, no. 11, pp. 8809–8815, 2011.
[183] T. Xing *et al.*, "Observation of Active Sites for Oxygen Reduction Reaction on Nitrogen-Doped Multilayer Graphene," *ACS Nano*, vol. 8, no. 7, pp. 6856–6862, Jul. 2014.
[184] X. Ji, C. E. Banks, A. Crossley, and R. G. Compton, "Oxygenated Edge Plane Sites Slow the Electron Transfer of the Ferro-/Ferricyanide Redox Couple at Graphite Electrodes," *ChemPhysChem*, vol. 7, no. 6, pp. 1337–1344, Jun. 2006.
[185] M. L. A. V. Heien, P. E. M. Phillips, G. D. Stuber, A. T. Seipel, and R. Mark Wightman, "Overoxidation of carbon-fiber microelectrodes enhances dopamine adsorption and increases sensitivity," *Analyst*, vol. 128, no. 12, pp. 1413–1419, 2003.
[186] J. Li and B. M. Christensen, "Effect of pH on the oxidation pathway of dopamine and dopa," *J. Electroanal. Chem.*, vol. 375, no. 1, pp. 219–231, Sep. 1994.
[187] C. D. Allred and R. L. McCreery, "Adsorption of catechols on fractured glassy carbon electrode surfaces," *Anal. Chem.*, vol. 64, no. 4, pp. 444–448, Feb. 1992.
[188] M. Megawati, C. Kiang Chua, Z. Sofer, K. Klímová, and M. Pumera, "Nitrogen-doped graphene: effect of graphite oxide precursors and nitrogen content on the electrochemical sensing properties," *Phys. Chem. Chem. Phys.*, vol. 19, no. 24, pp. 15914–15923, 2017.
[189] Z.-H. Sheng, X.-Q. Zheng, J.-Y. Xu, W.-J. Bao, F.-B. Wang, and X.-H. Xia, "Electrochemical sensor based on nitrogen doped graphene: Simultaneous determination of ascorbic acid, dopamine and uric acid," *Biosens. Bioelectron.*, vol. 34, no. 1, pp. 125–131, Apr. 2012.
[190] K. Sudhakara Prasad, G. Muthuraman, and J.-M. Zen, "The role of oxygen functionalities and edge plane sites on screen-printed carbon electrodes for simultaneous determination of dopamine, uric acid and ascorbic acid," *Electrochem. Commun.*, vol. 10, no. 4, pp. 559–563, Apr. 2008.
[191] L. Tang, Y. Wang, Y. Li, H. Feng, J. Lu, and J. Li, "Preparation, Structure, and Electrochemical Properties of Reduced Graphene Sheet Films," *Adv. Funct. Mater.*, vol. 19, no. 17, pp. 2782–2789, Sep. 2009.
[192] K. S. Chen, M. A. Hickner, and D. R. Noble, "Simplified models for predicting the onset of liquid water droplet instability at the gas diffusion layer/gas flow channel interface," *Int. J. Energy Res.*, vol. 29, no. 12, pp. 1113–1132, Oct. 2005.

[193] N. G. Shang *et al.*, "Catalyst-Free Efficient Growth, Orientation and Biosensing Properties of Multilayer Graphene Nanoflake Films with Sharp Edge Planes," *Adv. Funct. Mater.*, vol. 18, no. 21, pp. 3506–3514, Nov. 2008.
[194] M. Sajid, M. K. Nazal, M. Mansha, A. Alsharaa, S. M. S. Jillani, and C. Basheer, "Chemically modified electrodes for electrochemical detection of dopamine in the presence of uric acid and ascorbic acid: A review," *TrAC Trends Anal. Chem.*, vol. 76, pp. 15–29, Feb. 2016.
[195] P. Kissinger and W. R. Heineman, *Laboratory Techniques in Electroanalytical Chemistry, Second Edition, Revised and Expanded*. CRC Press, 1996.
[196] X. Mao, X. Yang, G. C. Rutledge, and T. Alan Hatton, "Ultra-Wide-Range Electrochemical Sensing Using Continuous Electrospun Carbon Nanofibers with High Densities of States," *ACS Appl. Mater. Interfaces*, vol. 6, no. 5, pp. 3394–3405, Mar. 2014.
[197] S. Hanaoka, J. M. Lin, and M. Yamada, "Chemiluminescent flow sensor for H2O2 based on the decomposition of H2O2 catalyzed by cobalt(II)-ethanolamine complex immobilized on resin," *Anal. Chim. Acta*, vol. 426, no. 1, pp. 57–64, 2001.
[198] A. Gomes, E. Fernandes, and J. L. F. C. Lima, "Fluorescence probes used for detection of reactive oxygen species," *J. Biochem. Biophys. Methods*, vol. 65, no. 2–3, pp. 45–80, 2005.
[199] S. Watabe, Y. Sakamoto, M. Morikawa, R. Okada, T. Miura, and E. Ito, "Highly sensitive determination of hydrogen peroxide and glucose by fluorescence correlation spectroscopy," *PLoS ONE*, vol. 6, no. 8, pp. 1–5, 2011.
[200] H. Tian, L. Wang, Z. Sofer, M. Pumera, and A. Bonanni, "Doped Graphene for DNA Analysis: the Electrochemical Signal is Strongly Influenced by the Kind of Dopant and the Nucleobase Structure," *Sci. Rep.*, vol. 6, no. August, p. 33046, 2016.
[201] Y. Zhang *et al.*, "Manageable N-doped graphene for high performance oxygen reduction reaction.," *Sci. Rep.*, vol. 3, p. 2771, 2013.
[202] D. Geng *et al.*, "High oxygen-reduction activity and durability of nitrogen-doped graphene," *Energy Environ. Sci.*, vol. 4, no. 3, p. 760, 2011.
[203] J. M. Campos-Martin, G. Blanco-Brieva, and J. L. G. Fierro, "Hydrogen peroxide synthesis: An outlook beyond the anthraquinone process," *Angew. Chem. - Int. Ed.*, vol. 45, no. 42, pp. 6962–6984, 2006.
[204] M. Yang, F. Qu, Y. Lu, Y. He, G. Shen, and R. Yu, "Platinum nanowire nanoelectrode array for the fabrication of biosensors," *Biomaterials*, vol. 27, no. 35, pp. 5944–5950, 2006.
[205] X. Gao *et al.*, "Single Crystal Sub-Nanometer Sized $Cu_6(SR)_6$ Clusters: Structure, Photophysical Properties, and Electrochemical Sensing," *Adv. Sci.*, vol. 3, no. 12, p. 1600126, 2016.
[206] J. Ju and W. Chen, "In situ growth of surfactant-free gold nanoparticles on nitrogen-doped graphene quantum dots for electrochemical detection of hydrogen peroxide in biological environments," *Anal. Chem.*, vol. 87, no. 3, pp. 1903–1910, 2015.
[207] B. Bin Jiang *et al.*, "A non-enzymatic hydrogen peroxide sensor based on a glassy carbon electrode modified with cuprous oxide and nitrogen-doped graphene in a nafion matrix," *Microchim. Acta*, vol. 181, no. 11–12, pp. 1463–1470, 2014.
[208] X. Wang, G. Sun, P. Routh, D.-H. Kim, W. Huang, and P. Chen, "Heteroatom-doped graphene materials: syntheses, properties and applications," *Chem Soc Rev*, vol. 43, no. 20, pp. 7067–7098, 2014.
[209] C. Zhang, L. Li, J. Ju, and W. Chen, "Electrochemical sensor based on graphene-supported tin oxide nanoclusters for nonenzymatic detection of hydrogen peroxide," *Electrochimica Acta*, vol. 210, pp. 181–189, 2016.
[210] R. Zhang and W. Chen, "Fe3C-functionalized 3D nitrogen-doped carbon structures for electrochemical detection of hydrogen peroxide," *Sci. Bull.*, vol. 60, no. 5, pp. 522–531, 2015.
[211] R. Zhang and W. Chen, "Recent advances in graphene-based nanomaterials for fabricating electrochemical hydrogen peroxide sensors," *Biosens. Bioelectron.*, vol. 89, pp. 249–268, 2016.
[212] W. Chen, S. Cai, Q.-Q. Ren, W. Wen, and Y.-D. Zhao, "Recent advances in electrochemical sensing for hydrogen peroxide: a review," *The Analyst*, vol. 137, no. 1, p. 49, 2012.
[213] S. N. Faisal *et al.*, "Pyridinic and graphitic nitrogen-rich graphene for high-performance supercapacitors and metal-free bifunctional electrocatalysts for ORR and OER," *RSC Adv*, vol. 7, no. 29, pp. 17950–17958, 2017.
[214] M. Liu, S. He, and W. Chen, "Co3O4 nanowires supported on 3D N-doped carbon foam as an electrochemical sensing platform for efficient H2O2 detection," *Nanoscale*, vol. 6, no. 20, pp. 11769–11776, 2014.

[215] S. J. He, B. Y. Zhang, M. M. Liu, and W. Chen, “Non-enzymatic hydrogen peroxide electrochemical sensor based on a three-dimensional MnO2 nanosheets/carbon foam composite,” *Rsc Adv.*, vol. 4, no. 90, pp. 49315–49323, 2014.
[216] M. Liu, R. Liu, and W. Chen, “Graphene wrapped Cu2O nanocubes: Non-enzymatic electrochemical sensors for the detection of glucose and hydrogen peroxide with enhanced stability,” *Biosens. Bioelectron.*, vol. 45, no. 1, pp. 206–212, 2013.
[217] Y. Shao *et al.*, “Nitrogen-doped graphene and its electrochemical applications,” *J. Mater. Chem.*, vol. 20, no. 35, p. 7491, 2010.
[218] Z.-H. Sheng, X.-Q. Zheng, J.-Y. Xu, W.-J. Bao, F.-B. Wang, and X.-H. Xia, “Electrochemical sensor based on nitrogen doped graphene: Simultaneous determination of ascorbic acid, dopamine and uric acid,” *Biosens. Bioelectron.*, vol. 34, no. 1, pp. 125–131, 2012.
[219] R. Yadav and C. K. Dixit, “Synthesis, characterization and prospective applications of nitrogen-doped graphene: A short review,” *J. Sci. Adv. Mater. Devices*, vol. 2, no. 2, pp. 141–149, 2017.
[220] H. Wang, T. Maiyalagan, and X. Wang, “Review on recent progress in nitrogen-doped graphene: Synthesis, characterization, and its potential applications,” *ACS Catal.*, vol. 2, no. 5, pp. 781–794, 2012.
[221] Y. Wang, Y. Shao, D. W. Matson, J. Li, and Y. Lin, “Nitrogen-Doped Graphene and Its Biosensing,” *ACS Nano*, vol. 4, no. 4, pp. 1790–1798, 2010.
[222] J. Zhu *et al.*, “Nitrogen-doped carbon nanofibers derived from polyacrylonitrile for use as anode material in sodium-ion batteries,” *Carbon*, vol. 94, pp. 189–195, 2015.
[223] A. M. Stortini, L. M. Moretto, A. Mardegan, M. Ongaro, and P. Ugo, “Arrays of copper nanowire electrodes: Preparation, characterization and application as nitrate sensor,” *Sens. Actuators B Chem.*, vol. 207, no. Part A, pp. 186–192, 2015.
[224] P. Wu, P. Du, H. Zhang, and C. X. Cai, “Microscopic effects of the bonding configuration of nitrogen-doped graphene on its reactivity toward hydrogen peroxide reduction reaction,” *Phys. Chem. Chem. Phys.*, vol. 15, pp. 6920–6928, 2013.
[225] L. Cheng, X.-L. Li, H.-J. Liu, H.-M. Xiong, and P.-W. Zhang, “Carbon-Coated Li 4 Ti 5 O 12 as a High Rate Electrode Material for Li-Ion Intercalation,” pp. 692–697, 2007.
[226] Y. Wang, Y. Shao, D. W. Matson, J. Li, and Y. Lin, “Nitrogen-Doped Graphene and Its Biosensing,” *ACS Nano*, vol. 4, no. 4, pp. 1790–1798, 2010.
[227] B. Pollack, S. Holmberg, D. George, I. Tran, M. Madou, and M. Ghazinejad, “Nitrogen-Rich Polyacrylonitrile-Based Graphitic Carbons for Hydrogen Peroxide Sensing,” *Sensors*, vol. 17, no. 10, p. 2407, Oct. 2017.
[228] X. Mao, X. Yang, G. C. Rutledge, and T. A. Hatton, “Ultrawide-range electrochemical sensing using continuous electrospun carbon nanofibers with high densities of states - Supporting Information.”
[229] X. Xu, S. Jiang, Z. Hu, and S. Liu, “Nitrogen-doped carbon nanotubes: high electrocatalytic activity toward the oxidation of hydrogen peroxide and its application for biosensing,” *ACS Nano*, vol. 4, no. 7, pp. 4292–4298, 2010.
[230] F. Xu, M. Deng, G. Li, S. Chen, and L. Wang, “Electrochemical behavior of cuprous oxide-reduced graphene oxide nanocomposites and their application in nonenzymatic hydrogen peroxide sensing,” *Electrochimica Acta*, vol. 88, pp. 59–65, 2013.
[231] L. Shi, X. Niu, T. Liu, H. Zhao, and M. Lan, “Electrocatalytic sensing of hydrogen peroxide using a screen printed carbon electrode modified with nitrogen-doped graphene nanoribbons,” *Microchim. Acta*, vol. 182, no. 15–16, pp. 2485–2493, 2015.
[232] V. Penmatsa, H. Kawarada, and C. Wang, “Fabrication of carbon nanostructures using photo-nanoimprint lithography and pyrolysis,” *J. Micromechanics Microengineering*, vol. 22, no. 4, p. 045024, 2012.
[233] V. Madhavi and S. S. Lele, “LACCASE: PROPERTIES AND APPLICATIONS,” *BioResources*, vol. 4, no. 4, pp. 1694–1717, Aug. 2009.
[234] O. V. Morozova, G. P. Shumakovich, S. V. Shleev, and Y. I. Yaropolov, “Laccase-mediator systems and their applications: A review,” *Appl. Biochem. Microbiol.*, vol. 43, no. 5, pp. 523–535, Sep. 2007.
[235] A. I. Yaropolov, O. V. Skorobogat’Ko, S. S. Vartanov, and S. D. Varfolomeyev, “Laccase,” *Appl. Biochem. Biotechnol.*, vol. 49, no. 3, pp. 257–280, 1994.
[236] A. M. Mayer and R. C. Staples, “Laccase: new functions for an old enzyme,” *Phytochemistry*, vol. 60, no. 6, pp. 551–565, 2002.
[237] M. Orlikowska *et al.*, “Structural studies of two thermostable laccases from the white-rot fungus Pycnoporus sanguineus,” *Int. J. Biol. Macromol.*, 2017.

[238] A. A. Voityuk, “Long-range electron transfer in biomolecules. Tunneling or hopping?,” *J. Phys. Chem. B*, vol. 115, no. 42, pp. 12202–12207, 2011.
[239] C. C. Page, C. C. Moser, X. Chen, and P. L. Dutton, “Natural engineering principles of electron tunnelling in biological oxidation–reduction,” *Nature*, vol. 402, no. 6757, p. 47, 1999.
[240] N. Lalaoui *et al.*, “Direct electron transfer between a site-specific pyrene-modified laccase and carbon nanotube/gold nanoparticle supramolecular assemblies for bioelectrocatalytic dioxygen reduction,” *Acs Catal.*, vol. 6, no. 3, pp. 1894–1900, 2016.
[241] M. S. Thorum *et al.*, “Direct, Electrocatalytic Oxygen Reduction by Laccase on Anthracene-2-methanethiol-Modified Gold,” *J. Phys. Chem. Lett.*, vol. 1, no. 15, pp. 2251–2254, Aug. 2010.
[242] F. Wu, L. Su, P. Yu, and L. Mao, “Role of organic solvents in immobilizing fungus laccase on single-walled carbon nanotubes for improved current response in direct bioelectrocatalysis,” *J. Am. Chem. Soc.*, vol. 139, no. 4, pp. 1565–1574, 2017.
[243] M. Patila, A. Kouloumpis, D. Gournis, P. Rudolf, and H. Stamatis, “Laccase-Functionalized Graphene Oxide Assemblies as Efficient Nanobiocatalysts for Oxidation Reactions,” *Sensors*, vol. 16, no. 3, p. 287, 2016.
[244] L. I. Ramírez-Cavazos *et al.*, “Enhanced production of thermostable laccases from a native strain of Pycnoporus sanguineus using central composite design,” *J. Zhejiang Univ. Sci. B*, vol. 15, no. 4, pp. 343–352, Apr. 2014.
[245] S. Holmberg *et al.*, “Bioelectrochemical Study of Thermostable Pycnoporus sanguineus CS43 Laccase Bioelectrodes Based on Pyrolytic Carbon Nanofibers for Bioelectrocatalytic O2 Reduction,” 24-Nov-2015. [Online]. Available: http://pubs.acs.org/doi/abs/10.1021/acscatal.5b01600. [Accessed: 14-Feb-2018].